Contents of issue 1   vol. LV

IDENTIFICATION AND VALIDATION OF DAMAGE PARAMETERS FOR ELASTO-VISCOPLASTIC CHABOCHE MODEL

A. A m b r o z i a k

Gdańsk University of Technology
Faculty of Civil and Environmental Engineering
Department of Structural Mechanics and Bridge Structures
Narutowicza 11/12, 80–952 Gdańsk, Poland

The aim of the paper is to propose an improved procedure of damage material parameters identification of the Chaboche model, coupled with the concept of isotropic damage model proposed by AMAR and DUFAILLY [2]. The proposed approach has been implemented into subroutines of the FE MSC.Marc code, as the user's viscoplastic subroutine UVSCPL, and has been used to perform FE static and dynamic computations. The paper gives a brief description of the Chaboche model including damage. The results are also presented of FE dynamic analyses using the respective UVSCPL subroutine. Analyses have been made for the nickel-based superalloy INCO718 and for steel. The numerical examples prove that the proposed identification approach is effective and the numerical implementation is correct.

Key words: damage, elasto-viscoplastic constitutive model, Chaboche, FEM, MSC. Marc.

1. INTRODUCTION

The identification of material parameters and numerical modelling of material damage by means of continuum mechanics is the subject of the present paper. The continuum damage mechanics deals with the microscale-defined damage variables as an effective surface density of cracks or the density of cavity intersections with a plane. For reference, see e.g. KACHANOV [17] or LEMAITRE [24], where the authors focused on the extensive study of continuum damage mechanics.

Since KACHANOV [18] introduced in 1958 the concept of effective stress to describe the rupture process under creep conditions, many theories of the continuous damage mechanics have been developed, regarding the concept of the isotropic damage variable (see e.g. RABOTNOV [31], HAYHURST and LECKIE [16], LEMAITRE and PLUMTREE [25], LECKIE [21], SIMO and JU [32], FOTIU *et al.* [14], SKRZYPEK *et al.* [33]). In the present paper, the isotropic damage concept is used (see LEMAITRE [23] for details), which defines the surface density of microcracs and microcavities. For the sake of this concept the material damage parameters are specified. This approach is introduced into the FE procedure with the Chaboche model employed.

2. Chaboche model equations

In the 1960s Perzyna [29] proposed the elasto-viscoplastic constitutive model, based on the orthogonal condition in the plastic law. The extension of the Perzyna law is the constitutive model proposed by Chaboche [12]. The Chaboche model is based on the assumption of the strain additivity

$$(2.1) \qquad \dot{\boldsymbol{\varepsilon}} = \dot{\boldsymbol{\varepsilon}}^E + \dot{\boldsymbol{\varepsilon}}^I,$$

where $\dot{\boldsymbol{\varepsilon}}$ is the total strain rate, $\dot{\boldsymbol{\varepsilon}}^E$ is the elastic strain rate and $\dot{\boldsymbol{\varepsilon}}^I$ is the inelastic strain rate.

The isotropic damage expressed by the scalar parameter fulfils the condition $D \in (0, 1)$. Based on the damage model proposed by Kachanov [18], the effective tensor of elasticity $\mathbf{B}^*$ for damaged material may be represented by the standard elasticity tensor $\mathbf{B}$ reduced by the damage parameter

$$(2.2) \qquad \mathbf{B}^* = (1 - D) \cdot \mathbf{B}.$$

Therefore, the relation between the stress and strain rate for the assumed isotropic model of material can be expressed as follows:

$$(2.3) \qquad \dot{\boldsymbol{\sigma}} = (1 - D) \cdot \mathbf{B} : \dot{\boldsymbol{\varepsilon}}^E = \mathbf{B}^* : \left(\dot{\boldsymbol{\varepsilon}} - \dot{\boldsymbol{\varepsilon}}^I \right).$$

Consequently, the nominal stress rate $\dot{\boldsymbol{\sigma}}$ is replaced by the effective stress rate $\dot{\sigma}^*$ in the damaged material, according to the formula

$$(2.4) \qquad \dot{\boldsymbol{\sigma}}^* = \frac{\dot{\boldsymbol{\sigma}}}{1 - D}.$$

Replacing the initial stress by the effective stress in the constitutive equations of the undamaged material makes it possible to consider the case of damage. Therefore the damage evolution D, proposed by Lemaitre [23], is expressed by the equation

$$(2.5) \qquad \dot{D} = \left(\frac{Y}{S} \right)^s \cdot \dot{p}.$$

The variables s and S are the damage material parameters, which are specified on the basis of experimental tests. The rate of the equivalent plastic strain $\dot{p}$ will be specified in the next part of the paper. The function Y is determined by the Young's modulus E, the Poisson's ratio ν and the current values of damage D, the Huber–Mises equivalent stress σ_{eq} and the hydrostatic stress σ_H. This function is called the damage strain energy release rate. It is expressed by the equation

$$(2.6) \qquad Y = \frac{\sigma_{eq}^2}{2 \cdot (1 - D)^2 \cdot E} \cdot \left(\frac{2}{3} \cdot (1 + \nu) + 3 \cdot (1 - 2 \cdot \nu) \cdot \left(\frac{\sigma_H}{\sigma_{eq}} \right)^2 \right).$$

In isothermal conditions, the inelastic strain rate $\dot{\boldsymbol{\varepsilon}}^I$ in the basic variant of the Chaboche model can be expressed by the following formula

$$(2.7) \qquad \dot{\boldsymbol{\varepsilon}}^I = \frac{3}{2} \cdot \dot{p} \cdot \frac{\boldsymbol{\sigma}' - \mathbf{X}'}{J\left(\boldsymbol{\sigma}' - \mathbf{X}'\right)}.$$

The rate $\dot{p}$ is defined by the equation (see e.g. AMAR and DUFAILLY [2])

$$(2.8) \qquad \dot{p} = \left\langle \frac{\dfrac{J\left(\boldsymbol{\sigma}' - \mathbf{X}'\right)}{1 - D} - R - k}{K} \right\rangle^n$$

where k, K and n are material parameters. The material constant k corresponds to the initial yield stress, while the factor R describes the isotropic hardening. Following $\boldsymbol{\sigma}'$ and $\mathbf{X}'$ are the deviatoric parts of stress tensor and back-stress tensor. Additionally, the invariant $J\left(\boldsymbol{\sigma}' - \mathbf{X}'\right)$ is specified as

$$(2.9) \qquad J\left(\boldsymbol{\sigma}' - \mathbf{X}'\right) = \sqrt{\frac{3}{2}\left(\boldsymbol{\sigma}' - \mathbf{X}'\right) : \left(\boldsymbol{\sigma}' - \mathbf{X}'\right)}.$$

The evolution of the isotropic hardening R is defined by

$$(2.10) \qquad \dot{R} = b \cdot (R_1 - R) \cdot \dot{p},$$

while the kinematic $\mathbf{X}$ hardening is described as

$$(2.11) \qquad \dot{\mathbf{X}} = \frac{2}{3} \cdot a \cdot \dot{\boldsymbol{\varepsilon}}^I - c \cdot \mathbf{X} \cdot \dot{p}.$$

The variables b, R_1 and a, c are the material parameters, which have to be specified on the basis of laboratory tests. It should be noted that it is necessary to establish eleven material parameters in the presented model: two elastic parameters E and ν, seven inelastic parameters k, n, K, c, a, b, R_1, and two additional damage parameters S, s.

The detailed description of several variants of the Chaboche model, with the material parameters specified, was given by the present author in [4] and [37]. The constitutive equations of the Chaboche model, with respect to a hierarchy of various models, were presented by CHABOCHE in [12] and WOZNICA in [36]. AKTAA and SCHINKE [1] applied the damage model proposed by HAYHURST [16] to the Chaboche model. In the paper [11] BROCKS and LIN extended the Chaboche viscoplastic law to a finite strain form based on an internal dissipation inequality. The authors assumed a multiplicative decomposition of the deformation gradient into elastic and inelastic parts. In order to numerically investigate the extended viscoplastic law, finite element algorithm and several examples were presented.

3. Application of the Chaboche model to FE open code

In the numerical analysis the MSC.Marc system has been used. It is a multi-purpose, FEA program for advanced engineering simulations, ready to be extended by user's subroutines. In order to apply the Chaboche model to the MSC. Marc system, the user-defined subroutines UVSCPL [34] were applied, with the inelastic strain rate and the stress increments specified. The main part of the algorithm used in the UVSCPL subroutine is presented in the form of a flow chart, in two variants. In Fig. 1 the undamaged Chaboche model is shown and in Fig. 2 the damage is considered. The present author used this UVSCPL procedure for static and dynamic analysis with the Chaboche model (see e.g. [6] and [38]). It should be noted that the values of time functions should be calculated in each step of iteration.

$$\Delta \mathbf{X} = \frac{\Delta t}{2} \cdot \left(\dot{\mathbf{X}}_{t-\Delta t} + \dot{\mathbf{X}}_t \right), \quad \mathbf{X}_t = \mathbf{X}_{t-\Delta t} + \Delta \mathbf{X}$$

$$\Delta R = \frac{\Delta t}{2} \cdot \left(\dot{R}_{t-\Delta t} + \dot{R}_t \right), \quad R_t = R_{t-\Delta t} + \Delta R$$

$$\Downarrow$$

$$\boldsymbol{\sigma}'_t, \mathbf{X}'_t, J\left(\boldsymbol{\sigma}'_t - \mathbf{X}'_t\right), J\left(\boldsymbol{\sigma}'_t\right), \mathrm{tr}\left(\boldsymbol{\sigma}_t\right)$$

$$\Downarrow$$

$$\dot{p}_t = \left\langle \frac{J(\boldsymbol{\sigma}'_t - \mathbf{X}'_t) - R_t - k}{K} \right\rangle^n$$

$$\Downarrow$$

$$\dot{\boldsymbol{\varepsilon}}^I_t = \frac{3}{2} \cdot \dot{p}_t \cdot \frac{\boldsymbol{\sigma}'_t - \mathbf{X}'_t}{J\left(\boldsymbol{\sigma}'_t - \mathbf{X}'_t\right)}$$

$$\Downarrow$$

$$\dot{\mathbf{X}}_t = \frac{2}{3} \cdot a \cdot \dot{\boldsymbol{\varepsilon}}^I_t - c \cdot \mathbf{X}_t \cdot \dot{p}_t$$

$$\Downarrow$$

$$\dot{R}_t = b \cdot (R_I - R_t) \cdot \dot{p}_t$$

$$\Downarrow$$

$$\Delta \boldsymbol{\varepsilon}^I_t = \dot{\boldsymbol{\varepsilon}}^I_t \cdot \Delta t_t$$

$$\Downarrow$$

$$\Delta \boldsymbol{\sigma}_t = \mathbf{B} \cdot \left(\Delta \boldsymbol{\varepsilon}_t - \Delta \boldsymbol{\varepsilon}^I_t \right)$$

Fig. 1. Flow chart of the UVSCPL subroutine – Chaboche model.

$$\Delta \mathbf{X} = \frac{\Delta t}{2} \cdot \left(\dot{\mathbf{X}}_{t-\Delta t} + \dot{\mathbf{X}}_t \right), \quad \mathbf{X}_t = \mathbf{X}_{t-\Delta t} + \Delta \mathbf{X}$$

$$\Delta R = \frac{\Delta t}{2} \cdot \left(\dot{R}_{t-\Delta t} + \dot{R}_t \right), \quad R_t = R_{t-\Delta t} + \Delta R$$

$$\Delta D = \frac{\Delta t}{2} \cdot \left(\dot{D}_{t-\Delta t} + \dot{D}_t \right), \quad D_t = D_{t-\Delta t} + \Delta D$$

$$\Downarrow$$

$$\boldsymbol{\sigma}'_t, \mathbf{X}'_t, J\left(\boldsymbol{\sigma}'_t - \mathbf{X}'_t\right), J\left(\boldsymbol{\sigma}'_t\right), \operatorname{tr}\left(\boldsymbol{\sigma}_t\right), \boldsymbol{\sigma}_{eq}, \sigma_H$$

$$\Downarrow$$

$$\dot{p}_t = \left\langle \frac{\left(J(\boldsymbol{\sigma}'_t - \mathbf{X}'_t)/1 - D_t\right) - R_t - k}{K} \right\rangle^n$$

$$\Downarrow$$

$$\dot{\boldsymbol{\varepsilon}}_t^I = \frac{3}{2} \cdot \dot{p}_t \cdot \frac{\boldsymbol{\sigma}'_t - \mathbf{X}'_t}{J\left(\boldsymbol{\sigma}'_t - \mathbf{X}'_t\right)}$$

$$\Downarrow$$

$$\dot{\mathbf{X}}_t = \frac{2}{3} \cdot a \cdot \dot{\boldsymbol{\varepsilon}}_t^I - c \cdot \mathbf{X}_t \cdot \dot{p}_t$$

$$\Downarrow$$

$$\dot{R}_t = b \cdot (R_I - R_t) \cdot \dot{p}_t$$

$$\Downarrow$$

$$Y_t = \frac{\sigma_{eq}^2}{2 \cdot (1 - D_t)^2 \cdot E} \cdot \left(\frac{2}{3} \cdot (1 + \nu) \cdot + 3 \cdot (1 - 2 \cdot \nu) \cdot \left(\frac{\sigma_H}{\sigma_{eq}} \right)^2 \right)$$

$$\Downarrow$$

$$\dot{D}_t = \left(\frac{Y_t}{S} \right)^s \cdot \dot{p}_t$$

$$\Downarrow$$

$$\mathbf{B}_t^* = (1 - D_t) \cdot \mathbf{B}$$

$$\Downarrow$$

$$\Delta \boldsymbol{\varepsilon}_t^I = \dot{\boldsymbol{\varepsilon}}_t^I \cdot \Delta t_t$$

$$\Downarrow$$

$$\Delta \boldsymbol{\sigma}_t = \mathbf{B} \cdot \left(\Delta \boldsymbol{\varepsilon}_t - \Delta \boldsymbol{\varepsilon}_t^I \right)$$
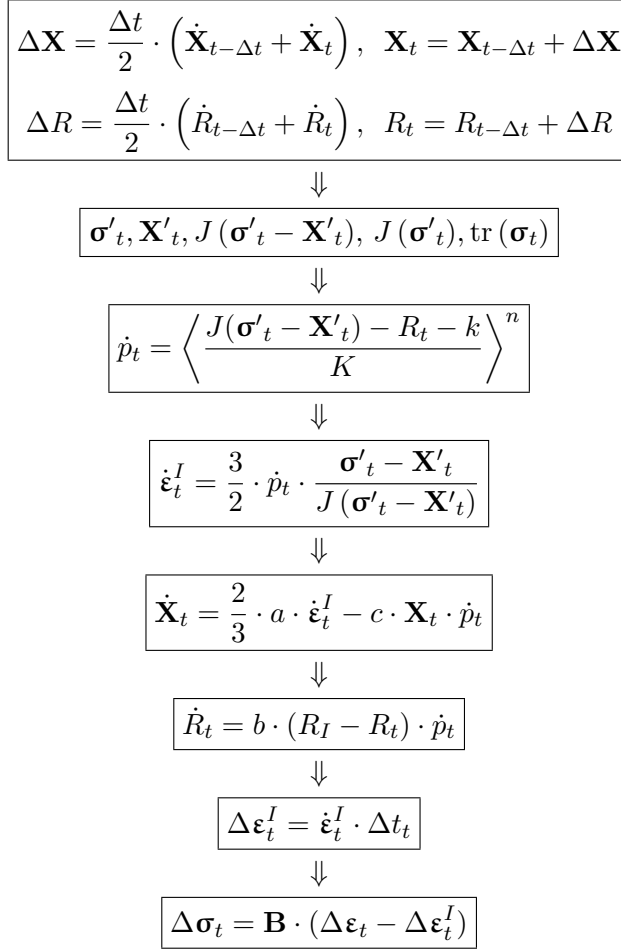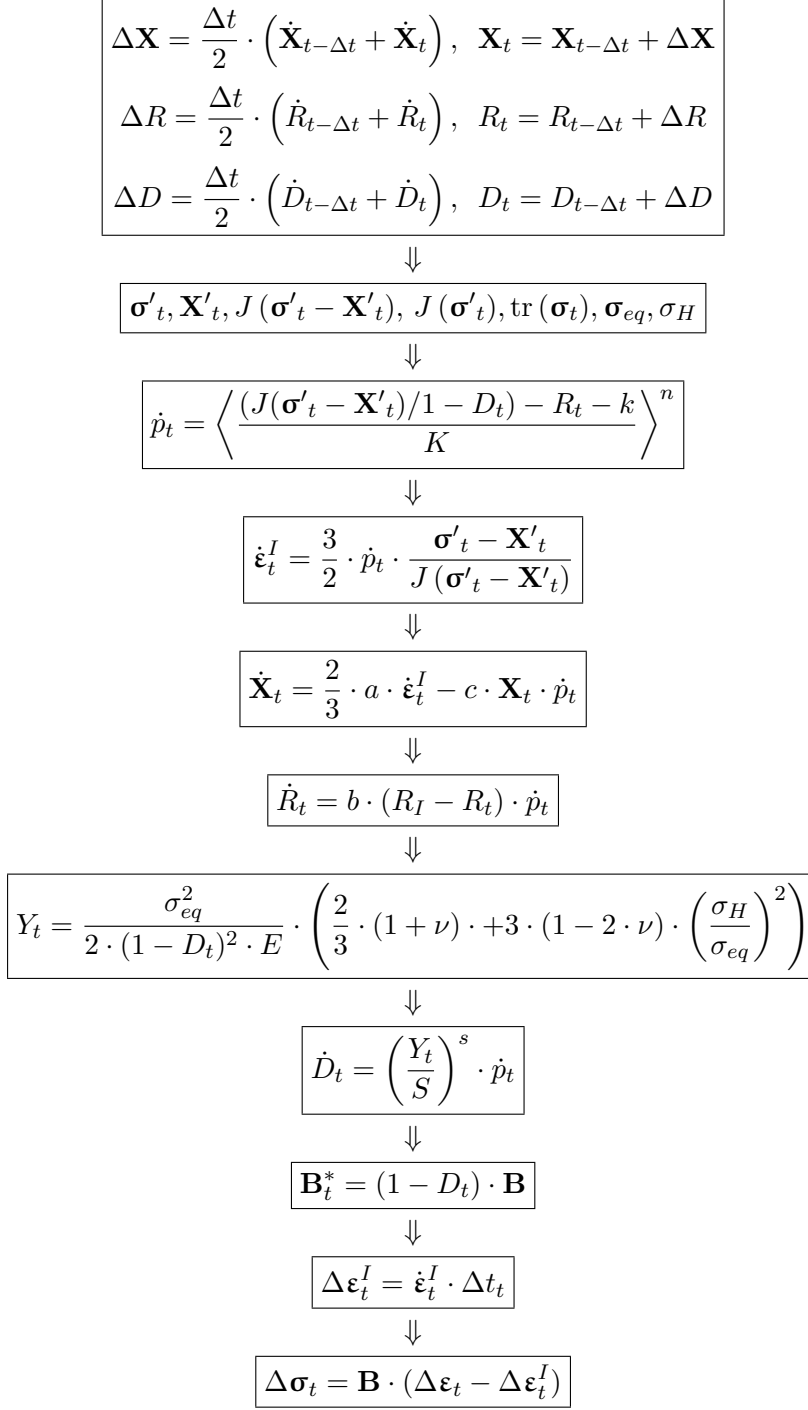
Fig. 2. Flow chart of the UVSCPL subroutine – Chaboche model with damage.

Additionally, at the beginning of a given time step t_i, in the first iteration all values with index t are taken as the final values from the previous step $t_i - \Delta t$.

It should be noted that other commercial FE codes exist; they enable us to introduce the constitutive models defined by the user. For example, some results can be specified of FE analyses. They are the user-defined material models UMAT, in the form of a subroutine introduced to the FE ABAQUS code with the unified viscoplastic model proposed by BODNER and PARTOM [10] and by CHABOCHE [13] for polycrystal alloys, and the creep model suggested by BERTRAM and OLSCHEWSKI [9] for single crystal alloys, coupled with the anisotropic damage model. All these models are presented by QI and BROCK [30].

4. IDENTIFICATION OF DAMAGE PARAMETERS

4.1. Concept of identification

The present author used the concept proposed by AMAR and DUFAILLY [2] in the process of identification of material parameters dealing with damage. In this concept it is assumed that at the beginning of the identification process of damage material parameters the basics constants for the Chaboche model are specified. If the parameters: E, ν and k, n, K, c, a, b, R_1 are known, the damage material parameters can be specified. The detailed description of identification of the material parameters for the Chaboche model is described e.g. by KŁOSOWSKI [19] or AMAR and DUFAILLY [2]. The design of experiments suitable for the parameter identification of the Chaboche material model under the uniaxial loading and stationary temperature conditions has been proposed also by FURAKAWA and YAGAWA [15]. For the detailed studies of experimental methods in material dynamics and impact, the author refers to the work [28].

The material parameters are usually identified on the basis of the uniaxial tension tests. In the case of uniaxial tension tests, the stress tensor $\boldsymbol{\sigma}$ has one non-vanishing component σ

$$(4.1) \qquad \boldsymbol{\sigma} = \begin{bmatrix} \sigma & 0 & 0 \\ 0 & 0 & 0 \\ 0 & 0 & 0 \end{bmatrix},$$

while the Huber–Mises equivalent stress $\sigma_{eq} = \sigma$ and the hydrostatic stress $\sigma_H = \sigma/3$. Then the function of the energy density (Eq. (2.6)) can be rewritten as

$$(4.2) \qquad Y = \frac{\sigma^2}{2 \cdot (1 - D)^2 \cdot E}.$$

For simplicity it has been assumed that rupture of the specimen is specified by the rupture time t_r, while $D = 1.0$. Additionally, in practical applications it is necessary to specify the value of the critical damage D_c, which indicates the limit of the theory. It should be noted that this factor must be lower than 1.0. It usually lies between 0.2 and 0.8, depending on the type of material; see e.g. LEMAITRE [22]. Substituting Eq. (4.2) into Eq. (2.5) we obtain

$$\dot{D} = \left(\frac{\sigma^2}{2 \cdot (1 - D)^2 \cdot E \cdot S} \right)^s \cdot \dot{p},$$

(4.3)

$$\dot{D} \cdot (1 - D)^{2 \cdot s} = \left(\frac{\sigma^2}{2 \cdot E \cdot S} \right)^s \cdot \dot{p}.$$

The author has assumed, as AMAR and DUFAILLY in [2], that the value of the parameter s is chosen arbitrarily; only the factor S has to be determined. Then the interchange of variation is used; the Eq. (4.3) can be transformed to the expressions

$$\int_0^1 (1 - D)^{2 \cdot s} \, dD = \frac{1}{2 \cdot s + 1} = \int_0^{t_r} \left(\frac{\sigma^2}{2 \cdot E \cdot S} \right)^s \cdot \dot{p} \, dt,$$

(4.4)

$$\frac{1}{2 \cdot s + 1} = \left(\frac{1}{2 \cdot E \cdot S} \right)^s \cdot \int_0^{t_r} \sigma^{2 \cdot s} \cdot \dot{p} \, dt \, ;$$

$$(2 \cdot s + 1)^{1/s} = 2 \cdot E \cdot S \cdot \frac{1}{\left(\int_0^{t_r} \sigma^{2 \cdot s} \cdot \dot{p} \, dt \right)^{1/s}}.$$

Finally, we obtain the equation of the damage material parameter S

(4.5)

$$S = \frac{(2 \cdot s + 1)^{1/s}}{2 \cdot E} \cdot \left(\int_0^{t_r} \left(\sigma^{2 \cdot s} \cdot \dot{p} \right) dt \right)^{1/s}.$$

We can notice that the parameter S depends on the parameter s and the history of loading (directly on σ and $\dot{p}$). It is necessary to establish the rupture time of the specimen t_r form the uniaxial tensile tests. Additionally it is necessary to obtain the value of the σ_j and $\dot{p}_j$ at each time step. Calculations to the first approximation of the value of the damage parameters have to be performed without damage. To calculate the integral from Eq. (4.5), the present author

used simple method of numerical integration, according to the formula

$$(4.6) \qquad \int_0^{t_r} \left(\sigma^{2 \cdot s} \cdot \dot{p} \right) \, dt = \sum_{j=1}^{n} \left[(\sigma_j)^{2 \cdot s} \cdot \dot{p}_j \cdot \Delta t_j \right].$$

Therefore, in the next calculation step, knowing the value of the rupture strain ε_r established in the laboratory test, the parameter S is calculated. The first approximation of the parameter S is made on the basis of the Chaboche model analysis without damage. According to Eq. (4.5), considering the evolution of the stress and $\dot{p}$, the first approximation of the damage parameter S_i is determined. The parameter S is evaluated from the following equation:

$$(4.7) \qquad S_{i+1} = S_i \cdot \frac{\varepsilon_r^{\mathrm{exp}}}{(\varepsilon_r)_i},$$

where $\varepsilon_r^{\mathrm{exp}}$ is the rupture strain, which has been established on the basis of the experimental test; $(\varepsilon_r)_i$ and S_i are the rupture strain and the value of damage parameter S obtained in the i-th iteration of the numerical simulation (index i specifies the number of approximation of the parameter S). In the above concept of identification it is necessary to know the load history and the rupture time t_r, which corresponds to the rupture strain ε_r (leading to the rupture of specimen of the investigated material).

4.2. Identification example – experiment simulation

In this section the present author is basing on the known material parameters for Chaboche model with damage. For these known parameters the author performed simulation of experiments of the uniaxial tensile tests, which are used in the identification process of the damage parameters, according to the concept of identification presented in the preceding section. At the beginning of the identification process of the damage parameters, the author assumed that the basic parameters for Chaboche model are known (E, ν, k, n, K, c, a, b and R_1).

AMAR and DUFAILLY [2] presented the material parameters for nickel-based superalloy INCO718 (at 650° C [2]): $E = 162000.0$ [MPa], $\nu = 0.3$ [$-$], $k = 501$ [MPa], $b = 15.0$ [$-$], $R_1 = -165.4$ [MPa], $a = 80000.0$ [MPa], $c = 200.0$ [$-$], $n = 2.4$ [$-$], $K = 12790$ $\left[(\mathrm{MPa} \cdot \mathrm{s})^{1/n} \right]$, $S = 4.48$ [MPa], $s = 3.0$ [$-$]. On the basis of these material parameters, the authors performed the simulation of the constant strain rate test for $\dot{\varepsilon} = 0.01$ $\left[\mathrm{s}^{-1} \right]$ (see Fig. 3, "Experiment simulation"). The numerical calculation was performed for the truss structure, subjected to the uniaxial tension test. The following geometrical parameters were assumed: length $l = 1.0$ [m] and cross-sectional area $A = 0.001$ [m^2]. It should be noted that failure of the specimen happened suddenly, see Fig. 3.
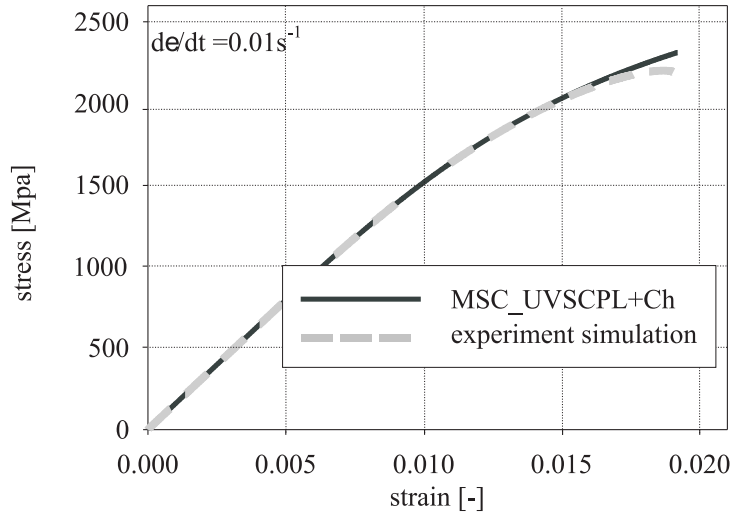
FIG. 3. Constant strain rate test for $\dot{\varepsilon} = 0.01 \text{ s}^{-1}$.

On the basis of the simulation of experiments performed for the constant strain rate test $\dot{\varepsilon} = 0.01 \left[\text{s}^{-1}\right]$, the following rupture time $t_r^{\text{exp}} = 1.92$ [s] (which corresponds to $\varepsilon_r^{\text{exp}} = 0.0192$ [–]) is established. For the purpose of the first approximation of the damage parameters, the author carried out the numerical calculations for the Chaboche model without damage to the limit of the strain $\varepsilon_r^{\text{exp}}$ (see Fig. 3). On the basis of these calculations the evolution of the stress and the rate $\dot{p}$ was specified, see Fig. 4.
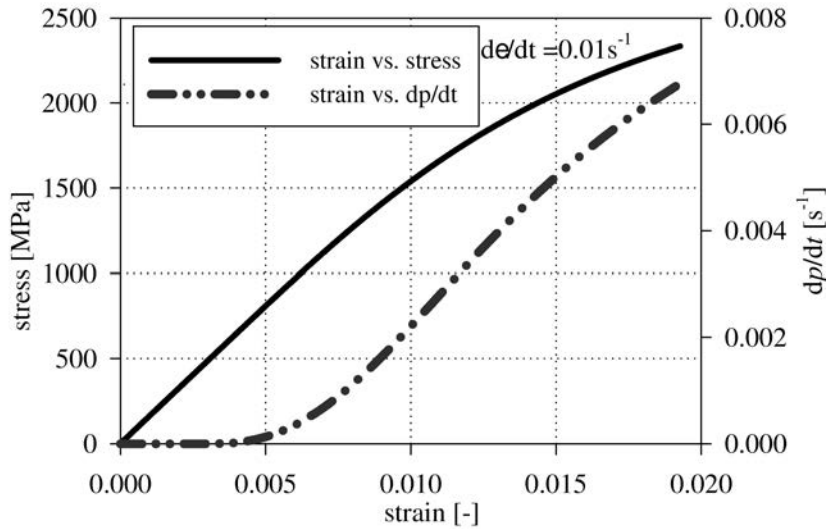
FIG. 4. Stress and $\dot{p}$ in the strain domain for $\dot{\varepsilon} = 0.01 \text{ s}^{-1}$.

Additionally, at the beginning of the identification process, it was necessary to assume the value of s. In the present investigation the author performed the identification process for five assumed values of parameter s: 1.0; 2.0; 3.0; 4.0; 5.0. In these cases it is possible to observe evolution of the damage material parameters. The values of parameters s may be specified optionally, but the author assumed them to be an integer S (the parameter s is the exponent in the Eq. (2.5)). The first approximation of the parameter S (named S_1 see Table 1), is calculated on the basis of the Chaboche analysis without damage. The following approximation S_i, according to Eq. (4.7), is performed for the Chaboche model coupled with damage. In each step of numerical calculations, strain $(\varepsilon_r)_i$ is specified and compared with the rupture strain obtained from laboratory tests. The results of identification of the damage material parameters are given in Table 1. It is possible to observe that the convergence of the parameter S is better for higher values of the parameter s.

Table 1. Identification of damage parameters.

i	1	2	3	4	5	6	7
$s = 1.0$ [–]							
S_i [MPa]	0.179	0.200	0.219	0.232	0.250	0.260	0.265
$(\varepsilon_r)_i$	0.0170	0.0175	0.0180	0.0183	0.0187	0.0190	0.0191
$s = 2.0$ [–]							
i	1	2	3	4			
S_i [MPa]	1.99	2.10	2.15	2.20			
$(\varepsilon_r)_i$	0.0182	0.0187	0.0189	0.0191			
$s = 3.0$ [–]							
i	1	2	3	5			
S_i [MPa]	4.26	4.33	4.40	4.45			
$(\varepsilon_r)_i$	0.0189	0.0189	0.0190	0.0191			
$s = 4.0$ [–]							
i	1	2					
S_i [MPa]	6.15	6.25					
$(\varepsilon_r)_i$	0.0189	0.0191					
$s = 5.0$ [–]							
i	1	2					
S_i [MPa]	7.62	7.70					
$(\varepsilon_r)_i$	0.0190	0.0192					

For each of the assumed values of the parameter s, parameters S are estimated, see Table 1. For these pairs of damage material parameters, numerical simulation of the uniaxial tension tests for $\dot{\varepsilon} = 0.01\,\mathrm{s}^{-1}$ is performed, see Figs. 5 and 6. In spite of the same rupture strain ε_r specified for each pair of parameters s and S, it is possible to observe small differences between strain vs. stress curves, given in Figs. 5 and 6. These differences can be seen better on the background of the strain vs. damage D curves.
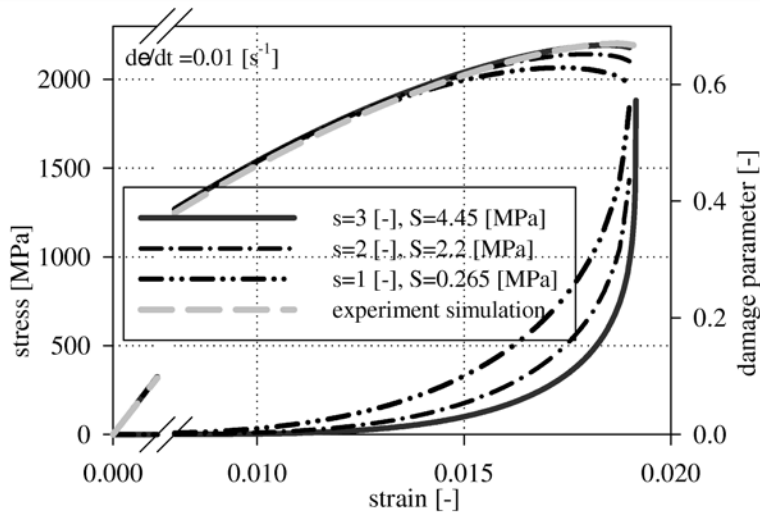
FIG. 5. Simulation of constant strain rate for different values of damage parameters.
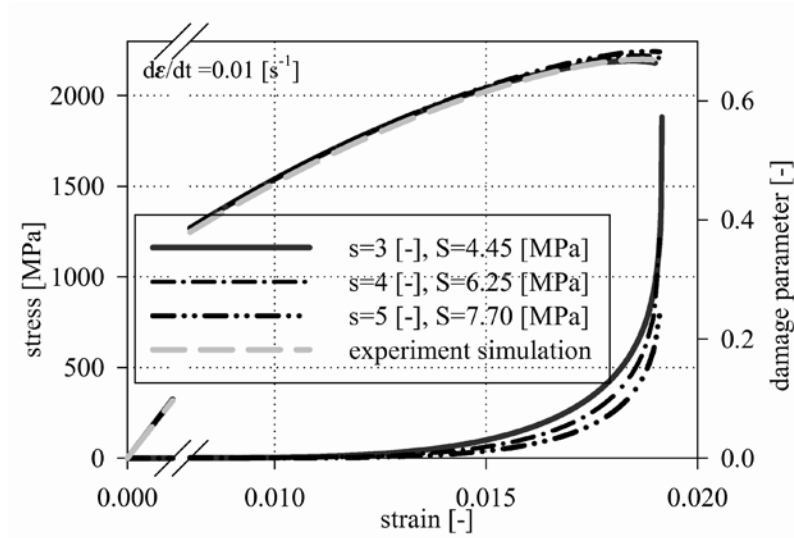
FIG. 6. Simulation of constant strain rate for different values of damage parameters.

For the purpose of final acceptance of pair of damage parameters, simulation of the creep tests (constant stress tests) for $\sigma = 2000$ [MPa] for each pair of the parameters s and S are performed. The obtained results are given in Figs. 7 and 8, where only the numerical calculations with the damage parameters $s = 3.0$ [–] and $S = 4.45$ [MPa] give a good approximation of the simulation of the experiment, see Fig. 9.
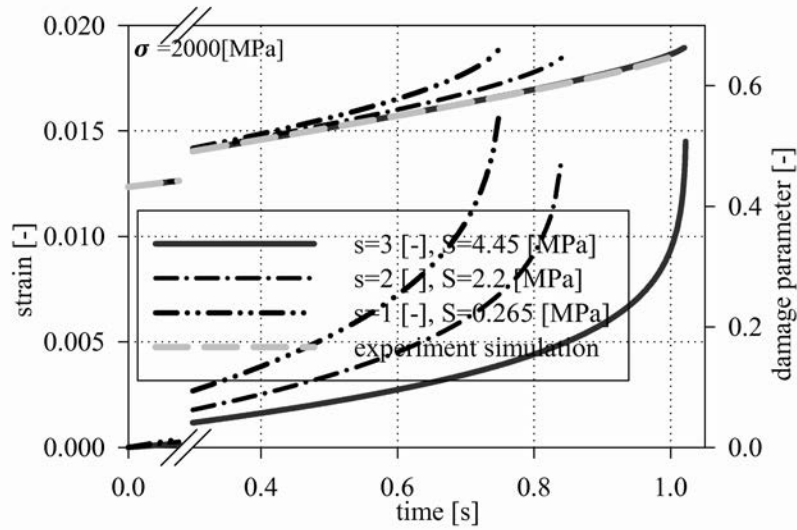
FIG. 7. Creep test for $\sigma = 2000$ [MPa] for different values of damage parameters.
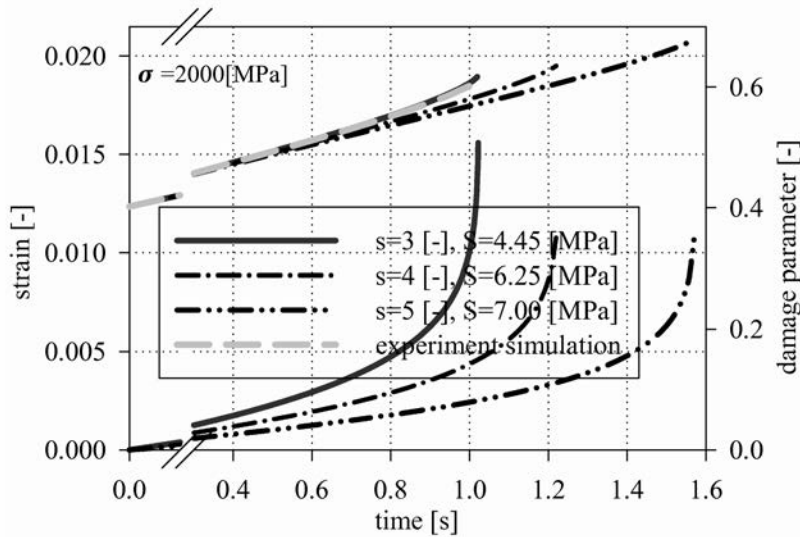
FIG. 8. Creep test for $\sigma = 2000$ [MPa] for different values of damage parameters.

Similarly to the case of a constant strain rate, the damage parameters can be determined on the basis of the creep tests. For that purpose the evolution of the stress and the rate $\dot{p}$ (see Fig. 10) is performed. The parameter S (see Eq. (4.5)) in the Chaboche model calculations without damage are ex-
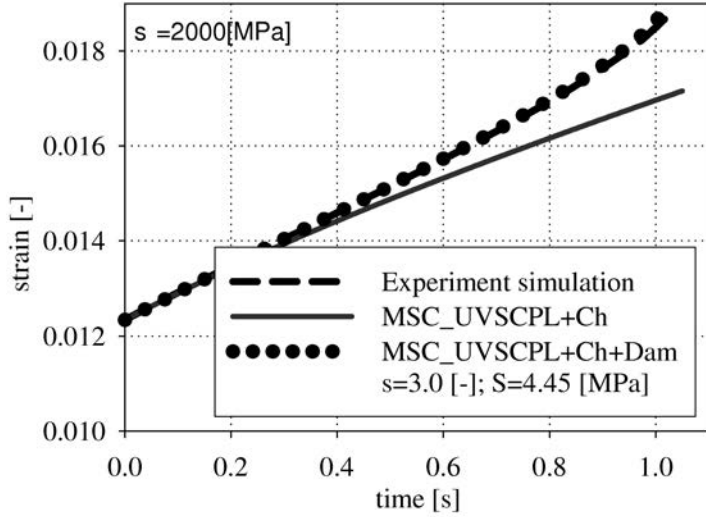
FIG. 9. Creep test for $\sigma = 2000$ [MPa] .
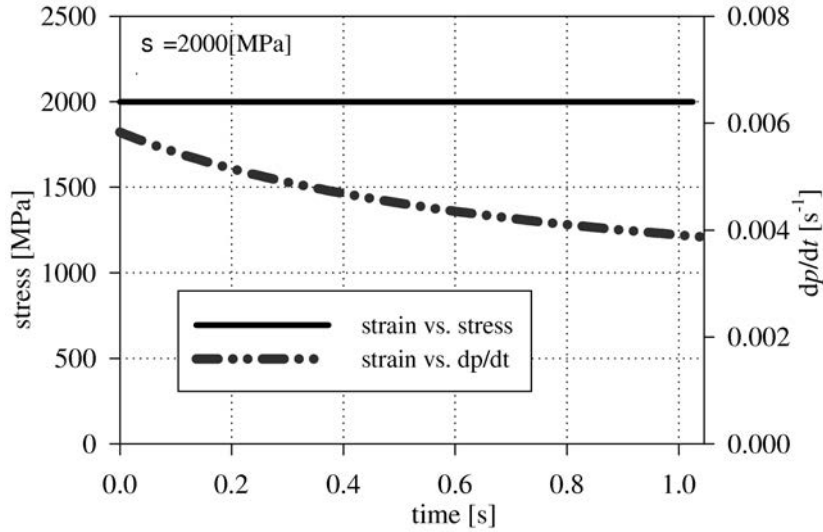
FIG. 10. Stress and $\dot{p}$ in the time domain $\sigma = \text{const} = 2000$ [MPa].

ploited, see Fig. 9 (MSC_UVSCPL+Ch). On the basis of simulation of experiments of the creep test, the rupture times $t_r = 1.045$ [s] (which correspond to $\varepsilon_r^{\text{exp}} = 0.0171$ [–]) are specified. Based on the stress and $\dot{p}$ evolution (see Fig. 10) the first approximation of the parameters $S = 3.98$ [MPa] is calculated for the assumed value of $s = 3.0$ [–]. Next iteration of the numerical analysis gives the final values of $S = 4.45$ [MPa].

4.3. Identification example – direct experiment

In this section the present author identify the damage parameters for steel at 20°C, based on laboratory tests, performed by KŁOSOWSKI [19]. The experimental tests were carried out at the Department of General Mechanics of RWTH Aachen. The following parameters for the basic variant of the Chaboche model are taken for steel (see KŁOSOWSKI [19] for details): $E = 223000$ [MPa], $\nu = 0.3$ [–] and $k = 210.15$ [MPa], $n = 9.51$ [–], $K = 14.085$ [MPas$^{1/n}$], $c = 38840$ [–], $a = 611700$ [MPa], $b = 16.74$ [–], $R_1 = -138.48$ [MPa].

Like in the former case (see preceding section), the damage material parameters for Chaboche model are specified on the basis of the constant strain rate tests. According to the Eq. (4.5) and assuming the value of $s = 2.0$ [–], with the following approximations considered, the parameter $S = 0.4$ [MPa] has been specified.

The results of damage analysis for the estimated damage parameters ($s = 2.0$ [–], $S = 0.4$ [MPa]) with two different strain rates $\dot{\varepsilon} = 0.01$ $[\text{s}^{-1}]$ and $\dot{\varepsilon} = 0.001$ $[\text{s}^{-1}]$ are given in Figs. 11 and 12. Good agreement has been obtained of strain vs. stress curves from FE calculations and the experiment.

On the basis of numerical simulations the present author has observed that the damage is indicated when the strain is equal to 0.01 [–]. The strains less than 0.01 [–] result in the zero value of the damage parameter D. There is no difference between the results obtained from the numerical simulations with damage (MSC+UVSCPL+Ch+Dam) and without damage (MSC+UVSCPL+Ch), see Fig. 13. This limit specified the strain at the damage threshold.
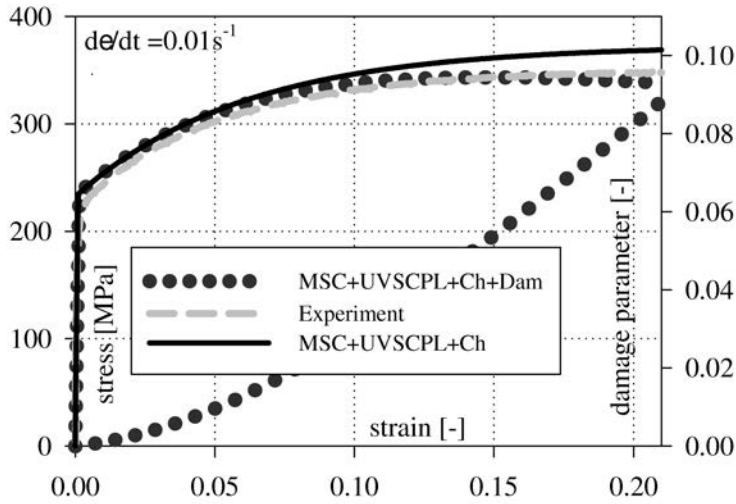
FIG. 11. Numerical simulation of the uniaxial tension test for $\dot{\varepsilon} = 0.01$ $[\text{s}^{-1}]$.
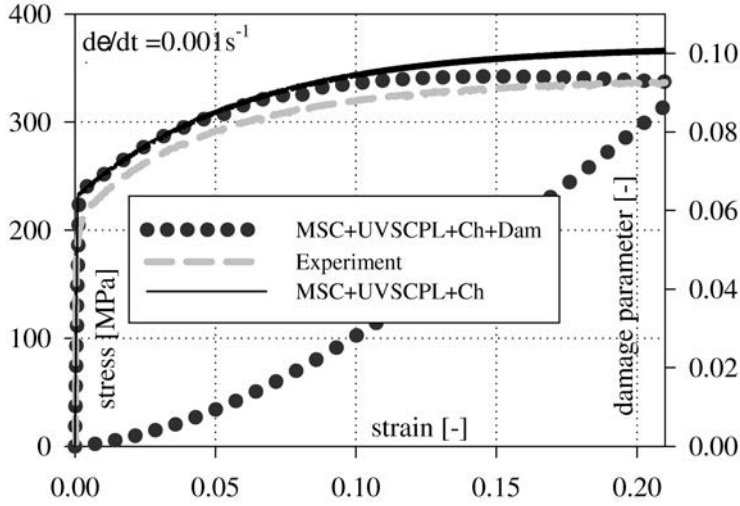
FIG. 12. Numerical simulation of the uniaxial tension test for $\dot{\varepsilon} = 0.001 \left[s^{-1}\right]$.
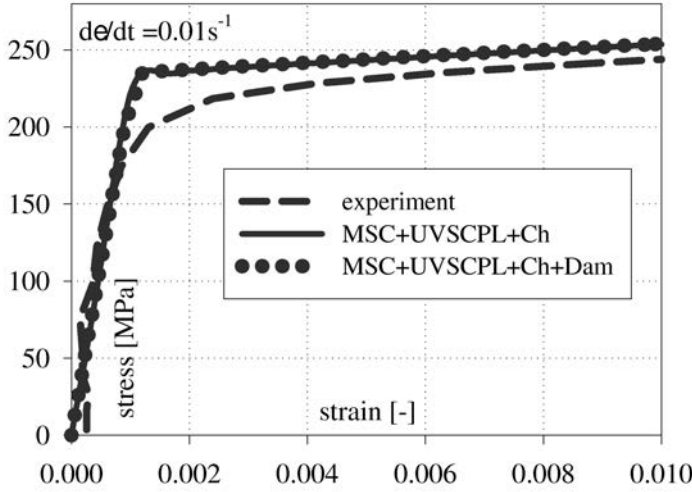
FIG. 13. Numerical simulation of the uniaxial tension test for $\dot{\varepsilon} = 0.01 \left[s^{-1}\right]$ to the ε_d.

In Table 2 the characteristic values of the ductile damage parameters for three chosen types of steel are given. The strains ε_d and ε_r (see Table 2) specify the strain at damage threshold and strain at failure, and D_c is the critical damage (the value of damage parameter D at macrocracks initiation).

Table 2. Characteristic ductile damage parameters.

Material	ε_d [–]	ε_r [–]	D_c [–]
investigated steel	0.01 [a]	0.45 [b]	0.10 [a]
steel XC 38 [23]	0.00	0.56	0.22
steel 30CD4 [23]	0.02	0.37	0.24
steel E24 [23]	0.50	0.88	0.17

[a] parameters are established on the basis of numerical simulations of uniaxial tensile tests,
[b] parameter is established on the basis of laboratory tests.

5. NUMERICAL EXAMPLES

5.1. Example 1

In this example the numerical analysis of circular steel plate under impact load are investigated. According to symmetry of the structure and loading, a quarter of the plate was analysed. The geometry of the plate used in the numerical calculations is shown in Fig. 14. In the analysis, the four-node shell elements were applied (Element 139, see [34]). The verification was done of the assumed boundary conditions and type of the analysis. For details see [3], where the author described the application of the Bodner–Partom constitutive equations in the finite element analysis.

t [ms]	$p(t)$ $[10^5\mathrm{Pa}]$
0.0	0.00
3.2	0.00
3.5	3.40
4.1	3.40
4.5	4.00
6.0	4.50
11.3	4.60
14.2	5.60
16.0	5.80
24.0	6.05
28.0	6.10
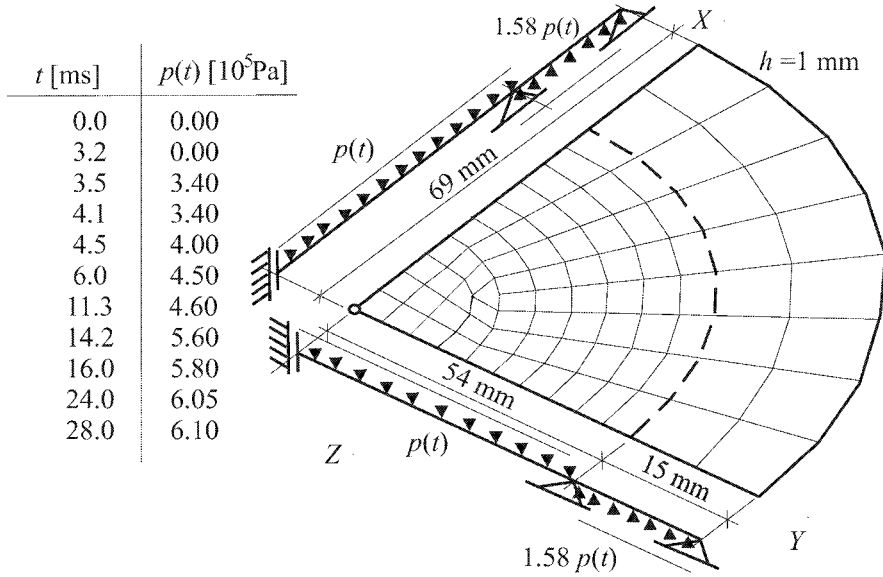
FIG. 14. Circular steel plate subjected to the impact pressure.

For the examined material, the following parameters were assumed: the elastic modulus $E = 223000.0$ [MPa], the Poisson's ratio $\nu = 0.3$ [–]; the thickness of the steel plate $t = 1$ mm. Additionally, the following material parameters for Chaboche model were taken: $k = 210.15$ [MPa], $n = 9.51$ [–], $K = 14.085$ [MPas$^{1/n}$], $c = 38840$ [–], $a = 611700$ [MPa], $b = 16.74$ [–], $R_1 = -138.48$ [MPa], with the damage parameters $s = 2.0$ [–] and $S = 0.4$ [MPa] estimated in the previous section.

The numerical calculations were performed using the proportional damping matrix with the Rayleigh damping multipliers $\alpha = 3.46 \cdot 10^{-6}$ and $\beta = 27.32$. Parameters α and β are the stiffness matrix multiplier and the mass matrix multiplier, respectively. They were calculated by the formula

(5.1)
$$\alpha = 2 \cdot \frac{(\xi_2 \cdot \omega_2 - \xi_1 \cdot \omega_1)}{\omega_2^2 - \omega_1^2},$$

$$\beta = 2 \cdot \omega_1 \cdot \omega_2 \cdot \frac{(\xi_1 \cdot \omega_2 - \xi_2 \cdot \omega_1)}{\omega_2^2 - \omega_1^2},$$

assuming that for the value of critical damping, the first two frequencies were given. The concept of specifying these multipliers is proposed in the paper [7]. To integrate the nonlinear equations of motion, the Newmark algorithm with the time step $\Delta t = 5 \cdot 10^{-7}$ was carried out.

Elasto-viscoplastic Chaboche model with damage is used to describe the behaviour of the steel plate under dynamic vibrations Fig. 15. These results of numerical simulations are compared with the results of the experimental test, which was performed in the impact pipe.
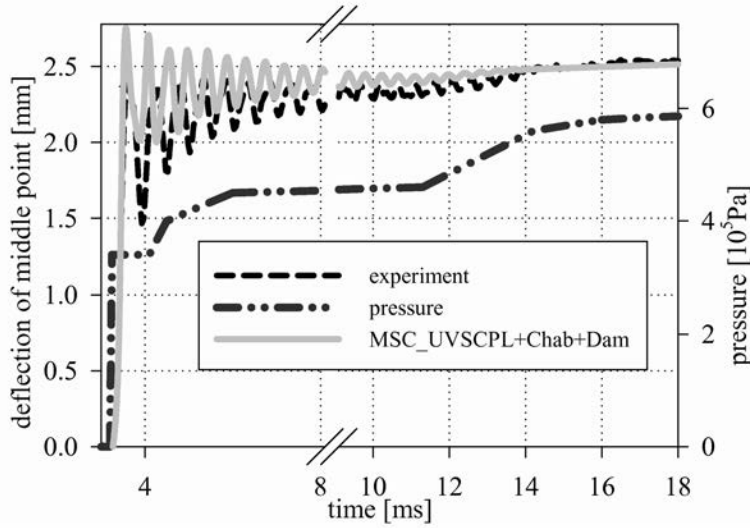
FIG. 15. Inelastic damped vibrations of the plate.

It should be noted that the elastic solution (see Fig. 16) gives a completely
different response of the vibrations, while the Chaboche model calculations are
close to the experimental results. The maximum value of the damage parameter
in this case is about 0.002 [–], thus a non-damage state of the plate is observed.
Additionally, the velocity and acceleration plots (Figs. 17, 18) in the time domain
illustrate the dynamic behaviour of the plate under impact load.
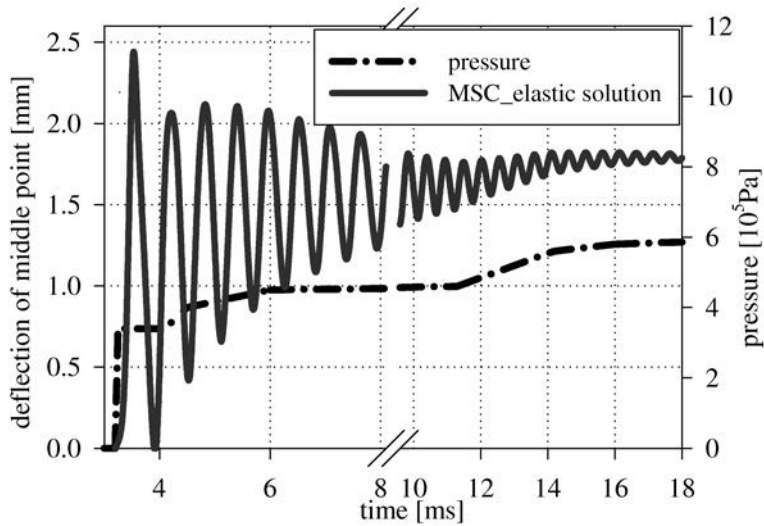
Fɪɢ. 16. Elastic damped vibrations of the plate.
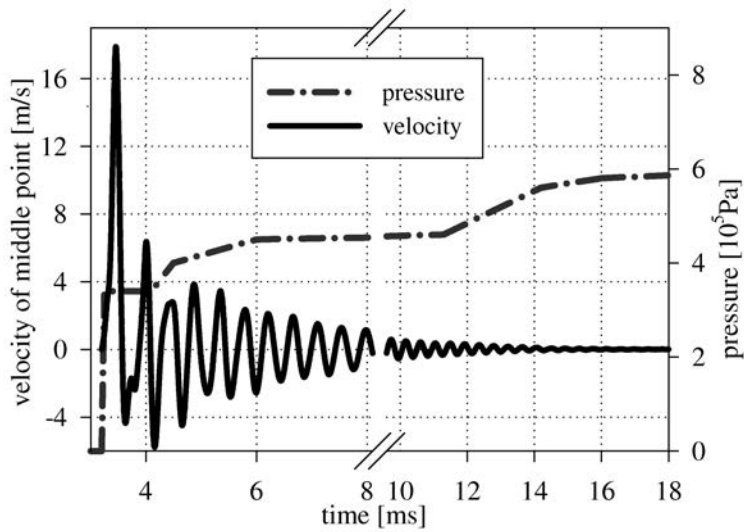
Fɪɢ. 17. Middle point velocity.
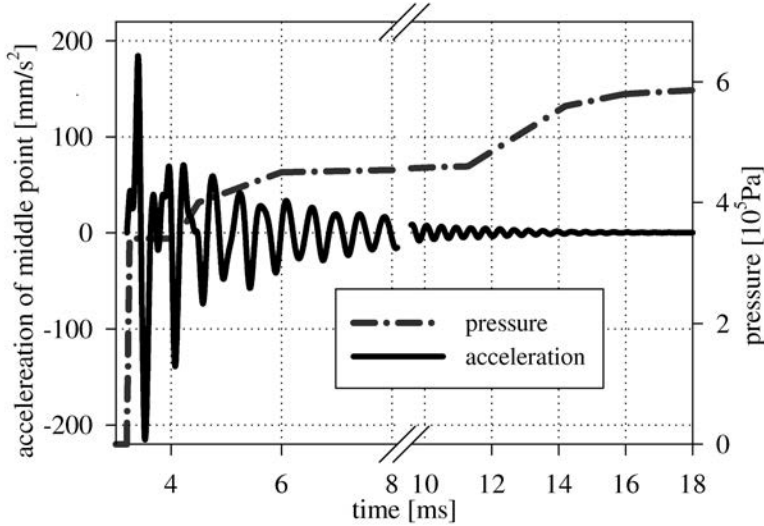
FIG. 18. Middle point acceleration.

5.2. Example 2

At the beginning, the dynamic analysis of a rod subjected to the impact force is presented. The elasto-viscoplastic constitutive equations of the Chaboche model with damage are taken to describe the behaviour of the material. Numerical calculations are performed for a simple truss structure, with the following geometrical parameters: $l = 1.0$ [m] (length) and $A = 0.001$ [m^2] (cross-section area). One of the ends of the rod is fixed while the next end is free. The free end of the truss element is subjected to impact forces F.

The dynamic analysis for three different values of the impact forces $F = 0.10$ [MN] (see Fig. 20), $F = 0.11$ [MN] (see Fig. 21) and $F = 0.12$ [MN] (see Fig. 22) is performed. The force is acting rapidly on the structures, in the time $t = 0.0$ [s], see Fig. 19. For the calculation, the material constants, corresponding to the Chaboche model with the following damage constants were taken (INCO718 at 650°C [2], see also [20]): $E = 159.0$ [GPa], $\nu = 0.3$ [–], $k = 514.21$ [MPa], $b = 60.0$ [–], $R_1 = -194.39$ [MPa], $a = 170000.0$ [MPa], $c = 500.0$ [–], $n = 4.0$ [–], $K = 1023.5$ $\left[(\text{MPa}\cdot\text{s})^{1/n}\right]$, $S = 4.48$ [MPa], $s = 3.0$ [–]. The reference calculations (named MSC_UWSCPL+Ch, see Figs. 20, 21 and 22) were performed without damage, according to the FE procedure given in Fig. 1.

In the research, two variants of the Chaboche model analysis are compared with each other: considering and neglecting the damage. In this case, small influence of damage is observed in the examined time range when the values of

forces are $F = 0.10$ [MN] (see Fig. 20) and $F = 0.11$ [MN] (see Fig. 21). The
force $F = 0.12$ [MN] (see Fig. 22) results exceed the limiting damage value, the
specimen is destroyed. Evaluation of the damage parameter D, specified by Eq.
(2.5), as a function of time, is given in Fig. 23. Due to the merely numerical
character of the example, only the calculations for free vibrations are consid-
ered. To integrate the nonlinear equations of motion, in the present example the
Newmark algorithm [27] with the time step $\Delta t = 5 \cdot 10^{-5}$ [s] is applied.
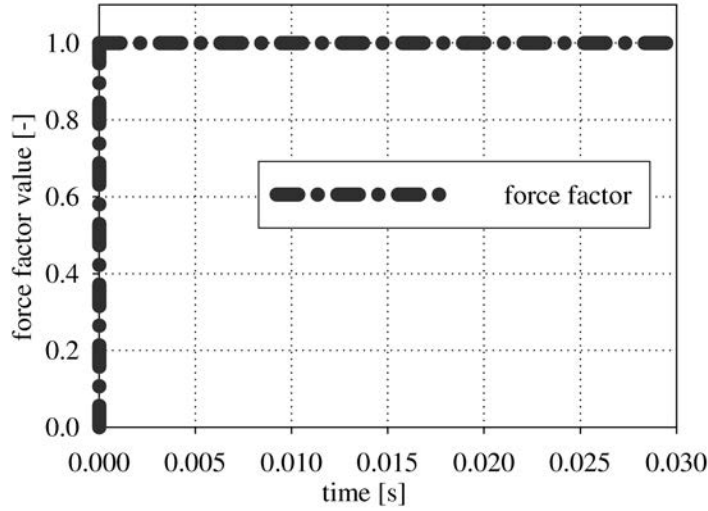
FIG. 19. Force factor value history diagram.
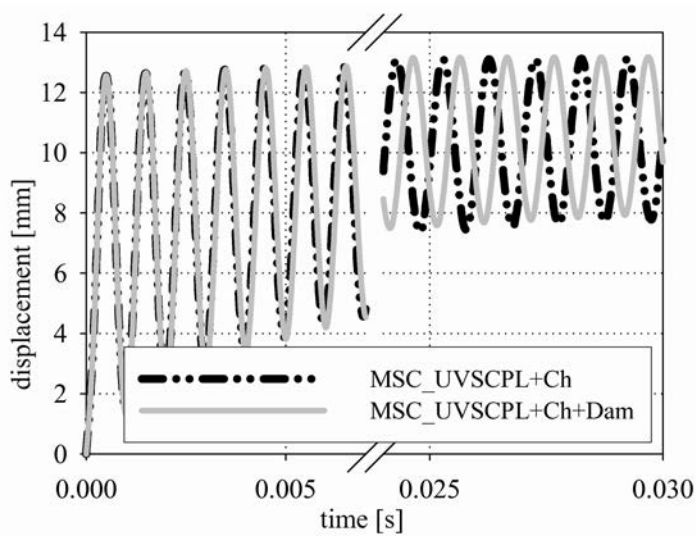
FIG. 20. Displacement diagram for $F = 0.10$ MN.
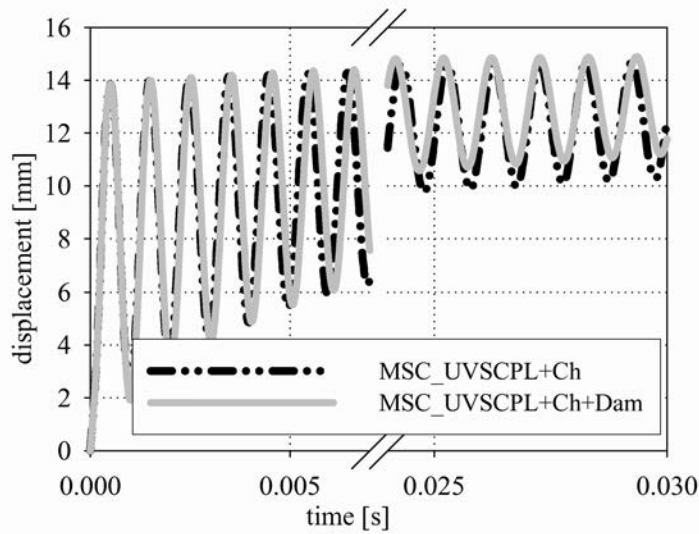
Fig. 21. Displacement diagram for $F = 0.11$ MN.
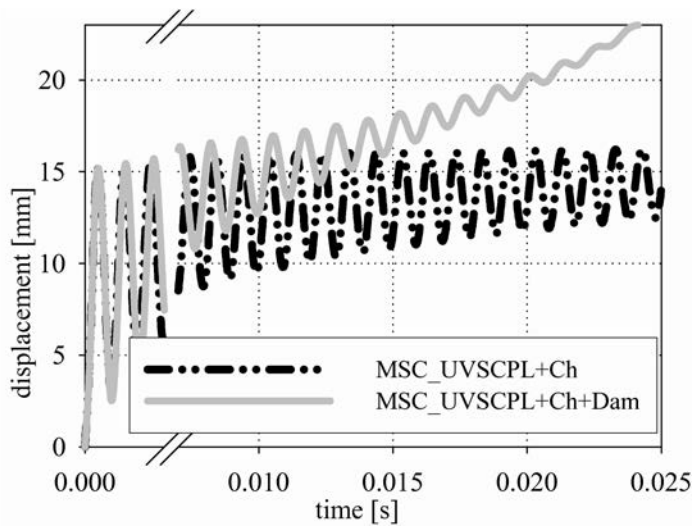
Fig. 22. Displacement diagram for $F = 0.12$ MN.

In the second variant of calculations, geometry of the plate is taken from the Example 1, see Fig. 14. In this case, the material parameters for INCO alloy at 650°C are accepted for the description of the plate material. The evolution of pressure in time domain is accepted according to Fig. 19. High value of the impact pressure, $p = 11.5$ [10^5 Pa], was assumed for distinct presentation of application
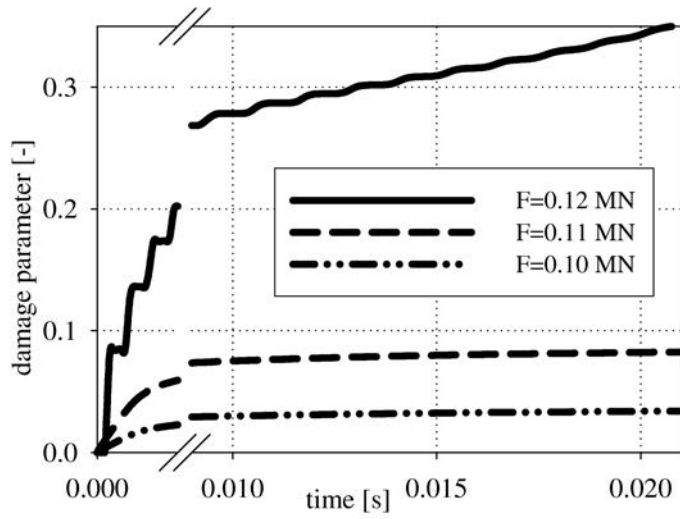
Fɪɢ. 23. Damage parameter evolution.
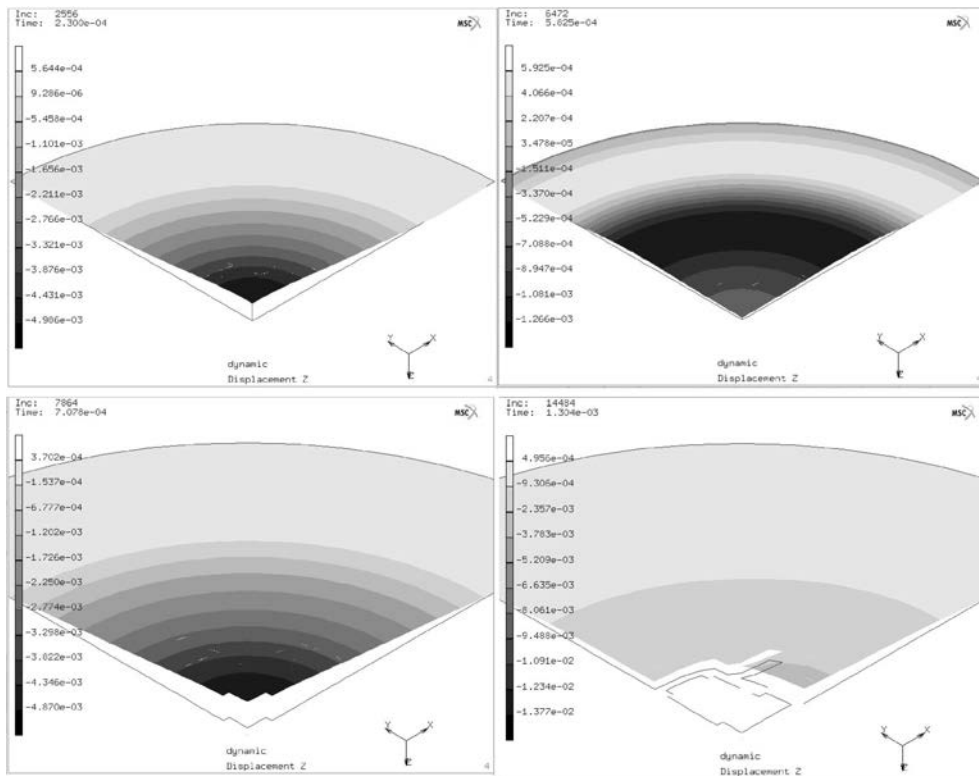
Fɪɢ. 24. Damage analysis with UVSCPL+UACTIV subroutines.
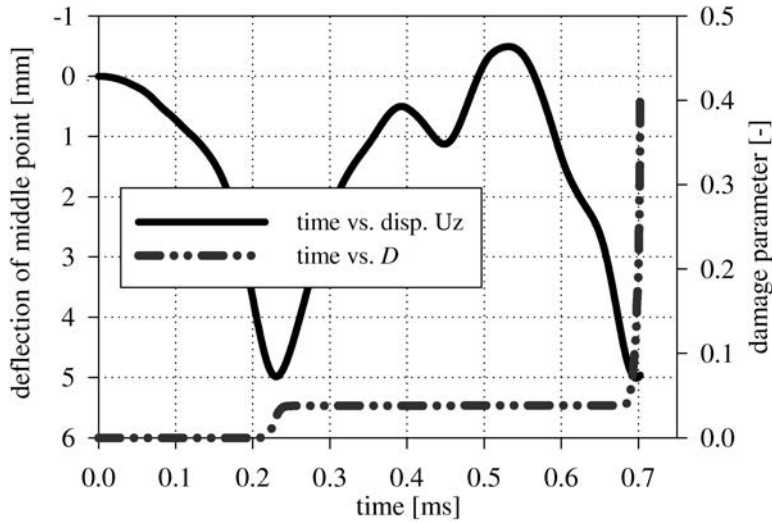
Fig. 25. Displacement diagram with damage parameter evolution.

of the proposed procedure for damage analysis. It should be noted that the subroutine UACTIV [34] was used to deactivate elements in the structure model, when the value of the damage parameter D in all integration points of the element is greater than the value of critical damage D_c. The vertical displacements for the quarter of a plate are presented in Fig. 24. The elements close to symmetry lines are deactivated due to evolution of the damage parameters, see Fig. 25. Then the crack runs to a diagonal of the plate. Finally, the middle part of the plate separates and moves rigidly. The author is aware of the fact that the detailed investigation of the structure crack propagation is connected with dynamic crack problems and the knowledge of explosions (see e.g. NEMITZ [26], BASISTA and NOWACKI [8] and WŁODARCZYK [35] for details). Nevertheless, this calculated example demonstrates practical applications of the presented procedure.

6. CONCLUSIONS AND FINAL REMARKS

In this study, the author proposed an improved concept of identification and validation of damage parameters. A model of isotropic damage based on a continuum damage variable on the concept of effective stress, can be directly applied in calculations. The procedures are presented to introduce the Chaboche model considering damage, into the open commercial FE-program code. Identification is made for nickel-based superalloy INCO718 and for steel by means of elastic modulus change caused by damage. The numerical examples prove that the Chaboche law and the presented method of performing the numerical implementation, are

effective. The future research should be concentrated on the development of the FE procedure, with emphasis placed on temperature influences and criterion for crack extension.

It is worth pointing out that the presented damage approach with the concept of damage parameters identification has been successfully used by the present author to describe the damage evaluation in the elasto-viscoplastic constitutive equations of the Bodner–Partom model, (for details see [5]).

References

1. J. Aktaa, B. Schinke, *Unified modelling of time dependent damage taking into account an explicit dependency on backstress,* International Journal of Fatigue, **19**, 3, 195–200, 1997.

2. G. Amar, J. Dufailly, *Identification of viscoplastic and damage constitutive equations*, European Journal of Mechanics, **12**, 2, 197–218, 1985.

3. A. Ambroziak, *Application of elasto-viscoplastic Bodner-Partom constitutive equations in finite element analysis*, Computer Assisted Mechanics and Engineering Sciences (in press).

4. A. Ambroziak, *Chaboche model – development and FE application*, Zeszyty Naukowe Politechniki Śląskiej, **104**, 35–42, 2005.

5. A. Ambroziak, *Modelling of continuum damage for application in elasto-viscoplastic Bodner-Partom constitutive equations*, Engineering Transactions (in press).

6. A. Ambroziak, *Numerical modelling of elasto-viscoplastic Chaboche constitutive equations using MSC. Marc*, Task Quarterly, **9**, 2, 157–166, 2005.

7. A. Ambroziak, *Viscoplastic analysis of damped vibrations of circular plate, [in:] Shell Structures: Theory and applications*, W. Pietraszkiewicz and C. Szymczak [Eds.], Taylor and Francis, London, 445–449, 2005.

8. M. Basista, W.K. Nowacki [Eds.] *Modelling of damage and fracture processes in engineering materials*, In Series: Trends in Mechanics of Materials. Volume 2, IPPT PAN, Warsaw 1999.

9. A. Bertram, J. Olschewski, *Anisotropic creep modelling of single crystal superalloy SRR99,* Journal of Computational Mathematic Science, **5**, 12–16, 1996.

10. S.R. Bodner, Y. Partom, *Constitutive equations for elastic-viscoplastic strain-hardening materials*, Journal of Applied Mechanics, ASME, **42**, 385–389, 1975.

11. W. Brocks, R. Lin, *An extended Chaboche viscoplastic law at finite strains and its numerical implementation*, GKSS-Forschunszentrum Geesthacht GmbH, Geesthacht 2003.

12. J.-L. Chaboche, *Constitutive equations for cyclic plasticity and cyclic viscoplasticity*, International Journal of Plasticity, **5**, 247–302, 1989.

13. J.-L. Chaboche, G. Rousselier, *On the plastic and viscoplstic constitutive equations*, International Journal of Pressure Vessels and Pining, **105**, 105–164, 1983.

14. P. Fotiu, H. Irschik, F. Ziegler, *Material science and numerical aspects in the dynamics of damaging structures*, [in:] Structural dynamics, G.I. Schueler [Ed.], Springer-Verlag, New York, 235–255, 1991.

15. T. Furakawa, G. Yagawa, *Inelastic constitutive parameter identification using an evolutionary algorithm with continuous individuals*, International Journal for Numerical Methods in Engineering, **40**, 1071–1090, 1997.

16. D.R. Hayhurst, F.A. Leckie, *The effect of creep constitutive and damage relations upon the rapture time of a solid circular torsion bar*, Journal of the Mechanics and Physics of Solids, **21**, 431-446, 1973.

17. L.M. Kachanov, *Introduction to continuum damage mechanics*, Martinus Nijhoff Publishers, Dordecht, 1986.

18. L.M. Kachanov, *Time of rapture process under creep conditions*, TVZ Akad. Nauk. S.S.R. Otd. Tech. Nauk., **8**, 26–31, 1958.

19. P. Kłosowski, *Nonlinear numerical analysis and experiments on vibrations of elasto-viscoplastic plates and shells* [in Polish], Politechnika Gdańska, Gdańsk 1999.

20. P. Kłosowski, K. Woznica, *Comparative analysis of dynamic behaviour of an elasto-viscoplastic truss element*, Machine Dynamics Problems, **24**, 3, 33–53, 2000.

21. F.A. Leckie, *The constitutive equations of continuum creep damage mechanics*, Philosophical Transactions of the Royal Society of London, **288**, 27–47, 1978.

22. J. Lemaitre, *Micro-mechanics of crack initiation*, International Journal of Fracture, **42**, 247–302, 1989.

23. J. Lemaitre, *A continuous damage mechanics. Model for ductile fracture*, Journal of Engineering Materials and Technology, **107**, 83–89, 1985.

24. J. Lemaitre, *A course on damage mechanics*, Springer-Verlag, New York 1992.

25. J. Lemaitre, A. Plumtree, *Application of damage concept to predict creep-fatigue failures*, Journal of Engineering Material and Technology, **101**, 284–292, 1979.

26. A. Nemitz, *Crack mechanics* [in Polish], PWN, Warsaw 1998.

27. N.M. Newmark, *A method of computation for structural dynamics*, Journal of the Engineering Mechanics Division, **85**, 67–94, 1959.

28. W.K. Nowacki, J.R. Klepaczko [Eds.], *New experimental methods in material dynamics and impact.* in Series: Trends in Mechanics of Materials, Volume 3, IPPT PAN and CoE AMAS, Warsaw 2001.

29. P. PERZYNA, *Fundamental problems in viscoplasticity*, Advanced in Mechanics, **9**, 243–377, 1966.

30. W. QI, W. BROCK, *ABAQUS user subroutines for simulation of viscoplastic behaviour including anisotropic damage for isotropic materials and for single crystals*, Technical Note GKSS/WMS/01/5, GKSS-Forschunszentrum Geesthacht GmbH, Geesthacht 2001.

31. Y.N. RABOTNOV, *Creep problems of structural members*, North-Holland, Amsterdam, 1969.

32. J.C. SIMO, J.W. JU, *Strain- and stress-based continuum damage models*, International Journal of Solids and Structures, **23**, 7, 821–869, 1987.

33. J. SKRZYPEK, H. KUNA-CISAŁKA, A. GARNCARSKI, *Continuum damage mechanics modelling of creep-damage and elastic-damage-fracture in materials and structures*, [in:] *Modelling of damage and fracture processes in engineering materials*, BASISTA M., NOWACKI W.K. [Eds.], Institute of Fundamental Technology Research Polish Academy of Science, Warsaw 1999.

34. Users handbook MSC.MARC, Volume B: Element library; Volume D: User subroutines and special routines, Version 2003, MSC. Software Corporation, 2003.

35. E. WŁODARCZYK, *Introduction to mechanic of explosion* [in Polish], PWN, Warsaw 1994.

36. K. WOZNICA, *Dynamique des structures elasto-viscoplastiques*, Cahiers de Mécanique, Lille 1998.

37. A. AMBROZIAK, P. KŁOSOWSKI, *Survey of modern trends in analysis of continuum damage in mechanics*, Task Quarterly, **10**, 4, 437–454, 2006.

38. A. AMBROZIAK, P. KŁOSOWSKI, M. NOWICKI, R. SCHMIDT, *Implementation of continuum damage in elasto-viscoplastic constitutive equations*, Task Quarterly, **10**, 2, 207–220, 2006.

INFLUENCE OF TRANSVERSE SHEARING AND ROTARY INERTIA ON VIBRATIONS OF A FIBROUS COMPOSITE BEAMS

J. G o ł a ś

University of Technology and Life Sciences in Bydgoszcz

S. Kaliskiego 7, 85-796 Bydgoszcz, Poland

The aim of the paper was determination of the influence of transverse shear deformation and rotary inertia on the natural frequencies and on the values of displacements of beams made of fibrous composites reinforced with layers of long fibres. It was assumed that the matrix of the composite beam possesses linear elastic and transversally isotropic properties. Moreover, a reinforcement in the form of layers composed of long fibres symmetrically located in the cross-section was considered. In order to describe the displacement and strain state of the matrix, the Timoshenko theory was applied. Using the complete analytical solutions obtained in the paper, the accuracy analysis of the results was performed and compared with the theory of Bernoulli beams.

Key words: dynamics of composite beam, transverse shear effect.

1. Introduction

Fibrous composites are playing an increasing role as construction materials in a wide variety of applications. They are used in civil engineering and chemical, aerospace and shipbuilding industries. The composites composed of the matrix reinforced with long fibres (see Fig. 1), are characterized by high strength capability, lightness and significant transversal non-homogeneity.

Technical application of fibrous composite materials requires to take into considerations their shear deformation vulnerability in order to carry out the strength calculations [1–6]. Theoretical and experimental investigations show that the use of the classical assumption about the non-deformability of the normal section makes the values of the calculated displacements (deflections) lower. On the other hand, it increases both the critical loads and the natural frequencies [3]. The errors connected with neglecting the influence of shear deformation on the vibrations of fibrous composite beam follow not only from the relation h/l and the load type but also from the relation E^r/E (Young's modulus of the fibres to Young's modulus of the matrix) and from the fibre density and its location in the cross-section [4, 5].
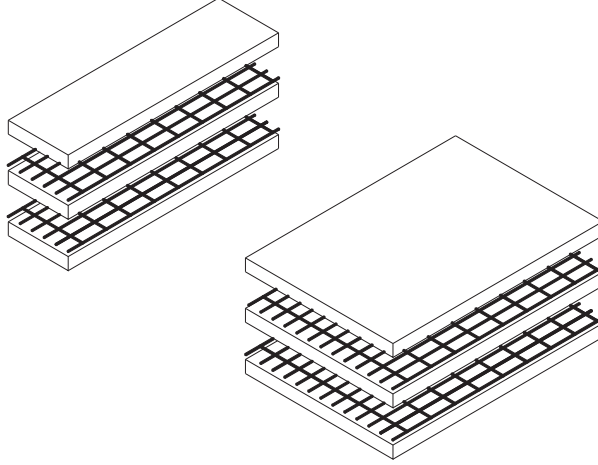
Fig. 1. Construction element reinforced with the layers of long fibres.

The aim of this study is to determine the influence of the transverse shear deformations and rotary inertia on the natural frequencies and on the displacement field of beams made of fibrous composites reinforced by layers of long fibres.

The composite can be defined as a material consisting of at least two components. The first component constitutes the main phase (matrix). The second one, immersed in the matrix, constitutes the fibrous phase (2-nd phase). The fibrous phase consists of any amount of *families*. The *family* is a group of long fibres lying in the planes parallel to the neutral axis of the beam. The fibres belonging to the *family* are thin, straight and so densely packed that a continuous model can be assumed. We assume that the two phases meet the continuity criteria both in the sense of displacements and strains. As a consequence of the above assumptions, we can take into consideration a theoretical model in the form of a continuous double-phase medium. In such model the *continuum* of the 1-st phase is immersed in the *continuum* of the 2-nd phase. The idea of the model presented herein was taken from the papers by HOLNICKI-SZULC [7] and ŚWITKA [8].

The dynamic problem of beams and plates made of transversally isotropic material has been investigated by a number of authors, e.g. NOWACKI [9], KĄCZKOWSKI [10], SZCZEŚNIAK [11, 12], JEMIELITA [13]. For a wide literature review of the problem see [10, 12, 13].

2. Formulation of the problem

Let us analyse the transverse vibration problem of a fibrous composite prismatic beam (cross-section $b \times h$) in xz-plane (see Fig. 2). Applying the Timo-

shenko theory, displacements of any point of the cross-section can be described using the equations

(2.1)
$$u_x\left(x, z, t\right) = u\left(x, t\right) + z\psi\left(x, t\right);$$
$$u_y\left(x, z, t\right) = 0; \qquad u_z\left(x, z, t\right) = w\left(x, t\right);$$

where u and w denote respectively horizontal and vertical components of the displacement vector for points lying on the neutral axis. The ψ is the angle of rotation of the cross-section.
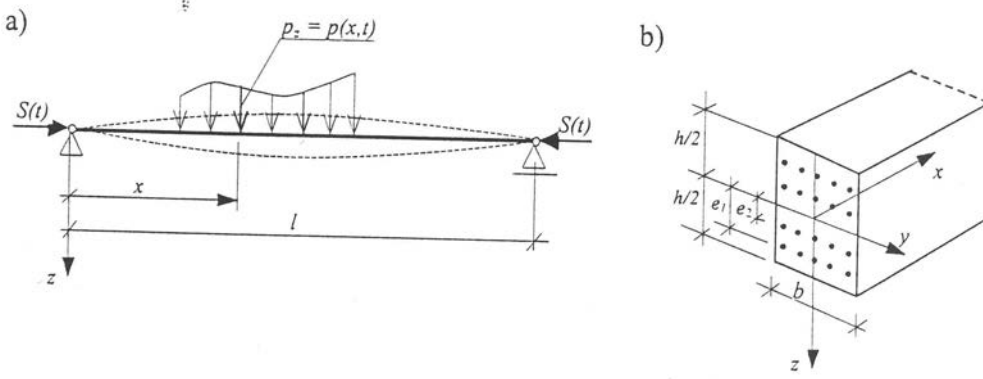
FIG. 2. Simply supported beam loaded by transverse load $p(x, t)$ and by axial load $S(t)$: a) model, b) example of the symmetric reinforcement of the cross-section with two pairs of long fibre families.

The strains of the beam are given by

(2.2) $$\varepsilon_x = \frac{\partial u_x}{\partial x} = \frac{\partial u}{\partial x} + z\frac{\partial \psi}{\partial x}; \qquad \gamma_{xz} = \frac{\partial u_x}{\partial z} + \frac{\partial u_z}{\partial x} = \psi + \frac{\partial w}{\partial x}.$$

In this work we assume that the matrix is made of the transversally isotropic perfectly elastic material obeying Hooke's relations

(2.3) $$\sigma_x = E\varepsilon_x; \qquad \tau_{xz} = G'\gamma_{xz}.$$

The fibre phase (reinforcement) consists of symmetrically located vertical layers of fibrous *families*. Each *family* consists of continuous, straight fibres coinciding with the x-axis and lying in planes $z = z^r$ ($r = 1, 2, 3...$), $z^r \in (-h/2,\ h/2)$. The fibres of each *family* are thin, densely packed and support only axial loads. We assume that the fibres are made of linear elastic material which much higher strength coefficients than the coefficients of the matrix. The force in the r-th *family* is given by

(2.4) $$S_x^r = j^r E^r A^r\left(\varepsilon_x^r - \varepsilon_x^{or}\right),$$

where ε_x^r, ε_x^{or}, E^r, A^r and j^r mean respectively the unit elongation, the initial distortion, the Young's modulus, the cross-section area of the fibre and the amount of fibres in the *family*.

We assume in the paper a perfect adherence between the matrix surface and the fibres surfaces, so that the resultant internal forces in the composite beam can be calculated as a sum of forces in the beam's components.

$$(2.5) \quad N = \int_A \sigma_x dA + \sum_r S_x^r; \qquad M = \int_A \sigma_x z dA + \sum_r S_x^r z^r; \qquad T = \int_A \tau_{xz} dA.$$

Making use of Eqs. (2.2), (2.3), (2.4) and assuming the amount of i equal pairs of fibre *families* to be symmetrically located in the cross-section at the distances $z^r = \pm e_1, \ \pm e_2, \ .... \pm e_i; \quad e_i \in (0, \ h/2)$, and also neglecting initial elongation of the fibres, Eqs. (2.5) take the form

$$(2.6) \qquad N = B\frac{\partial u}{\partial x}; \qquad M = D\frac{\partial \psi}{\partial x}; \qquad T = G'Ak\left(\psi + \frac{\partial w}{\partial x}\right),$$

where

$$(2.7) \qquad B = EA + 2ij^r E^r A^r, \qquad D = EJ + 2j^r E^r A^r \sum_i e_i^2$$

represent the respectively the tension/compression stiffness of the beam and its bending stiffness [6]. Moreover $A = bh; \quad J = bh^3/12; \quad G'$ – shear modulus of the matrix, $k = 5/6$.

We formulate the equations of motion of a straight prismatic beam based on the Hamilton principle. The assumption that the variations of displacements for the times t_0 and t_1 are equal to zero, gives the following variational equation:

$$(2.8) \qquad \int\limits_{t_0}^{t_1} \left\{ \int\limits_0^l \left[-\left(\frac{\partial N}{\partial x} - \rho A\ddot{u}\right)\delta u - \left(\frac{\partial M}{\partial x} - T - \rho J\ddot{\psi}\right)\delta\psi \right.\right.$$

$$\left. -\left(\frac{\partial T}{\partial x} - S\frac{\partial^2 w}{\partial x^2} + p_z - \rho A\ddot{w}\right)\delta w\right] dx$$

$$\left. + N\delta u|_0^l + M\delta\psi|_0^l + \left(T - S\frac{\partial w}{\partial x}\right)\delta w|_0^l \right\} dt = 0,$$

to be satisfied for any value of functions δu, $\delta\psi$ and δw. In the above expression $p_z = p(x,t)$ denotes the external transversally distributed load, $S(t)$ denotes the external axial force, symbol ρ denotes density and $\rho J\ddot{\psi}$ is the moment of rotary inertia. Dots denote differentiation with respect to the time coordinate t.

The Eq. (2.8) implicates the system of three equations of motion:

$$\frac{\partial N}{\partial x} - \rho A \ddot{u} = 0,$$

(2.9)
$$\frac{\partial M}{\partial x} - T - \rho J \ddot{\psi} = 0,$$

$$\frac{\partial}{\partial x}\left(T - S\frac{\partial w}{\partial x}\right) - \rho A \ddot{w} = -p\left(x, t\right),$$

and the appropriate natural boundary conditions. Analysing the uncoupled problem of axial and transverse vibration, we obtain in the first case two combinations of possible conditions for each boundary. In the case of pure transverse vibration, the number of combinations of boundary conditions is equal to four. The initial conditions correspond to the displacements u, ψ and w, and their velocities.

3. Influence of the rotary inertia on the natural frequencies

First of all let us determine the order of magnitude of the influence of the cross-section rotary inertia $\rho J \ddot{\psi}$ on the transverse natural frequencies of a composite beam.

Using the equations of motion (2.9) we obtain, taking into consideration the constitutive equations (2.6) and eliminating the variable ψ, the following differential equation describing the eigenvalue problem

(3.1)
$$D\frac{\partial^4 w}{\partial x^4} + \rho A \ddot{w} - \rho J \frac{\partial^2 \ddot{w}}{\partial x^2} - \frac{\rho D}{G'k}\frac{\partial^2 \ddot{w}}{\partial x^2} + \frac{\rho^2 J}{G'k}\ddddot{w} = 0.$$

The 3-rd and 5-th components in Eq. (3.1) express the influence of the rotary inertia and the 4-th component corresponds to the influence of the transverse shear deformation.

In the case of a simply supported beam, the Eq. (3.1) will be satisfied if

(3.2)
$$w\left(x, t\right) = A_n e^{-i\omega_n t}\sin\alpha_n x, \qquad n = 1, 2, 3, ...$$

where A_n denotes the deflection amplitude, ω_n means the natural frequency and $\alpha_n = \dfrac{n\pi}{l}$.

Substituting (3.2) into (3.1) gives

(3.3)
$$\beta^2\alpha_n^4 - \omega_n^2 - \frac{J}{A}\alpha_n^2\omega_n^2 - \frac{D}{G'kA}\alpha_n^2\omega_n^2 + \frac{\rho J}{G'kA}\omega_n^4 = 0,$$

where $\beta^2 = \dfrac{D}{\rho A}$.

If we take into consideration only the first two components in the Eq. (3.3), then we will obtain the formula to calculate the natural frequencies of a slender beam obeying the Bernoulli hypothesis

$$(3.4) \qquad \omega_n^2 = \beta^2 \alpha_n^4, \qquad n = 1, 2, 3, \ldots$$

In the expression (3.4) the influence of the shear deformations and the rotary inertia effect is not taken into account.

Substituting (3.4) into the last component of (3.3), as the first approximation, we notice that this component can be treated as a small 2-nd order term with respect to other components, so it can be neglected [9].

Making use of the above remarks, the Eq. (3.3) gives

$$(3.5) \qquad \omega_n = \frac{\beta \alpha_n^2}{\sqrt{1 + \dfrac{J}{A} \alpha_n^2 \left(1 + \dfrac{D}{G' k J}\right)}} \approx \beta \alpha_n^2 \left[1 - \frac{1}{2} \frac{J}{A} \alpha_n^2 \left(1 + \frac{D}{G' k J}\right)\right],$$

$$n = 1, 2, 3, \ldots$$

If we assume in (3.5) the value of inertia J to vanish, we will obtain the formula to calculate the natural frequencies respecting only the influence of the shear deformation

$$(3.6) \qquad \omega_{np} = \frac{\beta \alpha_n^2}{\sqrt{1 + n^2 \pi^2 \zeta}} \approx \beta \alpha_n^2 \left(1 - \frac{1}{2} n^2 \pi^2 \zeta\right).$$

Taking $G' = \infty$ we obtain the expression

$$(3.7) \qquad \omega_{nb} \approx \beta \alpha_n^2 \left(1 - \frac{1}{2} \frac{J}{A} \alpha_n^2\right),$$

respecting only the influence of the rotary inertia.

Let us apply the following coefficient in (3.6):

$$(3.8) \qquad \zeta = \frac{D}{G' k A l^2}.$$

It characterizes the shear deformability of the composite beam [6]. By using $(2.7)_2$ and taking $E \big/ G' = 2(1 + \nu)$, the coefficient ζ becomes

$$(3.9) \qquad \zeta = \frac{(1 + \nu) h^2}{5 l^2} \left(1 + 24 n^r \mu^r \sum_i \frac{e_i^2}{h^2}\right).$$

Equation (3.9) shows that the coefficient ζ strongly depends on the parameters h/l, $n^r = E^r/E$ (Young's modulus of the fibres to Young's modulus of the matrix), $\mu^r = j^r A^r/A$ (density of fibre packages in the r-th *family*) and e_i/h (location of the *family* of fibres in the cross-section). Figure 3 presents the diagram of the coefficient ζ as a function of the beam slenderness l/h and of the ratio E^r/E with $\nu = 0.30$; $\mu^r = 0.02$; $i = 2$, $e_1 = 0.45h$ and $e_2 = 0.35h$.
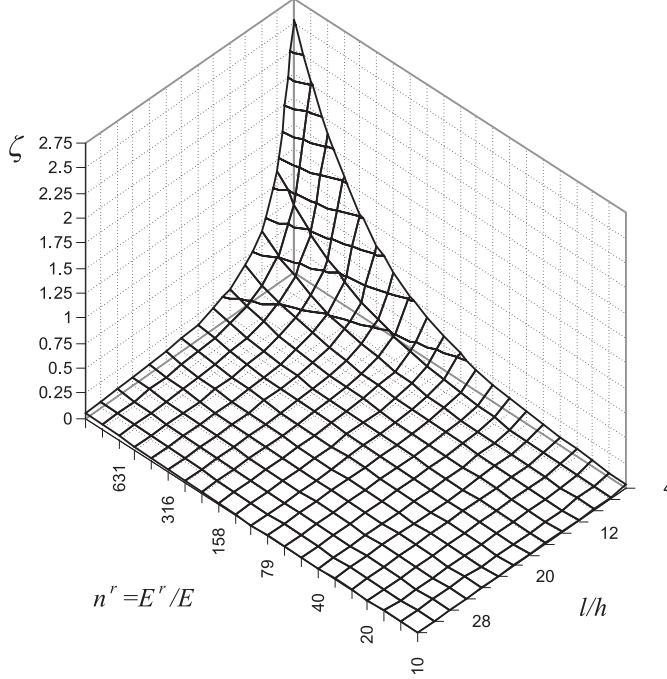
FIG. 3. Coefficient ζ as a function of the beam slenderness l/h and of the ratio of Young's moduli E^r/E.

The relative errors ε_p and ε_b resulting from neglecting of the influence of shear deformations and rotary inertia with respect to the natural frequency (3.4) of the slender composite beam are as follows, if we take into account (3.6) and (3.7):

$$(3.10) \qquad \varepsilon_p = \frac{|\omega_n - \omega_{np}|}{\omega_n} \cdot 100\% = \frac{1}{2} n^2 \pi^2 \zeta \cdot 100\%,$$

$$(3.11) \qquad \varepsilon_b = \frac{|\omega_n - \omega_{nb}|}{\omega_n} \cdot 100\% = \frac{n^2 \pi^2 J}{2l^2 A} \cdot 100\%.$$

The relation

$$(3.12) \qquad \frac{\varepsilon_p}{\varepsilon_b} = \frac{D}{G'kJ} = \frac{E}{G'k} \left(1 + 24 \sum_i n^r \mu^r \frac{e_i^2}{h^2} \right)$$

states how much the influence of the shear deformation is greater than the influence of the rotary inertia. Taking for example $E/G' = 2.6$; $i = 2$ (two pairs of identical fibre *families* in the cross-section), $n^r = 20$; $\mu^r = 0.02$ (4% of reinforcement), $e_1 = 0.45h$; $e_2 = 0.35h$ we obtain $\varepsilon_p/\varepsilon_b = 12.85$. This leads to the conclusion that *for the composite beams with reinforcement by layers of long fibres, the influence of shear deformation on the natural frequencies is at least one order of magnitude greater than the influence of rotary inertia.*

Taking into account the above conclusion we will neglect the influence of the rotary inertia of the cross-section on the vibration of composite beams.

The relative error ε_p caused by neglecting the influence of shear deformation with the length of deformation wave $l/n = 10h$ and $5h$ (where h denotes the cross-section height), is equal to 5.3% and 21.1% respectively (keeping remaining input values unchanged). So we can easily observe that the error is significant and increases in proportion to the coefficient ζ.

Thus, taking into account the influence of shear deformations only, we obtain the natural frequencies for a simply supported composite beam in the form (3.6). The associated eigenmodes are expressed in the form

$$(3.13) \qquad W_n(x) = A_n \sin \alpha_n x; \qquad \Psi_n(x) = B_n \cos \alpha_n x.$$

4. HARMONICALLY FORCED VIBRATION

In the case of beam vibration forced by transverse load $p(x,t) = p(x) e^{-i\omega t}$, neglecting the influence of axial loads and rotary inertia, the system of Eqs. (2.9) transforms into the system of uncoupled equations of motion

$$
\begin{aligned}
&\frac{\partial^4 w}{\partial x^4} + \frac{\rho A}{D}\left(1 - \zeta l^2 \frac{\partial^2}{\partial x^2}\right)\ddot{w} = \frac{1}{D}\left(1 - \zeta l^2 \frac{\partial^2}{\partial x^2}\right) p(x,t),\\[2mm]
&\frac{\partial^4 \psi}{\partial x^4} + \frac{\rho A}{D}\left(1 - \zeta l^2 \frac{\partial^2}{\partial x^2}\right)\ddot{\psi} = -\frac{1}{D}\frac{\partial}{\partial x} p(x,t).
\end{aligned}
$$

(4.1)

As a result of the load acting harmonically, the displacement $w(x,t)$ and the angle of rotation $\psi(x,t)$ varies also harmonically

$$(4.2) \qquad w(x,t) = W(x) e^{-i\omega t}; \qquad \psi(x,t) = \Psi(x) e^{-i\omega t}.$$

Substituting (4.2) into (4.1) gives the following ordinary differential equations:

$$
\begin{aligned}
&\frac{d^4 W(x)}{dx^4} - \omega^2 \frac{\rho A}{D}\left(1 - \zeta l^2 \frac{d^2}{dx^2}\right) W(x) = \frac{1}{D}\left(1 - \zeta l^2 \frac{d^2}{dx^2}\right) p(x),\\[2mm]
&\frac{d^4 \Psi(x)}{dx^4} - \omega^2 \frac{\rho A}{D}\left(1 - \zeta l^2 \frac{d^2}{dx^2}\right) \Psi(x) = -\frac{1}{D}\frac{dp(x)}{dx},
\end{aligned}
$$

(4.3)

completed by the appropriate boundary conditions. For a simply supported beam we should assume $W(0) = W(l) = 0$ and $\dfrac{d\Psi(0)}{dx} = \dfrac{d\Psi(l)}{dx} = 0$.

Taking

$$W(x) = \sum_{n=1}^{\infty} A_n \sin \alpha_n x;$$

(4.4)
$$\Psi(x) = \sum_{n=1}^{\infty} B_n \cos \alpha_n x;$$

$$p(x) = \sum_{n=1}^{\infty} p_n \sin \alpha_n x$$

and making use of the Fourier transform [9] in order to solve the Eqs. (4.3), leads to the following solution of the equations of motion (4.1):

$$w(x,t) = \frac{2}{l}\frac{e^{-i\omega t}}{\rho A} \sum_{n=1}^{\infty} \frac{\sin \alpha_n x}{\omega_n^2 \left(1 - \dfrac{\omega^2}{\omega_n^2}\right)} \int_0^l p(u) \sin \alpha_n u\, du,$$

(4.5)

$$\Psi(x,t) = -\frac{2}{l}\frac{e^{-i\omega t}}{\rho A} \sum_{n=1}^{\infty} \frac{\alpha_n \cos \alpha_n x}{(1 + n^2\pi^2\zeta)\,\omega_n^2 \left(1 - \dfrac{\omega^2}{\omega_n^2}\right)} \int_0^l p(u) \sin \alpha_n u\, du,$$

where ω denotes the frequency of excitation and ω_n denotes the natural vibration frequency.

In the case of the load being uniformly distributed along the beam $p(x,t) = pe^{-i\omega t}$ or for the concentrated load $p(x,t) = P\delta(x - \xi)\,e^{-i\omega t}$ acting in the section $x = \xi$, we obtain respectively

$$w(x,t) = \frac{4pe^{-i\omega t}}{lD} \sum_{n=1,3,5,\ldots} \frac{(1 + n^2\pi^2\zeta)}{\alpha_n^5 \left(1 - \dfrac{\omega^2}{\omega_n^2}\right)} \sin \alpha_n x,$$

(4.6)

$$\Psi(x,t) = -\frac{4pe^{-i\omega t}}{lD} \sum_{n=1,3,5,\ldots} \frac{\cos \alpha_n x}{\alpha_n^4 \left(1 - \dfrac{\omega^2}{\omega_n^2}\right)},$$

and

$$w\left(x,t\right)=\frac{2Pe^{-i\omega t}}{lD}\sum_{n=1}^{\infty}\frac{\left(1+n^2\pi^2\zeta\right)}{\alpha_n^4\left(1-\dfrac{\omega^2}{\omega_n^2}\right)}\sin\alpha_nx\sin\alpha_n\xi,$$

(4.7)

$$\Psi\left(x,t\right)=-\frac{2Pe^{-i\omega t}}{lD}\sum_{n=1}^{\infty}\frac{\cos\alpha_nx\sin\alpha_n\xi}{\alpha_n^3\left(1-\dfrac{\omega^2}{\omega_n^2}\right)}.$$

The solutions describing the harmonic motion problem for simply supported composite shearing-sensitive beam we have obtained above, can be used to evaluate the solutions of the slender reinforced beam problem. We just need to eliminate the shear deformation γ_{xz} by substituting $G' \to \infty$ or $\zeta = 0$ into Eqs. (3.6), (3.8), (4.1), (4.3), (4.5), (4.6) and (4.7). If we assume additionally $A^r = 0$ (elimination of the fibre phase), we will obtain appropriate solutions for the homogeneous beam [9].

The limiting case when $\omega \to 0$ gives the static problem. Thus, considering the uniformly distributed load p or the concentrated load P acting in the midspan of the beam, we will obtain the following extremal values of displacement components using (4.6) and (4.7):

(4.8) $\qquad w\left(l/2\right)=\dfrac{5}{384}\dfrac{pl^4}{D}\left(1+9.6\zeta\right);\qquad \Psi\left(0\right)=-\dfrac{pl^3}{24D}=-\Psi\left(l\right),$

(4.9) $\qquad w\left(l/2\right)=\dfrac{Pl^3}{48D}\left(1+12\zeta\right);\qquad \Psi\left(0\right)=-\dfrac{Pl^2}{16D}=-\Psi\left(l\right).$

Taking additionally $\zeta = 0$ leads to the solution of the slender beam obeying the Bernoulli hypothesis.

5. Parametric study

The aim of the analysis is to determine the influence of shear deformations on the values of deflections of the composite beam we deal with in this paper. As we have mentioned before, the girders made of fibrous composites are reinforced using fibres characterised by much better mechanical properties than the matrix properties. The fibres exhibit significant shear deformability. The use of Bernoulli hypothesis is suitable for isotropic slender beams. Because of it, a direct application of this hypothesis to solve the fibrous composite beam problem seems to be inappropriate and leads to significant errors.

The relative error connected with omitting the shear deformations to be calculated for extremal deflections

$$(5.1) \qquad \varepsilon = \frac{|w - w_B|}{|w_B|} \cdot 100\%,$$

taking into account (4.8) and (4.9) becomes, in the case of uniformly distributed load,

$$(5.2) \qquad \varepsilon = 9.6\zeta \cdot 100\%.$$

For the concentrated load, the relative error

$$(5.3) \qquad \varepsilon = 12\zeta \cdot 100\%$$

is 25% greater than the distributed load error. In the Eq. (5.1), symbol w_B denoting the deflection calculated according to the slender beams theory was used.

In order to demonstrate the influence of the beam slenderness changes l/h and of the ratio $n^r = E^r/E$ on the value of the error ε to be committed, let us take for example the data identical as before (see Fig. 3).

The calculated values of the error ε are presented in Table 1 and visualised in Fig. 4.
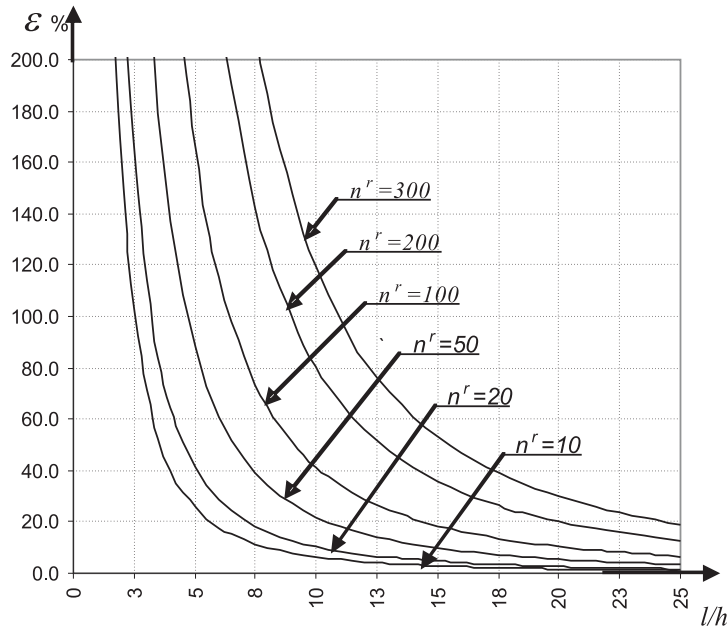
FIG. 4. Influence of the beam slenderness changes l/h and of the ratio $n^r = E^r/E$ on the value of the relative error ε caused by disregarding the transverse shear deformations effect.

Table 1.

ε %		l/h					
		25	20	15	10	8	4
$n^r = \dfrac{E^r}{E}$	10	1.02	1.60	2.84	6.39	9.98	39.9
	20	1.65	2.57	4.57	10.3	16.1	64.3
	50	3.52	5.49	9.77	22.0	34.3	137.3
	100	7.05	10.4	18.4	41.4	64.7	265.2
	200	12.88	20.1	35.7	80.4	125.6	502.3
	300	19.12	29.8	53.1	119.3	186.4	745.7

6. Conclusions

The complete analytical results obtained in the paper as well as the analysis carried out show that considering the influence of the transverse shear deformations in the dynamic problem of fibrous composite beams reinforced by layers of long fibres, strongly influences the natural frequencies and displacements to be calculated.

This influence depends mainly on the vulnerability parameter ζ which strongly depends on the parameters h^2/l^2, $n^r = E^r/E$, $\mu^r = j^r A^r/A$ (density of fibres' locations in the r-th *family*) and e_i/h (location of the *family* of fibres in the cross-section) and on the way the load is distributed.

The influence of shear deformations on the behaviour of a homogenous beam (without reinforcement) with the ratio $l/h \geq 10$ is negligible. An important fact we have presented in the paper is that for the composite beam possessing the same slenderness ratio, this influence is significant and may reach the values greater than 100% (see Table 1).

However, the influence of the rotary inertia on the eigenvalues of composite beams is over ten times smaller than the influence of shear deformations. Thus it may be neglected.

References

1. R.K. KAPANIA, S. RACITI, *Recent advances in analysis of laminated beams and plates*, Part I. *Shear effects and buckling.* AIAA J., **27**, 7, 923–934, 1989; Part II. *Vibrations and wave propagation.* AIAA J., **27**, 7, 935–946, 1989.

2. A.K. MALMEISTER, V.P. TAMUŻ, G.A TETERS, *Strength of polymeric and composite materials* [in Russian], Zinatne, Riga 1980.

3. J.N. REDDY, N.D. PHAN, *Stability and vibration of isotropic, orthotropic and laminated plates according to a higher – order shear deformation theory,* J. Sound and Vibr., **98**, 2, 157–170, 1985.

4. J. GOŁAŚ, *On limits of application of Kirchhoff's hypothesis in the theory of viscoelastic fibrous composite plates*, Engineering Transactions, **43**, 4, 603–626, 1995.

5. J. GOŁAŚ, *On necessity of making allowance for shear strain in cylindrical bending of fibre composite viscoelastic plates,* Archives of Civil Engineering, **43**, 2, 121–147, 1997.

6. J. GOŁAŚ, *Solution for Timoshenko beams expressed in terms of Euler-Bernoulli solutions for fibre-reinforced straight composite beams* [in Polish], Akademia Techniczno-Rolnicza, Zeszyty Naukowe Nr 228, Mechanika, **47**, 111–120, Bydgoszcz 2000.

7. J. HOLNICKI-SZULC, *Distortions in structural systems. Analysis, control, modelling* [in Polish], PWN, Warszawa–Poznań 1990.

8. R. ŚWITKA, *Equations of the fibre composite plates,* Engineering Transactions, **40**, 2, 187–201, 1992.

9. W. NOWACKI, *Dynamics of elastic systems* [in Polish], Arkady, Warszawa 1961.

10. Z. KĄCZKOWSKI, *Dynamics of bars and bar structures* [in Polish], Mechanika Techniczna (Applied Mechanics), Vol. IX, 182–240, PWN, Warszawa 1988.

11. W. SZCZEŚNIAK, *Free vibrations of viscoelastic Timoshenko beam and shield* [in Polish], Engineering Transactions, **22**, 4, 669–687, 1974.

12. W. SZCZEŚNIAK, *Selected problems of dynamics of plates* [in Polish], Oficyna Wydawnicza PW, 2000.

13. G. JEMIELITA, *Problems of dynamics of plates* [in Polish], Mechanika Techniczna (Applied Mechanics), Vol. VIII, Cz. WOŹNIAK [Ed.], PWN, Warszawa 296–330, 2001.

ON MICRO-DAMAGE IN HOT METAL WORKING
PART 2: CONSTITUTIVE MODELLING

J. L i n[1], A. D. F o s t e r[1], Y. L i u[1]
D. C. J. F a r r u g i a[2], T. A. D e a n[1]

[1]**Department of Manufacturing and Mechanical Engineering**
School of Engineering
University of Birmingham
Edgbaston, Birmingham B15 2TT, UK

[2] **Corus R, D and T, Swinden Technology Centre**
Moorgate, Rotherham, S60 3AR, UK

Damage constitutive equations are formulated to model the evolution of grain boundary and plasticity-induced damage for free-cutting steels under hot forming conditions. During high temperature, high strain rate deformation, material degradation has characteristics of both creep damage at grain boundaries, and ductile damage surrounding hard inclusions. This has been experimentally observed and is reported in the companion paper. This paper describes the development of unified viscoplastic-damage constitutive equations, in which the nucleation and growth of both damage types are considered independently. The effects of deformation rate, temperature, and material microstructure on damage evolution are modelled. The proposed damage evolution equations are combined with a viscoplastic constitutive equation set, enabling the evolution of dislocation hardening, recovery, recrystallisation, grain size, and damage to be modelled. This set of unified, mechanism-based, viscoplastic damage constitutive equations is determined from experimental data of a free-machining steel for the temperature range 1173–1373 K. The fitted model is then used to predict damage and failure features of the same material tested using a set of interrupted constant strain rate tests. Close agreement between the predicted and experimental results is obtained for all the cases studied.

Key words: creep damage, ductile damage, constitutive equations, hot metal forming, viscoplasticity.

NOTATIONS

ε_p	plastic strain,
ε_T	total strain,
A_1, A_2, γ_1	material constants in plastic strain rate law,
d	average grain size,
d_0	material constant for grain size dependence,
R	isotropic hardening parameter,
k	material yield stress,

S	recrystallised fraction,
$\bar{\rho}$	normalised dislocation density,
$\bar{\rho}_c$	material-dependent critical dislocation density for recrystallisation,
x	recrystallisation onset parameter,
H_1, λ_1	material constants in recrystallisation law,
δ_1, δ_2	material constants in dislocation accumulation law,
C_r, δ_3	material constants in dislocation recovery law,
C_S	material constant in dislocation annihilation by recrystallisation law,
X_1	material constant in recrystallisation onset law,
B	material constant in isotropic hardening law,
G_1, ψ_1	material constants in normal grain growth law,
G_2, ψ_2	material constants in grain size evolution law,
E	Young's modulus of material,
σ	residual stress,
D_T	total damage,
D_{GB}	grain boundary damage,
D_{GB}^N, D_{GB}^G	grain boundary damage nucleation and growth,
η	grain size dependence parameter for grain boundary damage,
d_c	critical grain size parameter for grain boundary damage,
a_1, a_2, a_3, n_1	material constants in grain boundary damage accumulation law,
a_4	material constant in grain boundary damage nucleation law,
n_2	material constant in grain boundary damage growth law,
D_{Pi}	plasticity-induced damage,
D_{Pi}^N, D_{Pi}^G	plasticity-induced damage nucleation and growth,
a_5	material constant in plasticity-induced damage accumulation law,
a_6, n_3, n_4	material constants in plasticity-induced damage growth law,
Q_p, Q_{ac}, Q_{GG}	activation energy for i) dislocation-based plasticity,
	ii) dislocation recovery, iii) grain growth,
Q_{GB}, Q_{Pi}	activation energy for i) grain boundary damage,
	ii) plasticity induced damage,
κ, T	heat constant, temperature.

1. INTRODUCTION

Damage modelling is now recognised as a powerful tool for the understanding and prediction of the initiation of macro-cracks in materials processing. Hot metal forming processes inadvertently cause a concentrated build-up of micro-damage within the working material at areas, where hydrostatic stress is positive [1]. It is the accumulation of this damage that can cause macro-cracking observed on feedstock during rolling. Macroscopic cracks are formed when micro-damage features reach a critical density and start to coalesce. In commercial rolled steels, a uniform, high-quality product is essential. To achieve this, regions with a high damage density are removed, a process which is expensive and wasteful. By using a damage model to accurately determine the critically damaged region, yield can be increased and specified mechanical properties of processed materials achieved. To enable the grain boundary damage and plasticity-induced damage observed from experimentation of hot metal working conditions to be

modelled, relevant damage models for high temperature creep, plasticity and superplasticity are outlined first.

Since the original work on damage accumulation during high temperature creep by KACHANOV [2], continuum damage mechanics (CDM) has been applied to a range of deformation conditions. For the case of high temperature creep in which viscoplastic straining occurs predominantly by grain boundary sliding due to the grain boundary diffusion process, damage has been identified as occurring by several damage mechanisms, with the dominant mechanism depending on both the material and the strain rate. The damage types have been independently studied and modelled, for instance damage due to mobile dislocations in creep has been modelled by using the equation form [3]:

$$(1.1) \qquad \dot{D} = C\,(1 - D)^2\,\dot{\varepsilon}_c$$

in which D represents damage in a unit area (varying from an undamaged state of $D = 0$ to a totally damaged state at $D = 1$), $\dot{\varepsilon}_c$ is the creep strain rate, and C is a material constant. Damage due to creep constrained cavity nucleation and growth (occurring at grain boundaries) is typically represented by

$$(1.2) \qquad \dot{D} = W\dot{\varepsilon}_c,$$

where W is a material constant [4]. If high temperature creep takes place under high stress levels, cavity growth is the dominant damage mechanism. According to COCKS and ASHBY [5], damage due to cavity growth at grain boundaries is modelled by

$$(1.3) \qquad \dot{D} = \beta \left(\frac{1}{(1 - D)^n} - (1 - D) \right) \left(\frac{\sigma_e}{\sigma_0} \right) \cdot \dot{\varepsilon}_0$$

in which σ_0 and n denote material constants, $\dot{\varepsilon}_0$ is the material creep rate, and β is a material parameter related to hydrostatic stress.

Deformation at low temperatures occurs predominantly by the formation and slip of dislocations within grains. Under these conditions, ductile damage nucleates and grows around the second phase and other matrix discontinuities that attract a localised build up of dislocations. Detailed studies of ductile void growth have been conducted by RICE and TRACEY [6] and GURSON [1]. RICE and TRACEY [6] proposed a damage model based on the radial growth characteristics of a pre-existing void in a unit cell, considering in detail the volumetric growth and shape changes of a void. Later, Gurson's approximation of a rigid-plastic solid containing spherical cavities [1] considered the micro-effects of a growing void within a continuum lattice. The model gives a good representation of the early evolution of damage, however coalescence is presumed as being

solely due to adjacent cavities meeting – which leads to a large discrepancy be-
tween the predicted and actual failure conditions [7]. Phenomenologically based
ductile damage models have also been developed to model the damage accu-
mulation due to large plastic deformation. By considering void nucleation and
growth as separate terms, damage can be represented by the form [8]:

$$(1.4) \qquad \dot{D} = c \cdot \dot{\varepsilon}_e^p + (a_1 + a_2 \cdot D) \cdot \frac{K^2}{2E} \cdot (\varepsilon_e^p)^{2m} \cdot f\left(\frac{\sigma_H}{\sigma_e}\right) \cdot \dot{\varepsilon}_e^p$$

in which c, a_1, and a_2 are material-dependant constants, and K and m are harden-
ing parameters. The first term represents the rate of nucleation of new damage
sites, the second models the growth of existing voids. The function $f\left(\dfrac{\sigma_H}{\sigma_e}\right)$
describes the stress state dependence of void growth.

Damage accumulation during superplastic deformation has been identified
at grain boundaries [9] and around hard particles both at grain boundaries and
within grains [10]. A damage model to predict damage during superplastic de-
formation occurring by void nucleation and growth around particles has been
developed by KHALEEL [10] and takes the form:

$$(1.5) \qquad \dot{D} = \eta \cdot (1 - D) \cdot \dot{\varepsilon}_p + \frac{F(\varepsilon_p)}{(1 - D)} \cdot \sigma \cdot \dot{\varepsilon}_p,$$

where η is usually taken as a material constant and F is a monotonic function
of plastic strain.

The models discussed above are designed to predict particular types of dam-
age evolution and damage mechanisms. In the companion paper, an experimen-
tal programme conducted on a free-cutting steel has identified the simultane-
ous presence of two discrete types of damage. Cracks and voids along grain
boundaries and at triple points of adjacent grains (referred to as grain boundary
damage in this paper) have similarities to those noted during high temperature
creep (e.g. [11]) and superplastic deformation. Damage surrounding hard inclu-
sions due to debonding of the inclusion/matrix interface is similar to a damage
example considered by GURSON [1] and others in ductile rupture conditions, as
well as that modelled by KHALEEL [10] for superplastic deformation. The rate
of accumulation of each damage type is affected by temperature, strain rate,
and material (especially the presence of hard inclusions within the material),
but the two damage types react very differently to a change in deformation con-
ditions or material. In addition, many dynamic matrix-reorganisation processes
also affect damage development such as hardening by dislocation accumulation,
subsequent softening by recovery and recrystallisation processes, grain size reduc-
tion by recrystallisation, and normal grain growth. The main aim of this paper

is to produce a damage model for hot deformation that is capable of following the evolution and the macroscopic effect of the two damage types encountered during uniaxial experimental testing.

The work presented in this paper concentrates on the identification of inter-actions between the mechanisms of hot deformation and the accumulation of the two damage types described above. A phenomenological model for grain bound-ary and plasticity-induced damage is built and, by coupling this with a modified version of LIN and LIU'S model for microstructure evolution in hot deformation [12], a complete set of viscoplastic-damage constitutive equations is presented. The constants within the viscoplastic damage constitutive equations are deter-mined for a free-cutting steel over the temperature range of 1173–1373 K and deformation rates of 0.1–10 s^{-1}. The model is then used to predict the mate-rial flow stress evolution of a set of interrupted constant strain rate tests, and compared with experimental results.

2. Development of damage models

The response of the two damage mechanisms to factors such as temperature, strain rate and grain size are not similar, and thus an independent mechanism is assigned for each damage type. Damage accumulation is considered as being homogeneous, and is treated as a phenomenological continuum model for simple tension in the present work.

2.1. Damage equation set

The two damage mechanisms independently map the accumulation of each damage type. Material failure is determined by the total damage, defined as the sum of both damage types. Total damage is initially 0 representing the undamaged state, and rises to a value of 0.9 at which point damage coalesces and macrocracks develop, which is the criteria for material failure. The total damage D_T is in the form:

$$(2.1) \qquad D_T = D_{GB} + D_{Pi} \ (D_T < 0.9).$$

Damage is accumulated by the nucleation of new damage sites and the growth of pre-existing sites, thus the grain boundary damage, D_{GB}, and plasticity-induced damage, D_{Pi}, are represented as:

$$(2.2) \qquad \dot{D}_{GB} = \dot{D}_{GB}^N + \dot{D}_{GB}^G,$$

$$(2.3) \qquad \dot{D}_{Pi} = \dot{D}_{Pi}^N + \dot{D}_{Pi}^G$$

in which $\dot{D}_{GB}^N$ and $\dot{D}_{GB}^G$ are the rates of nucleation and growth of damage at grain boundaries, $\dot{D}_{Pi}^N$ and $\dot{D}_{Pi}^G$ are the rates of nucleation and growth of plasticity-induced damage.

The accumulation rate of grain boundary damage is highly dependent on the grain size. If grains are large, there is less grain boundary sliding and grain rotations under hot-deformation conditions and damage accumulation at grain boundaries is slow. If grain size is very small (<10 μm), superplasticity is achieved, grains can rotate and slide past each other with ease and damage accumulation is again slow. A grain size between these two extremes will cause the highest grain boundary damage accumulation rate. In addition, the band of critical grain size is dependent of deformation rate (Fig. 1). Fast deformation favours dislocation-based plastic deformation, meaning that the grain size to achieve grain boundary movement is relatively smaller, and superplasticity is not easily achieved. In contrast, slow deformation favours grain boundary sliding due to grain-boundary diffusion, and so the critical grain size becomes larger. To reflect this, the equation to describe grain boundary damage accumulation has been modified to reflect grain size, strain rate, as well as temperature-dependence and is given by:

$$(2.4) \qquad \dot{D}_{GB} = \eta \cdot \left(\dot{D}_{GB}^N + \dot{D}_{GB}^G \right)$$

in which the damage compliance variable, η, is defined as:

$$(2.5) \qquad \eta = a_1 \cdot \exp\left(-a_2 \cdot \left(1 - \frac{d}{d_c} \right)^2 \right),$$

$$(2.6) \qquad d_c = a_3 \cdot (\dot{\varepsilon}_p)^{-n_1},$$

where a_1, a_2, a_3 and n_1 are constants. The characteristic curves of the compliance variable η are given in Fig. 1 with variations of grain size for different deformation rates. For these calculations the values of constants are as given in Table 2. Equation (2.6) calculates the critical grain size for which grain boundary damage accumulation is at a maximum, which is a function of strain rate. Equation (2.5) reduces the accumulation rate when the actual grain size is not at the critical value. The highest grain boundary damage accumulation rate varies with grain size and strain rates [Fig. 1].

Nucleation of grain boundary damage is encouraged when grains are harder than the grain boundaries, leading to plastic deformation by grain boundary movement, thus the damage nucleation variable is strongly influenced by dislocation density (intra-grain hardness):

$$(2.7) \qquad \dot{D}_{GB}^N = a_4 \cdot (1 - D_{GB}) \cdot \dot{\rho}$$

in which a_4 is a material constant.
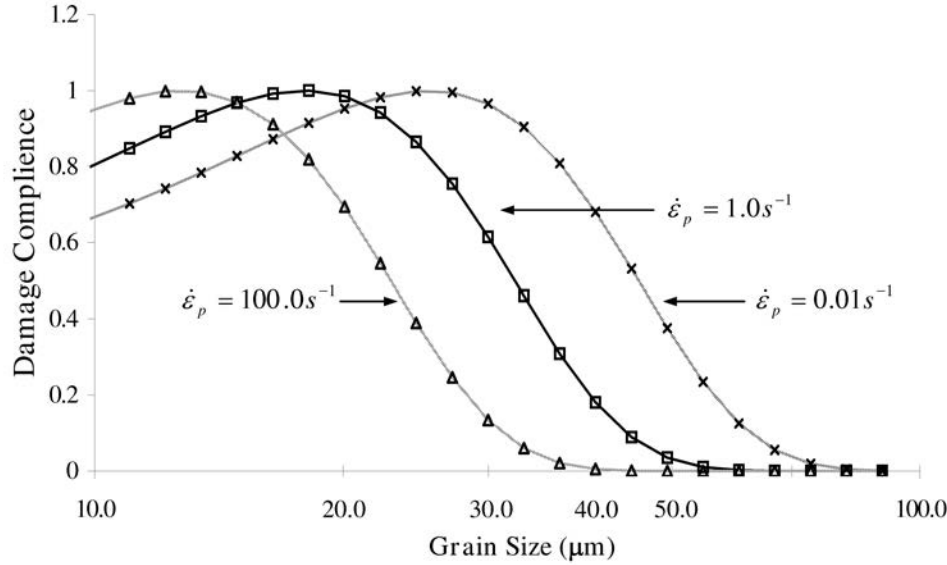
FIG. 1. Grain boundary damage compliance plotted against grain size for $T = 1273$ K.

Grain boundary damage grows so long as plastic deformation is taking place. COCKS and ASHBY [4] proposed an equation for the strain-controlled void growth of creep damage; modified for the present work, the equation takes the form:

$$(2.8) \qquad \dot{D}_{GB}^G = \left[\frac{1}{(1 - D_{GB})^{n_2}} - (1 - D_{GB})\right] \cdot \dot{\varepsilon}_p,$$

where n_2 is a constant. Plasticity-induced damage is created by the accumulation of dislocations around a hard inclusion. The nucleation of plasticity-induced damage is thus directly related to the amount of dislocation-based deformation experienced by the grain structure. A further consequence of this is that any softening processes acting to reduce the density of dislocations will also have a stabilising effect on nucleated voids. Using a similar term to that given in (1.1), but substituting creep strain rate for dislocation evolution rate, the rate of nucleation of plasticity-induced damage can be represented by:

$$(2.9) \qquad \dot{D}_{Pi}^N = (1 - D_{Pi}) \cdot \dot{\rho}.$$

The growth rate of plasticity-induced damage is a function of grain size, strain rate, and temperature, along with the amount of plasticity-induced damage that has been created. A large grain size favours deformation by dislocation movement and thus increases the rate of accumulation of plasticity-induced damage. For

the same reason, high strain rates increase the growth rate of plasticity-induced damage. The modelling equation is given as:

$$(2.10) \qquad \dot{D}_{Pi}^{G} = a_6 d \frac{D_{Pi}}{(1 - D_{Pi})^{n_3}} \cdot |\dot{\varepsilon}_p|^{n_4},$$

where a_6, n_3 and n_4 are constants.

2.2. Modelling the effect of damage on viscoplastic deformation

The basic model used for plastic strain is a hyperbolic sine law, with hardening and grain size effects considered [12], of the form:

$$(2.11) \qquad \dot{\varepsilon}_p = \frac{A_1 \cdot \sinh\left[A_2 \cdot (\sigma - R - k)\right]}{d^{\gamma_1}},$$

where A_1, A_2, and γ_1 are material constants. k is the initial yield stress of the material and R is the isotropic hardening due to plastic deformation. γ_1 characterises the effect of grain size on the viscoplastic flow of the material.

Damage at grain boundaries reduces the load bearing section over which a deformation force acts. This increases the effective stress according to the common practice of dealing with creep damage. Plasticity-induced damage is considered in much the same way; voids growing within grains will distribute and focus flow stress away from the voids [7]. The localisation of stress into the lattice generates more force to overcome grain hardening, when viewed from outside the grain, this leads to a softer grain that is easier to deform. In other words, plasticity-induced damage shrinks the yield surface of the material. Thus considering the softening effects due to damage, Eq. (2.11) is written as:

$$(2.12) \qquad \dot{\varepsilon}_p = A_1 \cdot \sinh\left[A_2 \cdot \left(\frac{\sigma}{(1 - D_{GB})} - (R + k) \cdot (1 - D_{Pi})\right)\right] d^{-\gamma_1}$$

in which grain boundary damage increases the effective stress causing plastic deformation, and plasticity-induced damage decreases the effective material hardness.

3. Development of unified viscoplastic-damage constitutive equations

Unified constitutive equations for viscoplasticity have been developed for many metal materials [13, 14]. The equations enable a wide range of time-dependent phenomena to be modelled, such as strain hardening, stress relaxation and ratchetting [15], and in addition enable the important time-dependent

effects, such as strain rates, recovery and creep to be modelled. This work intends to develop a set of unified viscoplastic damage constitutive equations to model the evolution of recrystallisation, dislocation density, hardening and grain size, damage at grain boundaries and around the second phase particles, to rationalise their inter-relationships and effects on viscoplastic flow of materials. The mechanism-based unified viscoplastic damage constitutive equations for hot metal forming may take the form:

$$(3.1) \qquad \dot{\varepsilon}_p = A_1 \cdot \sinh\left[A_2 \cdot \left(\frac{\sigma}{1 - D_{GB}} - (R + k) \cdot (1 - D_{Pi})\right)\right] \left(\frac{d}{d_0}\right)^{-\gamma_1},$$

$$(3.2) \qquad \dot{S} = H_1 \cdot (x \cdot \bar{\rho} - \bar{\rho}_c \cdot (1 - S)) \cdot (1 - S)^{\lambda_1},$$

$$(3.3) \qquad \dot{x} = X_1 \cdot (1 - x) \cdot \bar{\rho},$$

$$(3.4) \qquad \dot{\bar{\rho}} = \left(\frac{d}{d_0}\right)^{\delta_1} \cdot (1 - \bar{\rho}) \cdot |\dot{\varepsilon}_p|^{\delta_2} - C_r \cdot \bar{\rho}^{\delta_3} - \frac{C_S \cdot \bar{\rho}}{1 - S} \dot{S},$$

$$(3.5) \qquad \dot{R} = 0.5 \cdot B \cdot \bar{\rho}^{-1/2} \cdot \dot{\bar{\rho}},$$

$$(3.6) \qquad \dot{d} = \left(\frac{G_1}{d}\right)^{\psi_1} - G_2 \cdot \dot{S} \cdot \left(\frac{d}{d_0}\right)^{\psi_2},$$

$$(3.7) \qquad \sigma = E \cdot (\varepsilon_T - \varepsilon_p),$$

$$(3.8) \quad \dot{D}_{GB} = \eta \cdot \left([a_4 \cdot (1 - D_{GB}) \cdot \dot{\bar{\rho}}] + \left[\left(\frac{1}{(1 - D_{GB})^{n_2}} - (1 - D_{GB})\right) \cdot |\dot{\varepsilon}_p|\right]\right),$$

$$(3.9) \quad \dot{D}_{Pi} = a_5 \cdot \left([(1 - D_{Pi}) \cdot \dot{\bar{\rho}}] + \left[a_6 \cdot \frac{D_{Pi} \cdot d}{(1 - D_{Pi})^{n_3}} \cdot |\dot{\varepsilon}_p|^{n_4}\right]\right),$$

$$(3.10) \quad \dot{D}_T = \dot{D}_{GB} + \dot{D}_{Pi}.$$

Grain boundary damage parameter η has been defined in Eq. (2.5). Temperature-dependent material parameters in the Eqs. (3.1)–(3.10) are defined in Table 1.

Viscoplastic flow of the material is modelled using Eq. (3.1), which is a function of flow stress, σ, grain boundary damage, D_{GB}, plasticity-induced damage, D_{Pi}, isotropic hardening, R, and the average grain size, d. Equation (3.2) models the volume fraction of recrystallised grains during and after hot deformation. The incubation time for recrystallisation is controlled by Eq. (3.3), which is directly related to the accumulation of normalised dislocation density. The volume

Table 1. Temperature-dependent parameters.

$k = k_{(0)} \cdot \exp\left(\dfrac{Q_p}{\kappa \cdot T}\right)$	$\bar{\rho}_c = \bar{\rho}_{c(0)} \cdot \exp\left(\dfrac{Q_p}{\kappa \cdot T}\right)$
$C_r = C_{r(0)} \cdot \exp\left(\dfrac{-Q_{ac}}{\kappa \cdot T}\right)$	$X_1 = X_{1(0)} \cdot \exp\left(\dfrac{-Q_{ac}}{\kappa \cdot T}\right)$
$G_1 = G_{1(0)} \cdot \exp\left(\dfrac{-Q_{GG}}{\kappa \cdot T}\right)$	$E = \dfrac{E_{(\mathrm{ref})}}{\cosh^2\left(K_1 \cdot \left(T - T_{(\mathrm{ref})}\right)\right)}$
$\alpha_1 = \alpha_{1(0)} \cdot \exp\left(\dfrac{Q_{GB}}{\kappa \cdot T}\right)$	$\alpha_5 = \alpha_{5(0)} \cdot \exp\left(\dfrac{Q_{Pi}}{\kappa \cdot T}\right)$

fraction of recrystallisation variable, S, varies from 0 (no recrystallised grains) to 1.0 (representing the fully recrystallised state).

The normalised dislocation density is defined by $\bar{\rho} = (\rho - \rho_i)/\rho$, where ρ is the current dislocation density and ρ_i is the dislocation density for the virgin material. When the plastic deformation is high, $\rho \gg \rho_i$. Thus the range of normalised dislocation density varies from 0 to 1.0. Equation (3.4) models the evolution of the normalised dislocation density. The first term in the equation models the accumulation of dislocations due to viscoplastic deformation $|\dot{\varepsilon}_p|$ and the dynamic recovery of the dislocation density. The second term in the equation represents the annealing process, which reduces the dislocation density. Recrystallisation creates dislocation free grains, which results in the reduction of average dislocation density. The evolution of the normalised dislocation density due to recrystallisation is described by the third term of Eq. (3.4). The hardening of the material due to plastic deformation is directly related to the dislocation density and its evolution is given by Eq. (3.5). The effects of grain size on the accumulation of dislocation density is controlled by $(d/d_0)^{\delta_1}$. Small grain size facilitates the grain boundary sliding and grain rotation under viscoplastic deformation. Thus less strain is 'carried by dislocations'. The average grain size evolution is described by Eq. (3.6). The first term of the equation represents the static grain growth and the second the grain refinement due to recrystallisation. Flow stress is calculated from the elastic strain in the usual way; Eq. (3.7) along with details of the above viscoplastic constitutive equations are given by LIN *et al.* [12].

The grain boundary damage evolution is represented by Eq. (3.8). The effects of grain size and strain rates on grain boundary damage evolution are controlled by the parameter η (Eqs. (2.5) and (2.6)). Nucleation and growth rates of plasticity-induced damage are described by Eq. (3.9), which is directly related to Eqs. (2.3), (2.9) and (2.10). The total damage evolution is given by Eq. (3.10). The material constants, as indicated by the nomenclature and given

in Table 2, are determined from experimental data using an Evolutionary Programming (EP)-based optimisation technique developed by LI *et al.* [16] using the objective function detailed by LIN *et al.* [17]. The details of the optimisation process and the numerical procedure for this type of the problems are described by LIN *et al.* [12] and LI *et al.* [16].

Table 2. Material constants for the free-cutting steel.

Constant		Determined Value	Constant		Determined Value
A_1	$\left(\mathrm{s}^{-1}\right)$	68.0	κ	$\left(J \cdot \mathrm{mol}^{-1} \cdot \mathrm{K}^{-1}\right)$	8.31
A_2	$\left(\mathrm{MPa}^{-1}\right)$	1.5e-2	Q_p	$\left(J \cdot \mathrm{mol}^{-1}\right)$	1.069e5
γ_1	$(-)$	1.0	Q_{ac}	$\left(J \cdot \mathrm{mol}^{-1}\right)$	4.082e5
$k_{(0)}$	(MPa)	6.81e-4	$E_{(\mathrm{ref})}$	(MPa)	1.27e5
H_1	$\left(\mathrm{s}^{-1}\right)$	14.5	K_1	$\left(\mathrm{K}^{-1}\right)$	2.0e-3
$\bar{\rho}_{c(0)}$	$(-)$	1.10e-7	$T_{(\mathrm{ref})}$	(K)	1073
λ_1	$(-)$	1.0	$\alpha_{1(0)}$	$(-)$	1.3e-4
d_0	(μm)	28.67	α_2	$(-)$	1.1
δ_1	$(-)$	1.02	α_3	(μm)	18.0
δ_2	$(-)$	1.5	n_1	$(-)$	7.5e-2
$C_{r(0)}$	$\left(\mathrm{s}^{-1}\right)$	1.13e17	α_4	$(-)$	3.8e-5
δ_3	$(-)$	2.13	n_2	$(-)$	4.66
C_S	$(-)$	1.0	$\alpha_{5(0)}$	$(-)$	2.04e-3
$X_{1(0)}$	$\left(\mathrm{s}^{-1}\right)$	1.44e17	α_6	$\left(\mathrm{μm}^{-1}\right)$	2.33
B	(MPa)	1.60e2	n_3	$(-)$	14.0
$G_{1(0)}$	(μm)	6.401e4	n_4	$(-)$	0.89
ψ_1	$(-)$	0.875	Q_{GG}	$\left(J \cdot \mathrm{mol}^{-1}\right)$	7.020e4
G_2	$\left(\mathrm{s}^{-1}\right)$	26.61	Q_{GB}	$\left(J \cdot \mathrm{mol}^{-1}\right)$	1.017e5
ψ_2	$(-)$	0.90	Q_{Pi}	$\left(J \cdot \mathrm{mol}^{-1}\right)$	2.5e4

4. MODELLING RESULTS AND EXPERIMENTAL VALIDATION

4.1. Experimental results for the determination of material parameters

Hot uniaxial tensile tests were performed to obtain the stress-strain relationships for a range of constant strain rates and temperatures, which are used in the determination of material constants within the equations. The experimental programme was conducted on a Gleeble material simulator using a free-cutting steel which contained hard manganese sulphide inclusions, evenly distributed through the grain structure in the tested temperature range. The experimental programme was identical to that described in detail in the companion paper for a free-cutting steel. A 5-minute soaking process performed at 1473 K was

used to create a uniform microstructure, after which constant strain rate tests were conducted at strain rates between 0.1–10 s^{-1} at a temperature of 1273 K, and at a strain rate of 1.0 s^{-1} at temperatures between 1173 and 1373 K. The determined material constants are listed in Table 2.

Figure 2 shows experimental data plotted alongside the stress-strain curves generated by the fitted equation set for a range of strain rates and temperatures. The fitted model is consistent with test results, displaying good accuracy in the prediction of flow stresses as well as strains at failure for all conditions given, with strains at failure showing less than 5% discrepancy in all conditions. The peak in flow stress followed by an extended ductility that is associated with dynamic recrystallisation is prominent in low strain rate and high temperature stress-
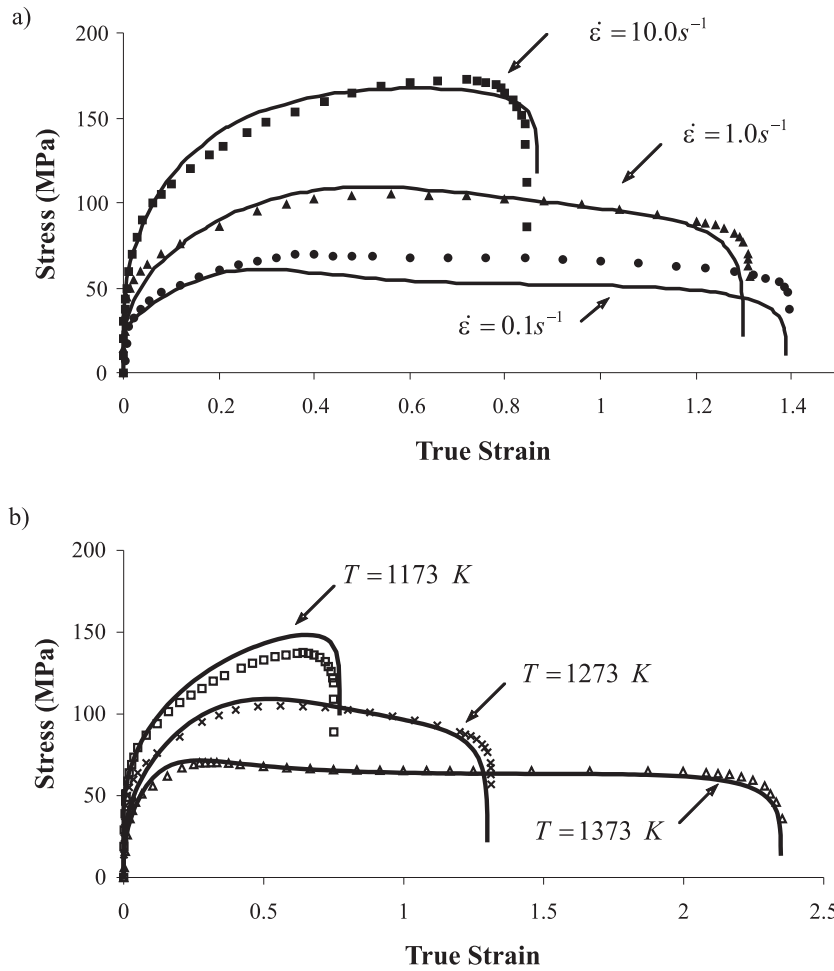
FIG. 2. Comparison of experimental (symbols) and computed (curves) stress-strain relationships for (a) different strain rates at 1273 K and (b) different temperatures at $\dot{\varepsilon} = 1.0$ s^{-1}.

strain plots, becoming less prominent with increasing strain rate and decreasing temperature.

It is understood that for high temperature, small grain size and low strain-rate deformation conditions, the dominant deformation mechanism is through grain boundary sliding and grain rotation. This results in inter-granular failure due to the accumulation of grain boundary damage. If the deformation rate is high, the grain size large and temperature is low, the strain is mainly carried by dislocations and voids at inclusions can be observed. This is due to the ac-
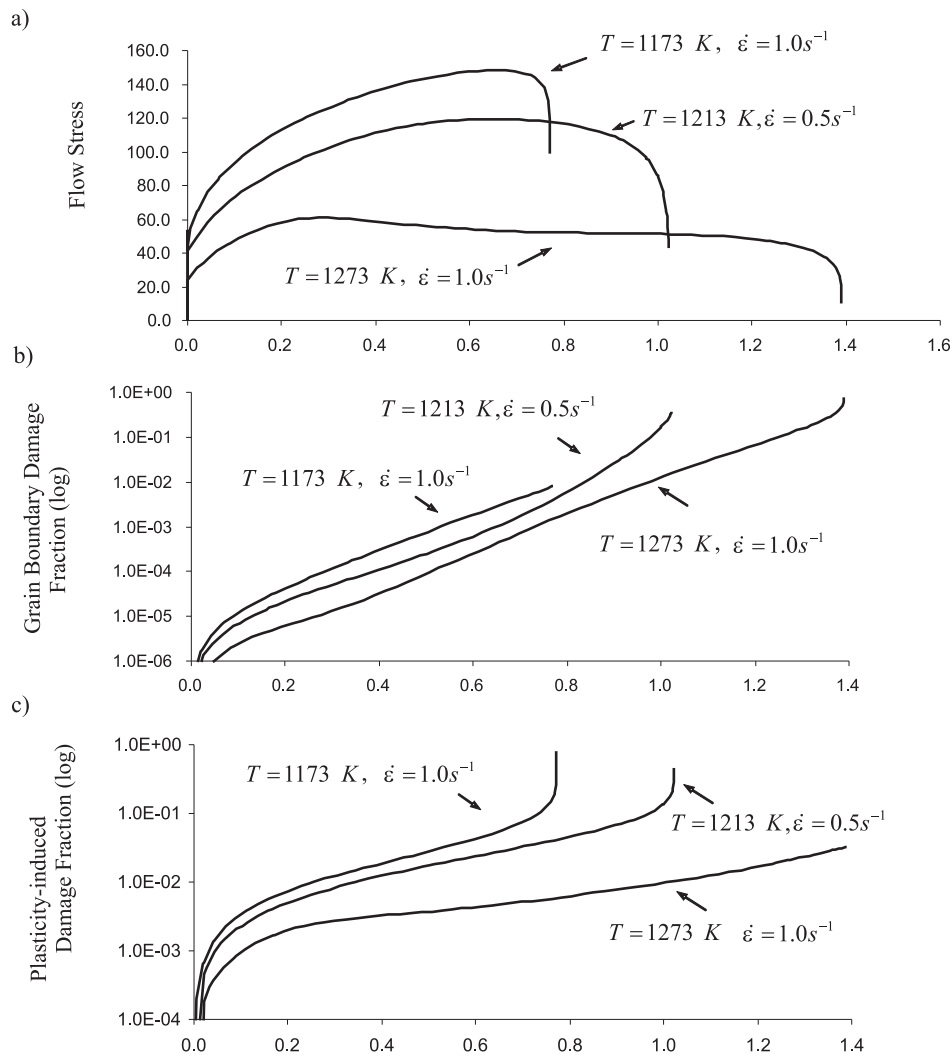
FIG. 3. Change of dominant damage type with increasing strain rate: a) flow stress plot for 3 deformation conditions, b) grain boundary damage, c) plasticity-induced damage.

cumulation of plasticity-induced damage. Calculations were carried out using the determined viscoplastic damage constitutive equations with the same initial grain size, different temperature and strain rates. Figure 3 shows the predicted results for flow stress (a), grain boundary damage (b), and plasticity-induced damage (c), for three loading conditions. are: (i) Low temperature and high strain rate: $T = 1173$ K and $\dot{\varepsilon}_T = 1.0$ s^{-1}; (ii) Medium temperature and strain rate: $T = 1213$ K and $\dot{\varepsilon}_T = 0.5$ s^{-1}; and, (iii) High temperature and low strain rate: $T = 1273$ K and $\dot{\varepsilon}_T = 0.1$ s^{-1}. When the total damage reaches 0.9, the failure takes place. Figure 3 shows that, for the first case, plasticity-induced damage is dominant over grain boundary damage. As the deformation temperature increases and strain rate decreases, the balance damage state can be observed. However, when the temperature increases further, grain boundary sliding deformation mechanism plays more important role. This results in a high value of grain boundary damage.

4.2. Experimental and modelled results of interrupted deformation tests

A second test set was conducted using an interrupted deformation programme. The testpieces were soaked for 5 minutes at 1473 K and then deformed at a total strain rate of 10 s^{-1} and a temperature of 1273 K. On reaching a pre-specified strain, the test was interrupted. Deformation was halted and testpiece temperature was maintained. During the interrupt period, metadynamic recovery processes develop, simulating the microstructure development between successive passes of a multi-pass hot-rolling schedule. Interruptions lasting 0.3–10 s were imposed once a true strain of 0.3 had been reached, corresponding with a point in deformation at which recrystallisation nucleations are present, but dynamic recrystallisation (DRX) is not apparent. Once the desired interrupt time is reached, the testpiece deformation was continued to failure.

The test programme was modelled using the developed equation set by emulating the physical restrictions given in the tests. The model was started with conditions of $\dot{\varepsilon}_T = 10$ s^{-1} and $T = 1273$ K. On reaching a strain $\varepsilon_T = 0.3$, the conditions of the model were forced to $\dot{\varepsilon}_p$, $\dot{\varepsilon}_T = 0$ s^{-1}. All other mechanisms and conditions were left unrestrained, resulting in the metadynamic reorganisation processes such as recovery and recrystallisation continuing to evolve, emulating the material evolution in the test programme. After the predefined interrupt time had passed, the model conditions were returned to $\dot{\varepsilon}_T = 10$ s^{-1} and deformation continued as before, until the termination condition of damage coalescence was reached.

The simulation of interrupted constant strain rate tests shows promising results. Stress-strain plots correctly predict the general shape of the curves (Fig. 4). The general trend exhibited by the strain at failure following reload-
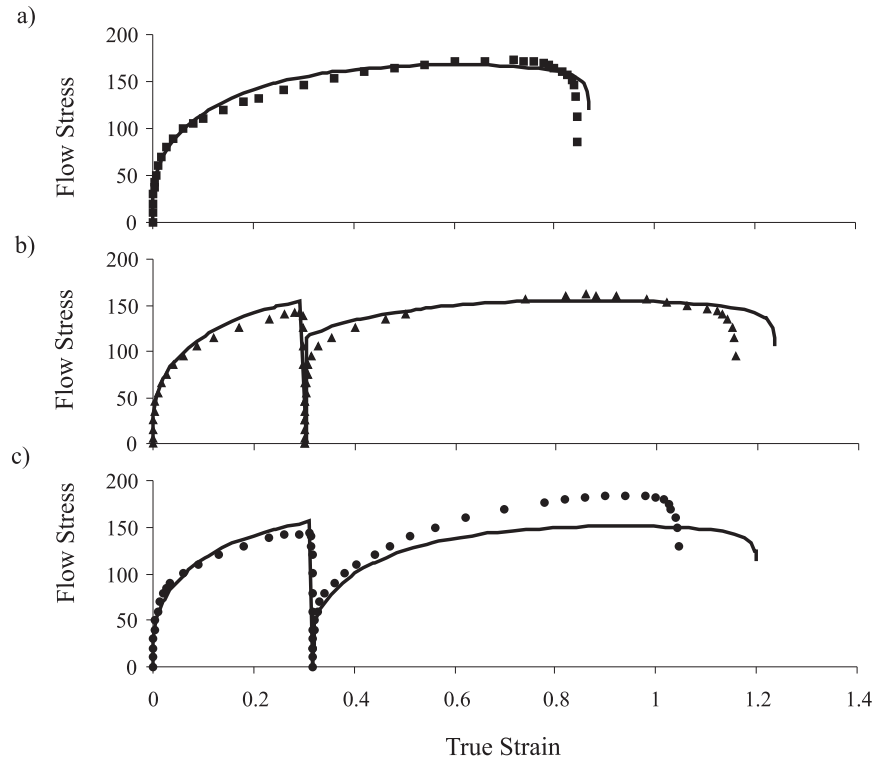
FIG. 4. Comparison of experimental (symbol) and computed (curves) interrupted flow stress curves at $\dot{\varepsilon} = 10 \text{ s}^{-1}$ and $T = 1273$ K for interrupt periods of (a) 0.0 s, (b) 0.3 s, and (c) 5.0 s.
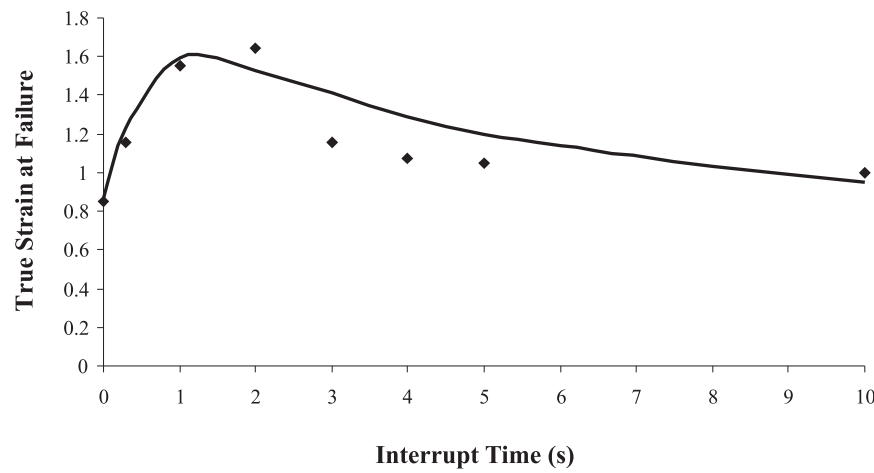
FIG. 5. Comparison of experimental (symbols) and computed (curve) strain at failure against interrupt period for $\dot{\varepsilon} = 10 \text{ s}^{-1}$ and $T = 1273$ K.

ing is correctly predicted (Fig. 5), with the predicted interrupt time leading to maximum ductility falling only marginally short of the experimentally determined value. The complex relationship between the interrupt period and the resulting reloading curve is interpreted within the model as the result of grain size and dislocation density changes resulting from metadynamic recovery, recrystallisation (MDRX), and grain size changes. A detailed explanation of the test results can be formed by splitting the material evolution into a number of stages.

Stage 1: Strain is applied at a constant strain rate. As the testpiece is strained, recrystallisation nucleation sites may develop within the material. No significant amount of DRX occurs. At a constant strain rate of $10\,\mathrm{s}^{-1}$, this stage will last approximately 0.03 s, during which no notable grain growth occurs.

Stage 2: Interrupt strain is reached. Deformation is stopped. Recrystallisation may continue depending on the remaining dislocation density, which reduces due to recrystallisation and annealing effects. Grain refinement takes place due to recrystallisation. Nucleated MDRX grains grow within the lattice until the new grain recrystallisation fronts meet. During this period, a limited amount of damage recovery takes place due to the reduction of dislocation density. Normal grain growth occurs depending on the interrupted intervals. Complex microstructure evolution takes place during inter-passes.

Stage 3: Constant strain rate deformation is restarted. Material evolution this point depending on what stage was reached before deformation was continued.

The interrupted tests were used to give an indirect measurement of the material's RX characteristics. By interpreting the interrupted flow stress results it has been possible to identify the relationship between the completeness of RX and material flow response. This relationship is critical if the model is to remain accurate in complex RX conditions; the model's accuracy can be improved by collecting additional experimental data to directly fit the data for static RX or grain size evolution.

In the companion paper, it has been discussed that recrystallisation processes may annihilate or reduce damage nucleations and young (physically small) damage sites. The damage level within the proposed model is reduced by the dislocation-linked reduction in damage nucleation sites; both of plasticity-induced and grain boundary damage.

The current model is not capable of accurately predicting the peak flow stress following reloading, which is predicted as varying only slightly with interrupt time, suggesting that further development of grain size and hardening mechanisms are required to improve the accuracy. The comparison of experimental and peak flow stress for the reloading state can be observed in Fig. 4. The trend

of the strain at failure for the reloading stage can be also predicted using the equation set, although the highest error is about 15% between the experimental and predicted results, which are shown in Fig. 5.

5. Conclusions

A set of unified viscoplastic damage constitutive equations has been formulated and determined to model the damage evolution features observed in experiments for a free-cutting steel under hot working conditions. In addition to recrystallisation, grain size evolution and dislocation hardening, the effects of microstructure, strain rates and temperature on the grain boundary damage and plasticity-induced damage can be predicted. The developed constitutive equation set can also be used to model the viscoplastic flow, microstructure evolution and failure of the material under interrupted loading conditions, including the microstructural evolution during the interval of the loadings. The errors of the prediction are within 20% for peak flow stress and 15% for strains at failure.

Acknowledgments

References

1. A.L. Gurson, *Continuum theory of ductile rupture by void nucleation and growth: Part 1 – Yield Criteria and Flow Rules for Porous Ductile Media,* J. Engng. Matr. Tech., **99**, 1977.

2. L.M. Kachanov, *Time to the rupture process under creep conditions,* Izv. Akad. SSR. Oid. Tekh. Nauk., **8**, 26–31, 1958.

3. J. Lin, D.R. Hayhurst, and B.F. Dyson, *The standard ridges uniaxial creep testpiece: computed accuracy of creep strain,* J. of Strain Analysis, **28**, 2, 101–115, 1993.

4. B.F. Dyson, *Creep and fracture of metals: mechanisms and mechanics*, Revue Phys. Appl., **23**, 605–613, 1988.

5. A.C.F. Cocks and M.F. Ashby, *On creep fracture by void growth,* Progress in Material Science, **27**, 189–244, 1982.

6. J.R. Rice and D.M. Tracey, *On the ductile enlargement of voids in triaxial stress fields,* J. of the Mechanics and Physics of Solids, **17**, 201–217, 1969.

7. N. Bonora, *Identification and measurement of ductile damage parameters,* J. of Strain Analysis, **34**, 463–478 1999.

8. S. Dhar, *et al.*, *A continuum damage mechanics model for ductile fracture*, International Journal of Pressure Vessels and Piping, **77**, 335–344, 2000.

9. J.S. Vetrano, *et al., Evidence for excess vacancies at sliding grain boundaries during superplastic deformation*, Acta Materialia, **47**, 4125–4129, 1999.

10. M.A. Khaleel, *et al., Constitutive modeling of deformation and damage in superplastic materials*, International J. of Plasticity, **17**, 277–296, 2001.

11. D.R. Hayhurst, *Creep rupture under multi-axial states of stress*, J. Mech. Phys. Solids, **20**, 381–390, 1972.

12. J. Lin and Y. Liu, *A set of unified constitutive equations for modelling microstructure evolution in hot deformation*, J. of Materials Processing Technology, **143–144**, 281–285, 2003.

13. L.G. Lim and F.P.E. Dunne, *Modelling central bursting in the extrusion of particulate reinforced metal matrix composite materials*, Int. J. of Machine Tools and Manufacture, **37**, 901–915, 1997.

14. A.A. Howe, D.C.J. Farrugia, *Alloy design: from composition to through process models*, Materials Science and Technology, **15**, 15–21, 1999.

15. J. Lin, F.P.E. Dunne and D.R. Hayhurst, *Physically-based temperature dependence of elastic viscoplastic constitutive equations for copper between 20 and 500 °C*, Philosophical Magazine, *A*, **74**, 2, 655–676, 1996.

16. B. Li, J. Lin, and X. Yao, *A novel evolutionary algorithm for determining unified creep damage constitutive equations*, Int. J. of Mech. Sci., **44**, 5, 987–1002, 2002.

17. J. Lin, B.H. Cheong, and X. Yao, *Universal multi-objective function for optimising superplastic-damage constitutive equations*, J. of Mat. Proc. Tech., **125–126**, 199–205, 2002.

NUMERICAL MODELING OF DELAMINATION IN GFRP COMPOSITES[1)]

M. R. K o s h r a v a n,   A. Y o u r d k h a n i

Faculty of Engineering
Mechanical Engineering Department
University of Tabriz, Tabriz, Iran

Polymer matrix composites have become highly relevant structural materials. However, high performance laminates are quite susceptible to transverse cracking and delamination. Transverse cracks may cause significant stiffness losses, accelerate environmentally induced degradation and generate delamination. The characterization and modeling of fracture behavior is thus highly relevant for the design of composite parts. In this paper, the delamination phenomena in the Mixed Mode I+II which is one of the important cause of failure in multilayer composites, are studied. The composite is a GFRP (Glass Fiber Reinforced Plastic) and are studied under static monotonic loading. Using the Irwin–Kies criteria, usual laws of elasticity and VCCT (Virtual Crack Closure Technique), based on finite element method, the SERR (Strain Energy Release Rate) in Mode I, Mode II, and four ratio Modes (G_I/G_{II}) are evaluated. The finite element analysis of test bars is carried out using ANSYS5.5 software in two dimensions, and the appropriate boundary conditions are chosen. Our numerical results are compared with known experimental ones and with application of the local effects, such as three-dimensional (3D) effect in the width of the test bar with the shape of MMB (Mixed Mode Bending) specimen, scattering between experimental and numerical results is evaluated and discussed. For the 3D effect, the variation of the stress components in the mid-plane of specimen in which delamination occurs, versus the width of specimen, is obtained. Then the variation of strain energy release rate in different ratio Modes, in the width of test bars is calculated.

1. Introduction

Composite laminates are one of the most useful materials for the engineering structures, because of their high strength ratio to their weight. A glass-fiber epoxy resin composite is one of those composites that its application, because of its high resistance in tension, the low commercial price of its fibers compared to others, such as carbon fibers, and its resistance against corrosion, has increased [1]. When a multilayer composite is loaded, the interlaminar stresses appear in the interface of the layers. Theses stresses lead to delamination [2], which is one of the most important mechanisms of rupture of the composite materials (Fig. 1) [3].

[1)]GFRP – Glass Fiber Reinforced Plastic.

Hence prediction of delamination and also fracture toughness of these materials is useful to their amelioration. In the present research the Uni-Directional (UD) GFRP were modeled. The modeling of a multilayer composite with different orientation of fibers in each layer will be done in the future researches. In this case, the evaluation of interlaminar stresses before modeling of delamination is important [4].
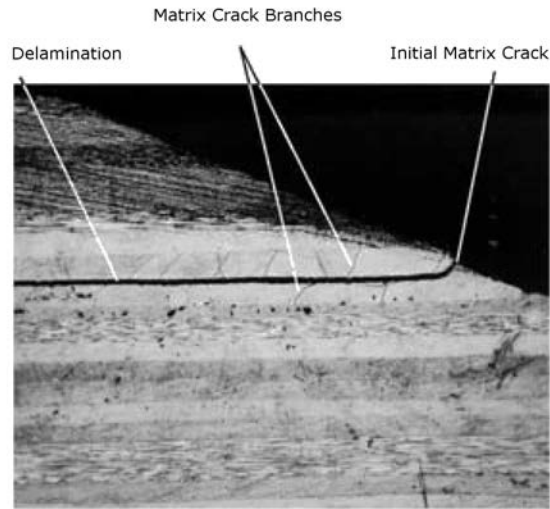
Fig. 1. Delamination in a composite material.

In the mechanism of delamination which is analogous to the crack growth in isotropic materials, all the possibilities of rupture shown in Fig. 2 exist [5]. Testing of Mode I is standardized by ISO using DCB (Double Cantilever Beam) specimen and several researches carried on Mode II using ENF (End Notched Flexure) [6] and ELS (End Loaded Split) specimen are well advanced. In reality delamination doesn't occur in a pure mode. Hence investigation on the Mixed Mode seems to be important [7].
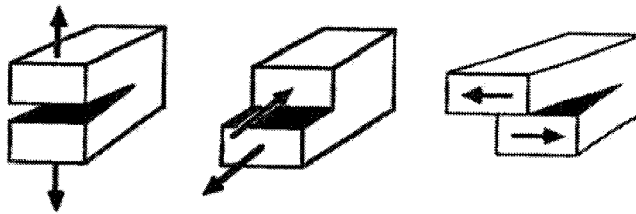
Fig. 2. Modes of rupture.

2. MMB SPECIMEN

Different tests of delamination on the Mixed Mode I + II such as CTS (Compact Tension Specimen) and CLS (Crack Lap Shear) are presented [8]. The most useful specimen for the Mixed Mode is the MMB specimen. Crews and Reeder, with the composition of DCB and ENF specimens, have presented a MMB specimen [9]. The first concept of MMB test device, in order to decrease the linear geometrical errors, which reached about 30%, was redesigned in order to eliminate the moment of the loads around the pins through which it is applied to the specimen [10]. In the corrected concept, the nonlinear errors are decreased to less than 3% and finally the test device is designed as shown in Fig. 3 [11].
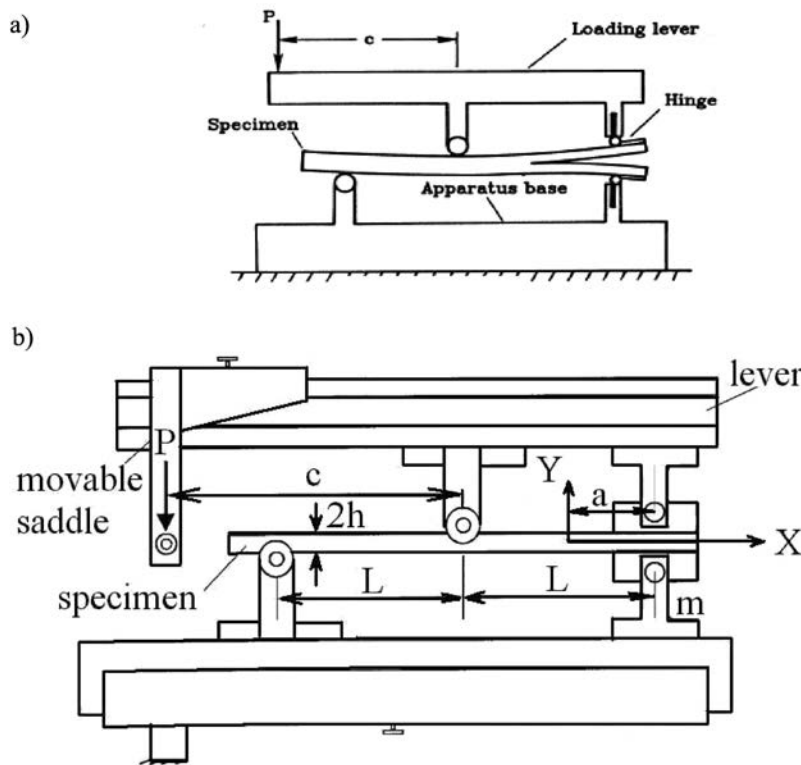
FIG. 3. MMB test apparatus [10]: a) schematic form; b) test apparatus with the device.

The manner of Mode I and Mode II loading composition and their application to the specimen are shown in Fig. 4 [9]. We can apply the forces using the unique load P through a lever, having I shape. If this load reaches its critical value, delamination will occur. The length of the lever c determines the ratio of the loads and then the ratio of the Modes. When the load P is applied in

the middle of the span of the beam, $(c = 0)$, the test bar will be loaded in the pure Mode II, and with increasing c, the ratio G_II/G_T (G_T is the total SERR) decreases. By moving the lever and lifting it on the hinge, the pure Mode I loading occurs. Dimensions and mechanical properties of the uni-directional glass fiber epoxy resin composite, which is used in our numerical analysis, are given in the Table 1 [11].
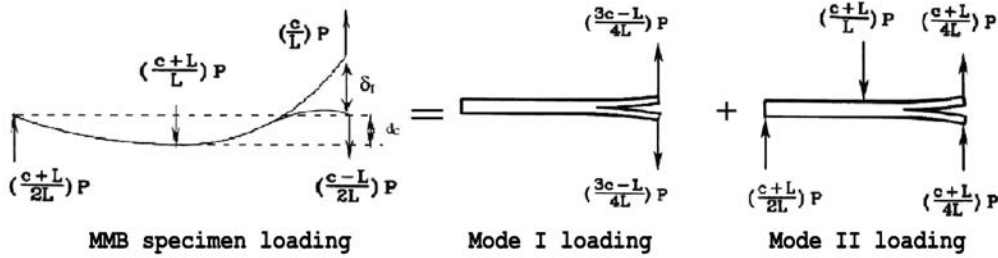
FIG. 4. MMB specimen loading.

Table 1. Mechanical properties and geometry of the test bar.

Specimen Dimension	Mechanical Property	
$L = 65$ mm	$E_{11} = 25.7$ GPa	$(\pm 8\%)$
$2h = 5$ mm	$E_{22} = 6.5$ GPa	$(\pm 8\%)$
$b = 20$ mm	$G_{12} = 2.5$ GPa	$(\pm 8\%)$
$L_T = 150$ mm	$\upsilon_{12} = 0.32$	$(\pm 8\%)$
$a_0 = 35$ mm	$\nu_\text{fiber} = 35.4\%$	$(\pm 8\%)$
	$\nu_\text{void} = 4.2\%$	$(\pm 8\%)$

3. THEORY OF STRAIN ENERGY RELEASE RATE

In this theory, the Irwin–Kies relationship is given as follows [12]:

$$(3.1) \qquad G = \frac{P^2}{2b}\frac{\partial C}{\partial a},$$

$$(3.2) \qquad C = \delta/P.$$

In this relationship P is the applied load, b is the width of specimen, C is the compliance, a is the crack length and δ is the deflection in the point of the load application. When G reaches its critical value (G_{IC}), delamination initiates.

4. BEAM THEORY

Using the elementary theory of beams and their substitution in the relations of Irwin–Kies, we can obtain the relations for the strain energy release rate. According to Fig. 4, the Mode I and Mode II components of loading are given as follow [10]:

(4.1)
$$P_{\text{I}} = \left(\frac{3c - L}{4L} \right) P,$$

$$P_{\text{II}} = \left(\frac{c + L}{L} \right) P.$$

Using the elementary beam theory for the DCB and the ENF specimens, the Mode I and Mode II components of the SERR are obtained [10]:

(4.2)
$$G_{\text{I}} = \frac{12a^2 P_{\text{I}}^2}{b^2 h^3 E_{11}},$$

$$G_{\text{II}} = \frac{9a^2 P_{\text{II}}^2}{16 b^2 h^3 E_{11}}.$$

With substitution of relations (4.1) with the Eqs. (4.2), we will have:

(4.3)
$$G_{\text{I}} = \frac{3a^2 P^2}{4 b^2 h^3 L^2 E_{11}} (3c - L)^2,$$

$$G_{\text{II}} = \frac{9a^2 P^2}{16 b^2 h^3 L^2 E_{11}} (c + L)^2.$$

So the ratio of modes is defined as follows:

(4.4)
$$\frac{G_{\text{I}}}{G_{\text{II}}} = \frac{4}{3} \left[\frac{3c - L}{c + L} \right], \qquad c \geq \left(\frac{L}{3} \right).$$

So relation (4.4) will not be valid for the values of C less than 21.67 mm. The ratio of modes is independent of the crack length a, and depends only on the length c. Using the correction coefficients for the shape deformation corresponding to the rotation of the section of specimen at the end of the crack and also the shape of shear deformation, relation (4.3) is corrected as follows [13]:

(4.5)
$$G_{\text{I}} = \frac{3a^2 P^2}{4 b^2 h^3 L^2 E_{11}} (3c - L)^2 \left[1 + \frac{2}{a\lambda} + \frac{1}{a^2 \lambda^2} + \frac{h^2}{10 a^2} \frac{E_{11}}{G_{13}} \right],$$

$$G_{\text{II}} = \frac{9a^2 P^2}{16 b^2 h^3 L^2 E_{11}} (c + L)^2 \left[1 + \frac{h^2}{5 a^2} \frac{E_{11}}{G_{13}} \right], \qquad \lambda = \frac{1}{h} \sqrt[4]{\frac{6 E_{22}}{E_{11}}}.$$

5. Calibration method

In this method, the compliance of specimen is calculated by measuring the critical applied load (which leads to the crack growth), the crack length and the displacement of the point of load application. This experiment is carried out for test bars with different initial crack lengths and results are demonstrated by the curve of compliance versus, the crack length. If we consider two separate compliances for Mode I and Mode II components, we will have [7]:

$$C_{\mathrm{I}} = \frac{\delta_I}{P_{\mathrm{I}}} = Ka^n,$$

(5.1)

$$C_{\mathrm{II}} = \frac{\delta_{\mathrm{II}}}{P_{\mathrm{II}}} = C_0 + ma^3.$$

In these relations P_{I} and P_{II} are determined with relation (4.2). n and m are obtained respectively from slope of the curves $Ln(C_{\mathrm{I}}) - Ln(a)$ and $C_{\mathrm{II}} - a^{1/3}$. δ_{I} is obtained directly by measurement of the opening of the crack. Displacement d_c is measured in the support, as shown in Fig. 4 and δ_{II} is calculated as follows [7]:

$$\delta_{\mathrm{II}} = \Delta + d_c m,$$

(5.2)

$$\Delta \approx \delta_{\mathrm{I}}/4.$$

Thus, Mode I and Mode II components of SERR are evaluated using the following relations [7]:

$$G_{\mathrm{I}} = \frac{nP_{\mathrm{I}}\delta_{\mathrm{I}}}{2ab},$$

(5.3)

$$G_{\mathrm{II}} = \frac{3ma^2 P_{\mathrm{II}}^2}{2b}.$$

In another method for obtaining SERR in Mode I, C is considered as a function of $(a + |\Delta|)^3$ and Δ is determined using the curve $C_{\mathrm{I}}^{1/3} - a$. As a result, the following relation is obtained. Δ indicates the phenomena of shear and rotation at the end of the crack [14].

(5.4)
$$G_{\mathrm{I}} = \frac{3P_I \delta_I}{2b(a + |\Delta|)}.$$

6. Finite element method

In this section, VCCT method is used and the components of strain energy release rate are obtained using the following relations:

(6.1)
$$G_{\mathrm{I}} = \lim_{\Delta a \to 0} \frac{1}{2b\Delta a} p_y^0 (\nu_1 - \nu_2),$$

$$G_{\mathrm{II}} = \lim_{\Delta a \to 0} \frac{1}{2b\Delta a} P_x^0 (u_1 - u_2),$$

u and v are the relative displacement between nodes 1 and 2. Δa is the length of crack which should close virtually. P_x^0 and P_y^0 are the loading components, which are used for the closure of the crack (Fig. 5).
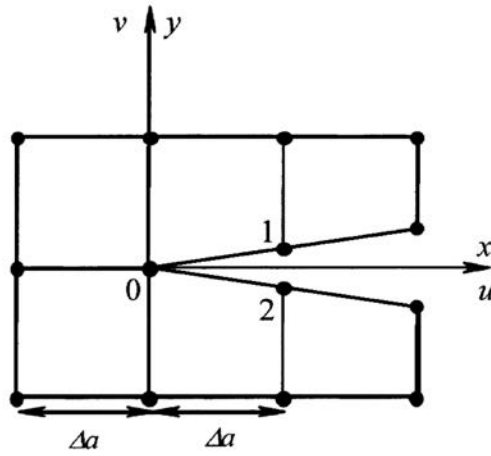
Fig. 5. The shape of elements for VCCT.

7. Finite element model of MMB specimen

For two-dimensional (2D) modeling, we have used four corners solid elements with 8 nodes and three corners solid elements with 6 nodes at crack tip. Since width of the specimen is higher than its thickness, the problem is studied in plane strain state. As the stress concentration zone is smaller than the dimensions of the specimen, the meshes are refined only in a small zone at the crack tip. We refined the meshes so that we obtained converged results. The convergence tolerance of stresses was 0.01 MPa, which was sufficiently precise for our research. Thus we don't need to include the micromechanics of the structure. The type of elements leads to singularity of the stresses and strains at the end of the crack (Fig. 6). The right and left supports of the specimen are modeled by limiting the

displacements of the nodes, but the rotation remained free. The values of the applied loads, depending on the ratio of loading mode, is calculated by relation (4.1) and applied on the nodes.
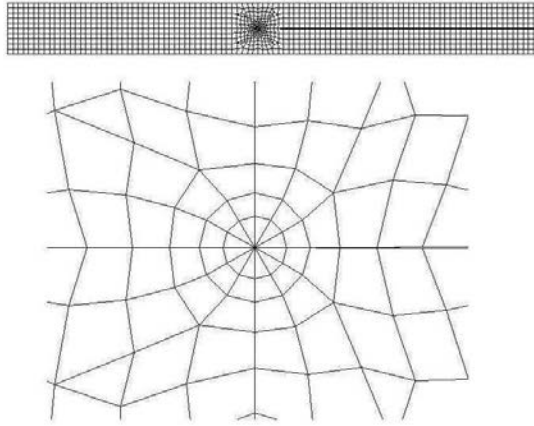
Fig. 6. Mesh generation for 2D finite element analysis.

Each test bar is in contact with two rollers and two hinges through which the load is applied (Fig. 3a). In the 2D finite element modeling, for each contact point, the boundary conditions are applied to the test bar in all of the nodes in the vicinity of the point of load application in order to take into account the contact surface of the roller and the test bar.

In three-dimensional (3D) finite element model, we have used twenty nodes solid elements. The goal of 3D modeling is analyzing the stress and strain energy along the width of specimen [15]. The elements are refined regularly at the width of the crack. The x-axis and y-axis are situated at the crack tip and z-axis is directed along of the width of specimen. As the boundary conditions and dimensions of 3D specimen are symmetrical about to the xy plane, only half of specimen is modelled (Fig. 7).
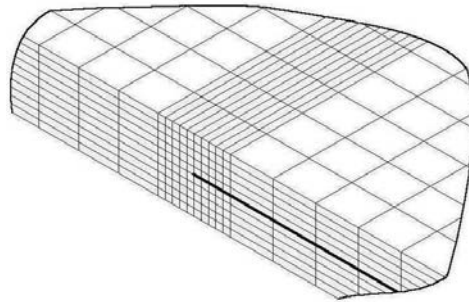
Fig. 7. Mesh generation for 3D finite element analysis.

As the Mode II of delamination is introduced in specimen, for its two cantilever parts, the lower face of the upper cantilever could slide on the upper face of the lower cantilever. So, in 2D and 3D models, contact elements are used.

8. Ruptures in the crack tip

In studying at delamination, identification of the beginning of the crack propagation is a discussible case. In this paper, with using the finite element analysis of specimen, different stresses at the end of the crack are calculated. Using rupture criteria in composite materials and stresses calculated at the crack tip, we analyze the delamination. From the mechanical point of view, fracture of the composite materials with epoxy resin matrix is similar to that occurring in the brittle materials. So the plastic zone in the crack tip is very small and in the theoretical analyses and in the finite element model, the rupture in the crack tip is considered as only elastic.

9. Experimental criterion of rupture

The point of the initiation of crack in an experimental specimen is obtained using three methods. In the first method, the crack growth leads to a deviation of the curve of load-displacement from the linear state. The point of deviation is called NL, which is not always easily distinguishable [16]. In the second method, a line with a slope smaller than 5% of the initial slope of the curve of load-displacement is considered [17]. The intersection of this line with the curve of load-displacement is the starting point of crack propagation. In the third method, point AE (Acoustic Emission), which corresponds to the registration of the first signal during the test, is defined as the beginning of the crack growth. All these criterions are shown in Fig. 8.
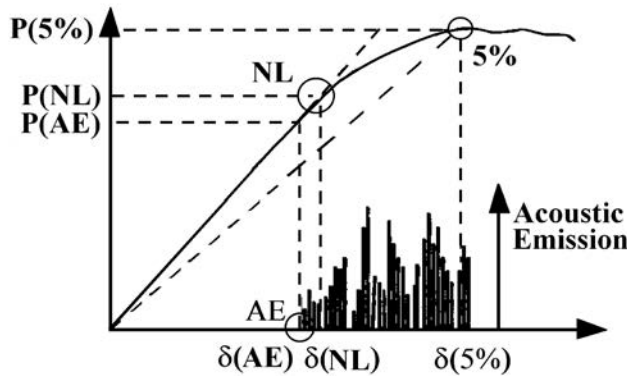
Fig. 8. Mesh generation for 3D finite element analysis.

10. Results and discussion

10.1. 2D Results

Numerical analysis of the specimen is carried out according to the experimental methods, in pure Mode I, pure Mode II, and four ratios of Mode (G_{II}/G_I) 0.25, 0.50, 0.75 and 0.89 which corresponds to the lever length c of 108.3, 56.8, 39 and 31.55mm with an initial crack length of $a_0 = 35$ mm. The stress distribution σ_x has the same shape for all of the mode ratios and it has not a significant influence on the crack growth because of high strength of the composite specimen in the x-axis direction. Figure 9 shows the σ_y stress distribution in crack zone for pure modes loading. The σ_y distribution for the mode ratios, for which Mode I exists, has the shape of two tangent circles (Bean Shape). The maximum stress in y-axis direction has the highest value and is the principal cause of crack growth in Mode I. The lowest value is in x-axis direction. Figure 10 presents the τ_{xy} distribution in crack zone for pure modes loading. The τ_{xy} distribution for the mode ratios in which Mode II exist has a spindle shape. The maximum stress in x-axis direction has the highest value and is the principal cause of crack growth

a) σ_x

b) σ_y

c) τ_{xy}

d) Stress versus the length of crack
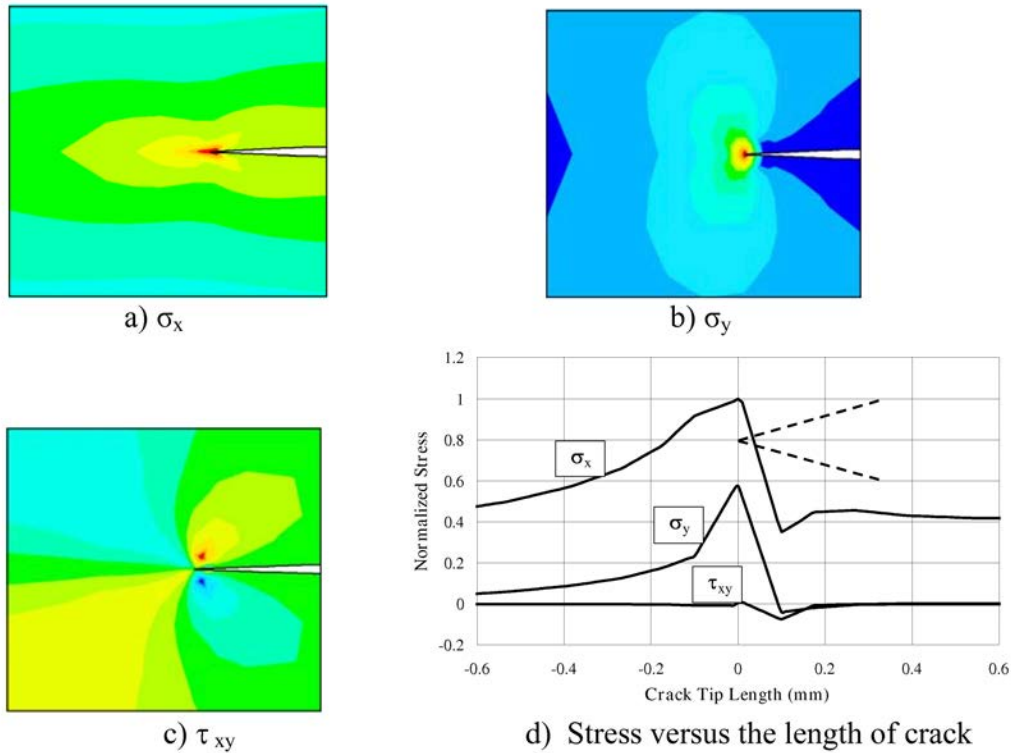
Fig. 9. Stress distribution in crack zone in pure Mode I Loading of 2D model.

in Mode II. The lowest values are observed in y-axis direction. The maximum stress σ_y in pure loading of Mode II and τ_{xy} in pure loading of Mode I occurs in a zone farther than crack tip and it can deviate the crack from its principal route, (Fig. 9b and 10a).

a) σ_x

b) σ_y

c) τ_{xy}

d) Stress versus the length of crack
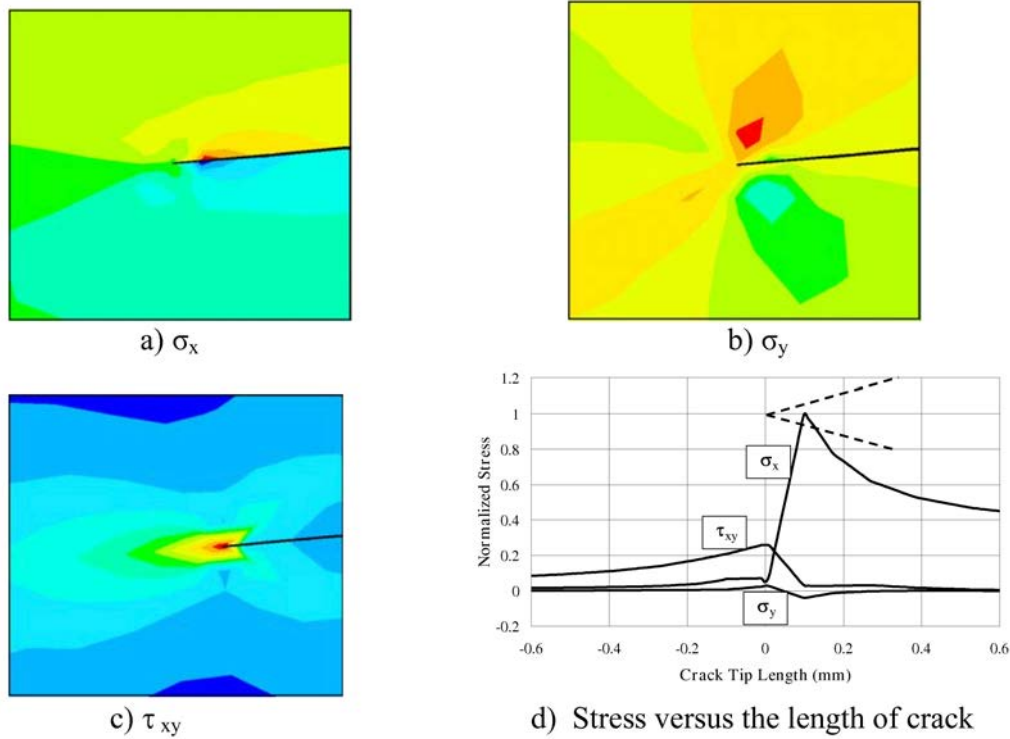
FIG. 10. Stress distribution in crack zone in pure Mode II Loading of 2D model.

Figures 11 and 12 show Mode I and Mode II components of SERR for $G_{II}/G_T = 50\%$ versus the crack length a. The values of SERR of the beam theory G_{BT}, following relation (4.3), the corrected beam theory G_{CBT}, following relation (4.5) and calibration method G_{IC} following relation (5.3), are obtained by substituting the critical values of load and deflection obtained from numerical analysis in the corresponding relations. When the curve of load-displacement reaches its critical value, using VCCT criterion the SERR is calculated at the crack tip. As it can be observed, the strain energy release rate doesn't change too much for different crack lengths. Also the values of G_{CBT} are higher than G_{BT}. In the components of Mode I, G_{vcct} has a well corporation with calibration method, especially with relation (5.4), because the scatter doesn't exceed 1%.
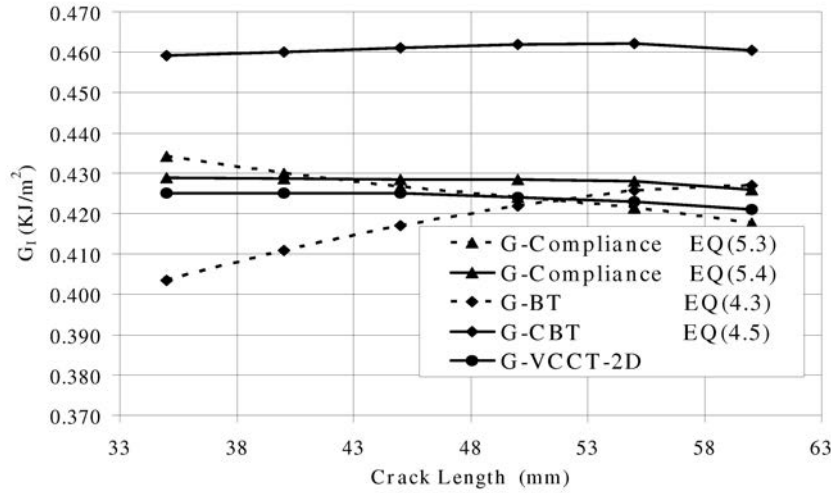
Fig. 11. The Mode I component of SERR versus crack length for the mode ratio
$G_{\mathrm{II}}/G_T = 50\%$ in 2D model.
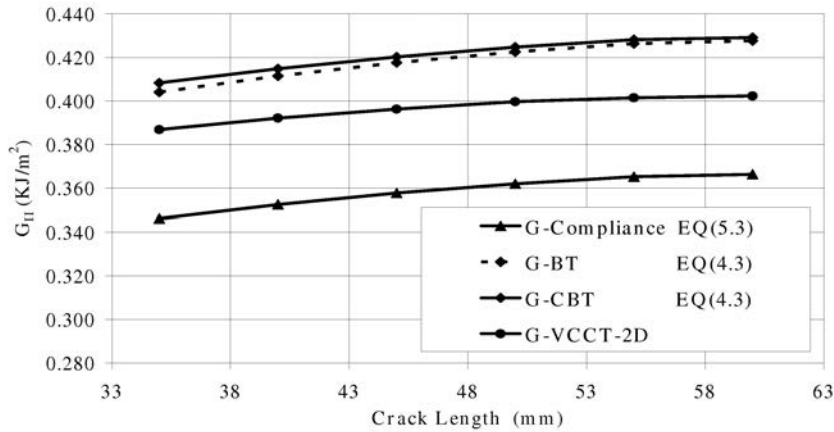
Fig. 12. The Mode II component of SERR versus crack length for the mode ratio
$G_{\mathrm{II}}/G_T = 50\%$ in 2D model.

10.2. 3D Results

Figures 13 to 16 present some of the stress distributions of the 3D specimen on
the plane $(X–Y)$, in the vicinity of the crack. These figures explain the variation
of stress in the width of specimen and 3D effects. In all of the cases, peak of the
curve is situated at crack tip. The highest value of σ_x and σ_y is in the middle
of specimen width and decreases in the margins, (Fig. 13 and 14). On the mode
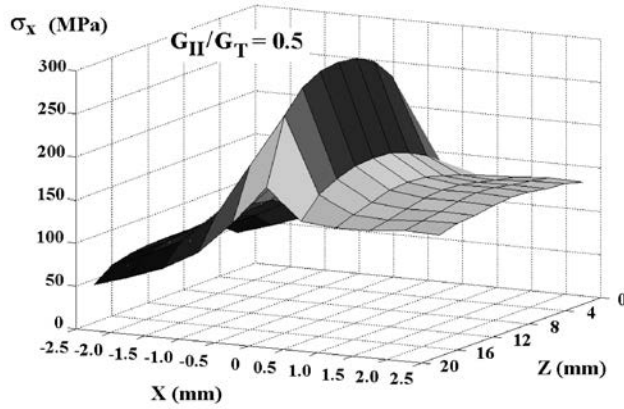
FIG. 13. σ_x distribution in the width of crack in 3D model, for the mode ratio of $G_{II}/G_T = 0.5$.
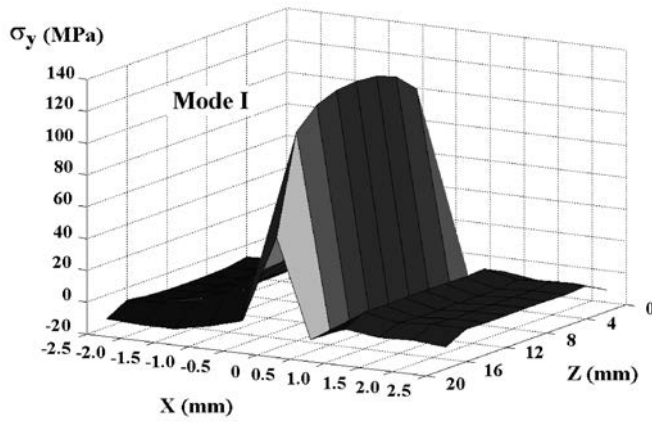
FIG. 14. τ_y distribution in the width of crack in 3D model, for pure Mode I loading.
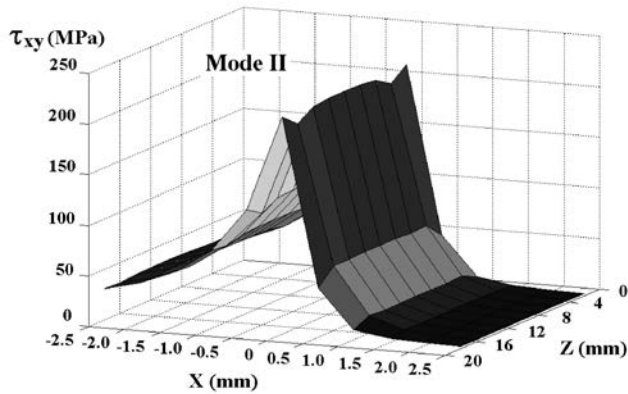
FIG. 15. τ_{xy} distribution in the width of crack in 3D model, for pure Mode II loading.
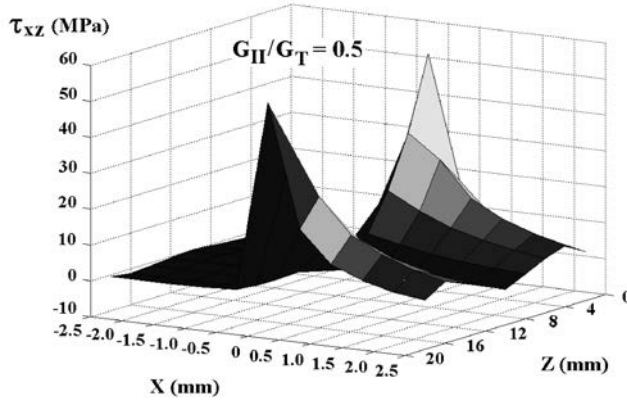
FIG. 16. τ_{xy} distribution in the width of crack in 3D model, for the mode ratio of
$G_{\mathrm{II}}/G_T = 0.5$.

ratios which Mode II loading exists, the transversal strains of the upper and lower
layers of crack plane are in opposite direction on the z-axis. This phenomenon
leads to sliding of these layers on each other, maximize τ_{xz} in the margins and use
a part of the strain energy for the Mode III (Fig. 16). The τ_{xy} stress distribution
is a composition of the above-mentioned cases (Fig. 15).

Figure 17 shows the distribution of SERR components in the specimen width
using VCCT criterion. The shape of their distribution for all ratios of modes
remains as shown, with the difference that their quantity varies upon the ratio
of the modes. For all ratios in which Mode II is associated, we observe a local
increasing of G_{III} in the margins. The G_{total} variation in the different ratio of
modes is influenced by G_{I}, G_{II} and G_{III} behavior (Fig. 18).
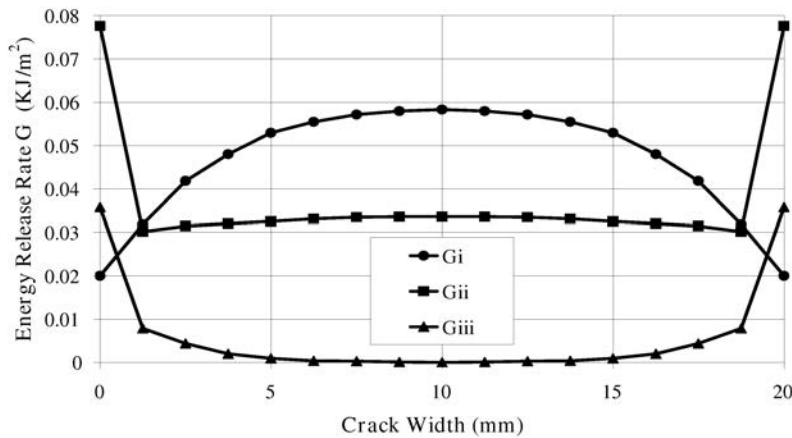
FIG. 17. Distribution of G_{I}, G_{II} and G_{III} in crack width with VCCT for the mode ratio
$G_{\mathrm{II}}/G_T = 0.5$.
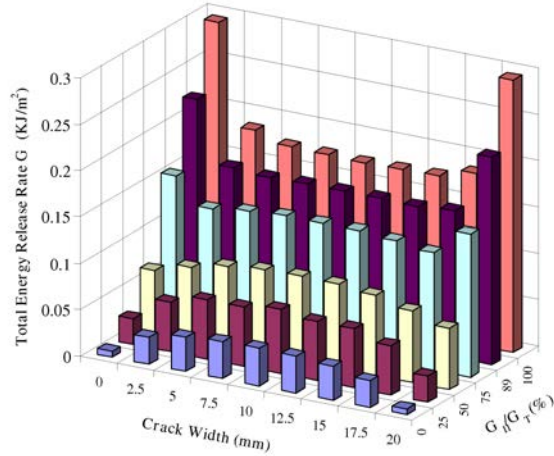
FIG. 18. Distribution of G_T in the crack width with VCCT.

11. CONCLUSION

2D model and plane strain conditions can not explain completely the stress distribution in crack width and regarding the above behaviors, the fracture toughness of the 3D model is lower than the 2D model. 3D effects of model are applied as a percentage of error to the results of fracture toughness of 2D model. The curve of the fracture toughness for a crack length of 35mm, in the tested mixed modes, versus numerical results of 2D and 3D, and also experimental results of 5%, NL and AE criteria, are drawn in Fig. 19. Experimental
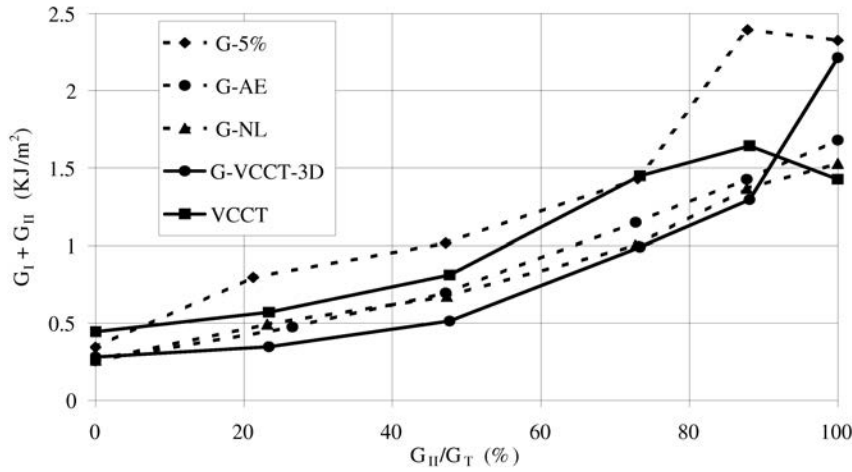
FIG. 19. Fracture toughness using experimental criterions and numerical analysis for different modes of loading.

results of NL and AE have a better agreement with each other, for the ratios of G_{II}/G_T, from 0 to 89%. The fracture toughness of 3D model G_{3D} has decreased in maximum by 39% relative to the fracture toughness of 2D model G_{2D}, and for the pure Mode II loading has increased by 35%. In all the cases with increasing of Mode II loading component, the fracture toughness increases.

Although this finite element code doesn't contain a complete model of the fracture mechanisms at the crack tip, however with taking into account the 3D effect, the numerical results are brought to the vicinity of the experimental results. The effects like friction between the two faces of the crack, kind of the specimen supports and so on, which need statistical studies, should also enter in the mechanisms of the fracture and their influence on the SERR rate should be studied.

References

1. R.M. Jones, *Mechanics of composite materials*, 2-nd edition, Taylor and Francis, Inc. USA, 1999.

2. N.E. Janson, R. Larson, *Rotational interface formulation for delamination analysis of composite laminates*, Computers and Structures, **81**, 2705–2716, 2003.

3. R. Krueger, M. Cvitkovich, K. O'Brien, P. Minguet, *Testing and analysis of composite skin/stringer*, J. Composite Materials, **34**, 15, 1263–1300, 2000.

4. M.R. Khoshravan, A.R. Jami, *Interlaminar stresses in CFRP composites*, Proceeding of the International Conference on Advanced Fibers and Polymer Materials, Oct. 19–21, Shanghai, China, **1**, 338–342, 2005.

5. R. Hertzberg, *Deformation and fracture mechanics of engineering materials*, Section 8.2, Wiley publishing company, 1989.

6. M.R. Khoshravan, M. Monir Vaghefi, *Numerical evaluation of delamination on Mode II in glass fiber reinforced composites*, Engineering Transactions, **53**, 55–68, 2005.

7. F. Ducept, P. Davies, D. Gamby, *An experimental study to validate tests used to determine mixed mode failure criteria of glass/epoxy composite*, Composite Part A 28A, 719–729, 1997.

8. Z. Zou, S.R. Reid, S. Li, *A continuum damage model for delaminations in laminated composites*, J. Mechanics and Physics of Solids, **51**, 333–356, 2003.

9. J.H. Crews, J.R. Reeder, *A mixed mode bending apparatus for delamination testing*, NASA TECHNICAL MEMORANDUM 100662, 1988.

10. J.R. Reeder and J.H. Crews, *Nonlinear analysis and redesign of the mixed mode bending delamination test*, NASA TECHNICAL MEMORANDUM 102777, 1991.

11. F. Ducept, P. Davies, D. Gamby, *Mixed mode failure criteria for a glass/epoxy composite and an adhesively bonded composite/composite joint*, International Journal of Adhesion and Adhesives, **20**, 233–244, 2000.

12. G.R. Irwin, *Fracture Handbook of Physic, VI*, Springer, 551–590, 1958.

13. M.F. Kanninen, *An argumented double cantilever beam model for studying crack propagation and arrest*, International Journal of Fracture, **9**, 1, 83–92,1973.

14. S. Hashemi, A.J. Kinloch, J.G. Williams, *The analysis of interlaminar fracture in uniaxial fiber-polymer composites*, Proceedings of the Royal Society of London, A427,173–199,1990.

15. R. Krueger, T.K. O'Brien, *A shell/3D modeling technique for the analysis of delaminated composite laminates*, J. of Composites, Part A: Applied Science and Manufacturing, **32**, 1, 25–44,2001.

16. P. Davies, *Analysis of G_{IC} interlaminar fracture test*, Applied Composite Materials, Round robin, 1996.

17. ASTM standard E399-81, *Standard test method for plane strain fracture toughness of metallic materials*.

ON PULSATILE HYDROMAGNETIC FLOW OF AN OLDROYD FLUID WITH HEAT TRANSFER

S. S r i n i v a s [1)], T. M a l a t h y[1)], P. L. S a c h d e v[2)]

[1)]**Department of Mathematics**
Vellore Institute of Technology
Deemed University
Vellore – 632 014, India

[2)] **Department of Mathematics**
Indian Institute of Science
Bangalore

The problem of heat transfer to pulsatile flow of hydromagnetic viscoelastic fluid has been studied. Expressions for the velocity, temperature distribution and mass flow rate are obtained. The rate of heat transfer at the plates has also been calculated. These expressions are evaluated numerically for various values of the parameters. The influence of pertinent parameters on temperature, heat transfer coefficient and mass flux has been studied and numerical results obtained are presented graphically.

Key words: Pulsatile flow, Oldroyd fluid, Hartmann number and heat transfer.

1. Introduction

The problems of fluid flow in a channel or pipe have been studied in recent past by many scientists [1–7] with a focus to understand some physical phenomena such as transpiration cooling and gaseous diffusion. In recent years, considerable attention has been given to problems of heat transfer to pulsatile fluid flows [7, 9–16]. The solutions of these problems play a vital role in the study of blood flow in arteries [8, 17]. Radhakrishnamacharya and Maiti [9] have made an investigation of heat transfer to pulsatile viscous fluid flow in a porous channel. Later Ghosh and Debnath [11] analyzed the problem of heat transfer to pulsatile flow in a viscoelastic fluid bounded by impervious rigid parallel plates.

The present paper considers the heat transfer to the pulsatile hydromagnetic flow of a viscoelastic fluid bounded by impervious rigid parallel plates separated by a distance h. The fluid is driven by an unsteady pressure gradient. With the assumption that the upper plate is at a temperature higher than the lower one, the solutions for the steady and fluctuating temperature distributions are

obtained. The rate of heat transfer at the plates is also calculated. Numerical solutions are discussed with graphical representations. It is found that elastic properties of the fluid significantly increase the temperature in the boundary layers near the plates. The magnitude of heat transfer at the plates is also greatly affected by elasticity of the fluid and the Eckert number.

2. Mathematical formulation

We consider the pulsatile flow of a viscoelastic fluid between two infinitely long parallel plates, at a distance h apart, which is driven by the unsteady pressure gradient

$$(2.1) \qquad -\frac{1}{\rho}\frac{\partial p}{\partial x} = A\left\{1 + \varepsilon\exp\left(i\omega t\right)\right\},$$

where A is a known constant, ε is a suitably chosen positive quantity and ω is the frequency. Let the x-axis be along one plate and y-axis normal to it. The plate $y = 0$ and $y = h$ are maintained at uniform temperatures T_0 and $T_1(> T_0)$ respectively. It is assumed that the motion is slow so that all second-order quantities may be neglected. A uniform magnetic field is imposed along the direction normal to the flow. In the analysis, we assume that the induced magnetic field is negligible.

This study is based upon the Oldroyd model of a viscoelastic fluid [6], and the properties of such a fluid are specified by three constants η_0, of the dimension of viscosity, and λ_1, λ_2 of dimensions of time. The equations of the state relating to stress tensor p_{ik} and the rate of strain tensor $e_{ik} = \frac{1}{2}(u_{i,k} + u_{k,i})$ of such fluids are of the form

$$(2.2) \qquad p_{ik} = p'_{ik} - p\delta_{ik},$$

$$(2.3) \qquad \left(1 + \lambda_1\frac{\partial}{\partial t}\right)p'_{ik} = 2\eta_0\left(1 + \lambda_2\frac{\partial}{\partial t}\right)e_{ik},$$

where u_i denotes the velocity vector, δ_{ik} is the Kronecker delta, p_{ik} is the part of the stress tensor related to the change of the shape of a material element, and p is an isotropic pressure. The liquid ($e_{ii} = 0$) described by the above model behaves as a viscous liquid if $\eta_0 > 0$ and $\lambda_1 = \lambda_2$. The equations of motion combined with constitutive equations of the hydromagnetic viscoelastic fluid are given by

$$(2.4) \qquad \left(1 + \lambda_1\frac{\partial}{\partial t}\right)\frac{\partial u}{\partial t} = -\frac{1}{\rho}\left(1 + \lambda_1\frac{\partial}{\partial t}\right)\frac{\partial p}{\partial x}$$
$$+ \nu\left(1 + \lambda_2\frac{\partial}{\partial t}\right)\frac{\partial^2 u}{\partial y^2} - \left(1 + \lambda_1\frac{\partial}{\partial t}\right)\frac{\sigma B_0^2 u}{\rho},$$

(2.5) $$0 = -\frac{1}{\rho}\left(1 + \lambda_1 \frac{\partial}{\partial t}\right)\frac{\partial p}{\partial y},$$

where u is the fluid velocity in the x-direction, σ is the electrical conductivity and B_0 is an imposed uniform magnetic field. The energy equation is

(2.6) $$\rho\, C_p \frac{\partial T}{\partial t} = \chi \frac{\partial^2 T}{\partial y^2} + \mu \left(\frac{\partial u}{\partial y}\right)^2,$$

where $\rho, C_p, \chi, \mu, \nu$ are respectively the density, specific heat, thermal conductivity, coefficient of dynamic viscosity and coefficient of kinematic viscosity, and λ_1 and λ_2 are the relaxation and retardation times respectively.

The boundary conditions are

(2.7) $$u = 0, \quad T = T_0 \quad \text{at} \quad y = 0,$$

(2.8) $$u = 0, \quad T = T_1 \quad \text{at} \quad y = h.$$

The solution of (2.4) has the form

(2.9) $$u^* = \frac{u}{\left(\dfrac{Ah^2}{\nu}\right)} = u_0 + \varepsilon u_1 e^{i\tau}; \qquad \tau = \omega t,$$

where

(2.10) $$u_0 = \frac{1}{H^2}\left\{1 - \frac{\sinh H(1 - \eta) + \sinh H\eta}{\sinh H}\right\},$$

(2.11) $$u_1 = \frac{1}{\beta_2^2}\left\{1 - \frac{\sinh \beta_1(1 - \eta) + \sinh \beta_1\eta}{\sinh \beta_1}\right\}$$

with

$$\eta = \frac{y}{h}, \qquad H^2 = \frac{h^2\sigma B_0^2}{\mu}, \qquad R_*^2 = \frac{\omega h^2}{\nu}, \qquad \nu = \frac{\mu}{\rho}, \qquad \beta^2 = \frac{1 + iF_1}{1 + iF_1F_2},$$

(2.12)
$$F_1 = \lambda_1\omega, \qquad F_2 = \frac{\lambda_2}{\lambda_1}\,(< 1),$$

$$\beta_1^2 = \beta^2\left(H^2 + iR_*^2\right), \qquad \beta_2^2 = H^2 + iR_*^2$$

It can be noted that the results for viscous fluid correspond to the case $\lambda_2 = \lambda_1$, i.e. $F_2 = 1$, independent of the values of F_1.

Introducing (2.12) and the dimensionless temperature

(2.13) $$\theta = \frac{T - T_0}{T_1 - T_0}$$

in (2.6), the energy equation becomes

(2.14) $$R_*^2 \frac{\partial \theta}{\partial \tau} = \frac{1}{P_r} \left(\frac{\partial^2 \theta}{\partial \eta^2} \right) + E_c \left(\frac{\partial u^*}{\partial \eta} \right)^2 ,$$

where $P_r = \dfrac{\mu C_p}{\chi}$ is the Prandtl number, and $E_c = \dfrac{A^2 h^4}{\nu^2 C_p (T_1 - T_{0)}}$ is the Eckert number. The boundary conditions for θ are

(2.15) $$\theta = 0 \quad \text{at} \quad \eta = 0,$$

(2.16) $$\theta = 1 \quad \text{at} \quad \eta = 1.$$

In view of (2.9), the temperature θ can be assumed in the form

(2.17) $$\theta(\eta, t) = \theta_0(\eta) + \varepsilon F(\eta) e^{i\tau} + \varepsilon^2 G_1(\eta) e^{2i\tau}.$$

Substituting (2.17) and u* in (2.14), equating the harmonic terms, retaining coefficients of ε^2 and solving the corresponding equations for $\theta_0, F(\eta)$ and $G_1(\eta)$ with the help of (2.15) and (2.16), we obtain

(2.18) $$\theta_0(\eta) = \eta + \frac{P_r E_c}{4H^2} \left\{ \eta(\eta - 1) \left[1 - \frac{(\cosh H - 1)^2}{\sinh^2 H} \right] \right.$$

$$\left. + 2 \left[\frac{\cosh H - 1}{H^2 \sinh^2 H} \right] \sinh H\eta. \sinh H(1 - \eta) \right\},$$

(2.19) $$F(\eta) = -L(0) \left\{ \cosh N\eta + \left(\frac{1 - \cosh N}{\sinh N} \right) \sinh N\eta \right\} + L(\eta),$$

(2.20) $$L(\eta) = -\frac{4\beta_1 P_r E_c}{\beta_2^2 H \sinh H. \sinh \beta_1} . \sinh \left(\frac{H}{2} \right) \sinh \left(\frac{\beta_1}{2} \right)$$

$$\left\{ \frac{1}{\beta_1^2 - N^2 + H(H + 2\beta_1)} \cosh \left[\frac{(H + \beta_1)(1 - 2\eta)}{2} \right] \right.$$

$$\left. - \frac{1}{\beta_1^2 - N^2 + H(H - 2\beta_1)} \cosh \left[\frac{(H - \beta_1)(1 - 2\eta)}{2} \right] \right\},$$

$$(2.21) \quad L(0) = L(1) = -\frac{4\beta_1 P_r E_c}{\beta_2^2 H \sinh H . \sinh \beta_1} . \sinh\left(\frac{H}{2}\right) \sinh\left(\frac{\beta_1}{2}\right)$$

$$\left\{ \frac{1}{\beta_1^2 - N^2 + H(H + 2\beta_1)} \cosh\left(\frac{H + \beta_1}{2}\right) \right.$$

$$\left. -\frac{1}{\beta_1^2 - N^2 + H(H - 2\beta_1)} \cosh\left(\frac{H - \beta_1}{2}\right) \right\},$$

where

$$(2.22) \quad N = n(1 + i), \qquad n = R_*\left(\frac{P_r}{2}\right)^{1/2},$$

and

$$(2.23) \quad G_1(\eta) = -\frac{1}{\sinh \sqrt{2}N}\left[G_2(0) \sinh \sqrt{2}N(1 - \eta) \right.$$

$$\left. + G_2(1) \sinh \sqrt{2}N\eta \right] + G_2(\eta),$$

$$(2.24) \quad G_2(\eta) = \frac{P_r E_c \beta_1^2}{2\beta_2^4 \sinh^2 \beta_1}\left[\frac{1 - \cosh \beta_1}{N^2} \right.$$

$$-\left(\frac{1 + \cosh 2\beta_1 - 2\cosh \beta_1}{2\left(2\beta_1^2 - N^2\right)} \right) \cosh 2\beta_1\eta$$

$$\left. +\frac{(\sinh 2\beta_1 - 2\sinh \beta_1)}{2\left(2\beta_1^2 - N^2\right)} \sinh 2\beta_1\eta \right],$$

$$(2.25) \quad G_2(0) = G_2(1) = \frac{P_r E_c \beta_1^2}{2\beta_2^4 \sinh^2 \beta_1}\left[\frac{1 - \cosh \beta_1}{N^2} \right.$$

$$\left. -\left(\frac{1 + \cosh 2\beta_1 - 2\cosh \beta_1}{2\left(2\beta_1^2 - N^2\right)} \right) \right].$$

The instantaneous mass flux Q may be obtained by integrating Eq. (2.9) across the channel:

$$(2.26) \quad \frac{Q}{\left(\frac{Ah^3}{\nu}\right)} = \frac{1}{H^2}\left[1 + 2\left(\frac{1 - \cosh H}{H \sinh H}\right) \right] + \frac{\varepsilon e^{i\omega t}}{\beta_2^2}\left[1 + 2\left(\frac{1 - \cosh \beta_1}{\beta_1 \sinh \beta_1}\right) \right].$$

3. Rate of heat transfer

The rate of heat transfer per unit area at the plate $\eta = 0$ is given by

$$Q_0' = -\frac{q_0 h}{\chi(T_1 - T_0)} = \left(\frac{\partial \theta}{\partial \eta}\right)_{\eta=0},$$

$$Q_0' = \left(\frac{d\theta_0}{d\eta}\right)_{\eta=0} + \varepsilon e^{i\omega t} \left(\frac{dF}{d\eta}\right)_{\eta=0} + \varepsilon^2 e^{2i\omega t} \left(\frac{dG_1}{d\eta}\right)_{\eta=0},$$

(3.1) $$Q_0' = 1 + \frac{P_r E_c}{H^2} \left\{ \left(\frac{\cosh H - 1}{\sinh^2 H}\right) \left(\frac{2\sinh H}{H} + (\cosh H - 1)\right) - 1 \right\}$$

$$+ \varepsilon e^{i\omega t} \left[\frac{-NL(0)}{\sinh N} (1 - \cosh N) + \frac{4\beta_1 P_r E_c}{\beta_2^2 H \sinh H \sinh \beta_1} \cdot \sinh\left(\frac{H}{2}\right) \sinh\left(\frac{\beta_1}{2}\right) \right.$$

$$\left\{ \frac{(H + \beta_1)\sinh\left(\frac{H + \beta_1}{2}\right)}{\beta_1^2 - N^2 + H(H + 2\beta_1)} - \frac{(H - \beta_1)\sinh\left(\frac{H - \beta_1}{2}\right)}{\beta_1^2 - N^2 + H(H - 2\beta_1)} \right\} \right] + \varepsilon^2 e^{2i\omega t}$$

$$\left\{ \frac{-G_2(0)\sqrt{2}N}{\sinh \sqrt{2}N} \left(1 + \cosh \sqrt{2}N\right) + \frac{P_r E_c \beta_1^3 (\sinh 2\beta_1 - 2\sinh \beta_1)}{2\beta_2^4 \left(2\beta_1^2 - N^2\right) \sinh^2 \beta_1} \right\}$$

$$= \left(\theta_0'\right)_{\eta=0} + \varepsilon |D_0| \cos(\omega t + \alpha_0) + \cdots,$$

where $D_0 = D_{0r} + iD_{0i}$ and $\tan \alpha_0 = D_{0i}/D_{or}$.

Similarly, the rate of heat transfer per unit area at the plate $\eta = 1$ is given by

$$Q_1' = -\frac{q_1 h}{\chi(T_1 - T_0)} = \left(\frac{\partial \theta}{\partial \eta}\right)_{\eta=1},$$

(3.2)

$$Q_1' = 1 + \frac{P_r E_c}{H^2} \left[1 - \left(\frac{\cosh H - 1}{\sinh^2 H}\right) \left((\cosh H - 1) + \frac{2\sinh H}{H}\right) \right]$$

$$+ \varepsilon e^{i\omega t} \left\{ -NL(0) \left(\sinh N + \left(\frac{1 - \cosh N}{\sinh N}\right) \cosh N\right) \right.$$

(3.2)
[cont.]

$$- \frac{4\beta_1 P_r E_c}{\beta_2^2 H \sinh H \sinh \beta_1} \cdot \sinh\left(\frac{H}{2}\right) \sinh\left(\frac{\beta_1}{2}\right)$$

$$\left[\frac{H + \beta_1}{\beta_1^2 - N^2 + H(H + 2\beta_1)} \cdot \sinh\left(\frac{H + \beta_1}{2}\right) \right.$$

$$\left. - \frac{(H - \beta_1)}{\beta_1^2 - N^2 + H(H - 2\beta_1)} \sinh\left(\frac{H - \beta_1}{2}\right) \right] \right\}$$

$$+ \varepsilon^2 e^{2i\omega t} \left\{ \frac{-\sqrt{2} N G_2(0)}{\sinh \sqrt{2} N} \left[\cosh \sqrt{2} N - 1 \right] + \frac{P_r E_c \beta_1^3}{\beta_2^4 \sinh^2 \beta_1} \right.$$

$$\left[\left(\frac{\sinh 2\beta_1 - 2 \sinh \beta_1}{2(2\beta_1^2 - N^2)} \right) \cosh 2\beta_1 - \left(\frac{1 + \cosh 2\beta_1 - 2 \cosh \beta_1}{2(2\beta_1^2 - N^2)} \right) \sinh 2\beta_1 \right] \right\}$$

$$= \left(\theta_0' \right)_{\eta=1} + \varepsilon |D_1| \cos(\omega t + \alpha_1) + \cdots,$$

where $D_1 = D_{1r} + i D_{1i}$ and $\tan \alpha_1 = D_{1i}/D_{1r}$.

4. Numerical results and discussion

In order to get the physical insight of the problem, velocity, temperature field, mass flow and rate of heat transfer have been discussed by assigning numerical values to various parameters obtained in mathematical formulation of the problem and the results are shown graphically.

From Fig. 1a, it can be observed that when the frequency R_* is small, the unsteady velocity profile is almost parabolic. Also it can be noted that the unsteady velocity decreases with the increasing values of the Hartmann number. Part of the unsteady velocity profile is nearly linear as the frequency increases and the maximum occurs in the central part of the channel, Fig. 1b. If the frequency is large, the maxima of the velocity are shifted to the boundary layers near the walls, Figs. 1c and 1d.

The effects of the velocity profiles for different values of the Hartmann number and frequency parameter are shown in Figs. 2a and 2b. It can be observed from Fig. 2a that the velocity u of the fluid in the x-direction decreases due to increase of the Hartmann number H. As the frequency parameter increases, we can note from Figs. 2b and 2c that velocity decreases

The magnitude of the mass flux of $\frac{Q\nu}{Ah^3}$ is plotted in Figs. 3a and 3b. It can be observed that mass flux decreases as the frequency parameter and Hartmann number increases.

a)
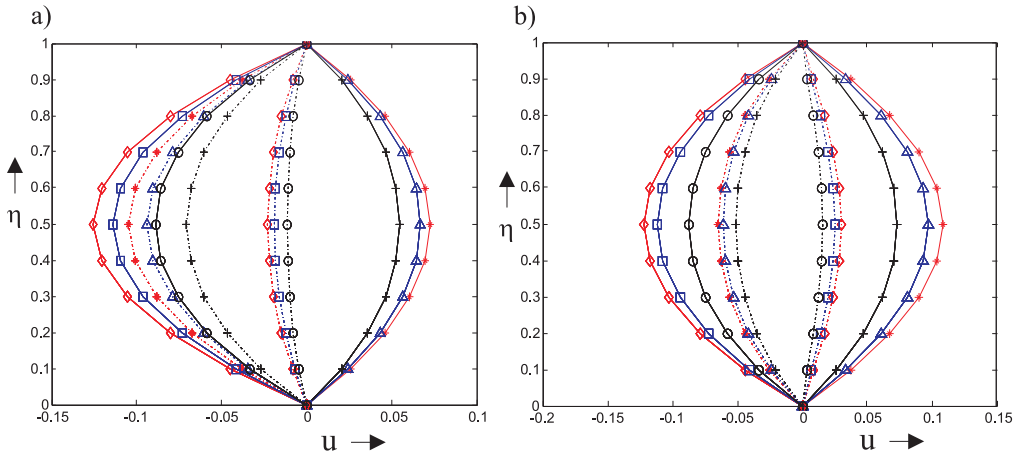
$F_1 = 0.2,\ F_2 = 0.08,\ P_r = 100,\ R_* = 0$

b)

$F_1 = 0.2,\ F_2 = 0.08,\ P_r = 100,\ R_* = 2$

c)

$F_1 = 0.2,\ F_2 = 1,\ P_r = 100,\ R_* = 9$

d)
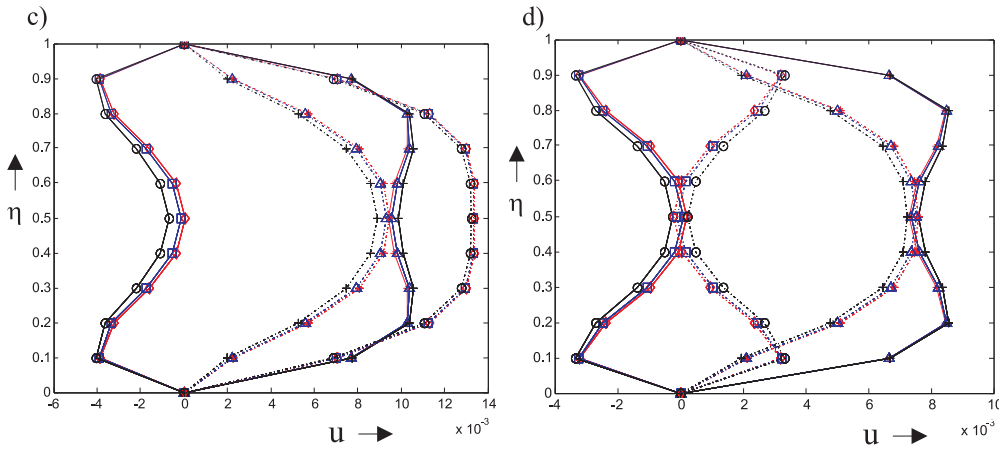
$F_1 = 0.2,\ F_2 = 1,\ P_r = 100,\ R_* = 10$

$*\underline{\quad}*$	$H = 0,$	$\triangle\underline{\quad}\triangle$	$H = 1,$	$+\underline{\quad}+$	$H = 2,$	$\omega t = \pi/4$
$\Diamond - \cdot - \Diamond$	$H = 0,$	$\square - \cdot - \square$	$H = 1,$	$\mathrm{o} - \cdot - \mathrm{o}$	$H = 2,$	$\omega t = \pi/2$
$* - \cdot - *$	$H = 0,$	$\triangle - \cdot - \triangle$	$H = 1,$	$+ - \cdot - +$	$H = 2,$	$\omega t = 3\pi/4$
$\Diamond\underline{\quad}\Diamond$	$H = 0,$	$\square - \square$	$H = 1,$	$\mathrm{o} - \cdot - \mathrm{o}$	$H = 2,$	$\omega t = \pi$

FIG. 1. Unsteady velocity profiles.

a)
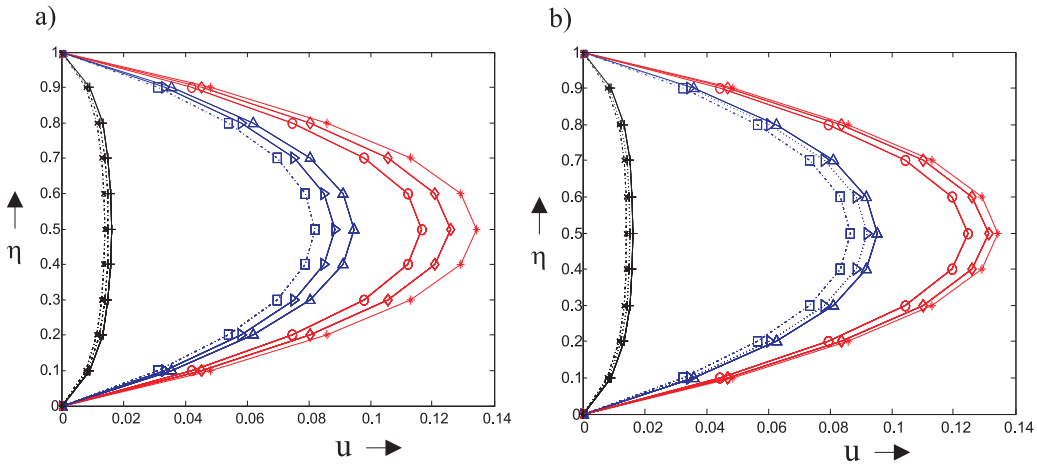
$F_1 = 0.2,\ F_2 = 0.8,\ P_r = 100,\ R_* = 1,\ \varepsilon = 0.1$

b)

$F_1 = 0.2,\ F_2 = 0.8,\ P_r = 100,\ R_* = 3,\ \varepsilon = 0.1$

c)
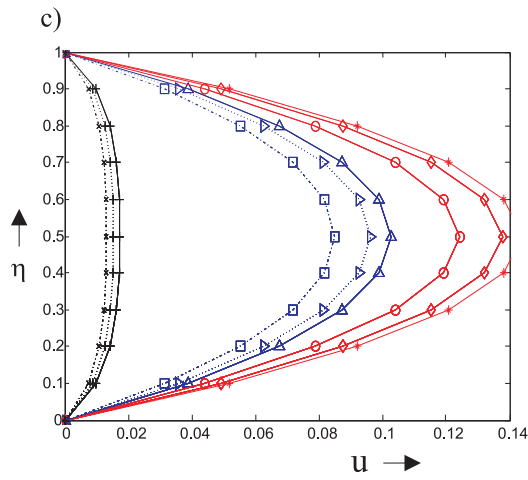
$F_1 = 0.2,\ F_2 = 0.8,\ P_r = 100,\ R_* = 3,\ \varepsilon = 0.2$

$*\underline{\quad}*$	$H = 0,$	$\Delta\underline{\quad}\Delta$	$H = 2,$	$+\underline{\quad}+$	$H = 8,\quad \omega t = \pi/4$
$\Diamond\underline{\quad}\Diamond$	$H = 0,$	$\triangleright\underline{\quad}\triangleright$	$H = 2,$	$+-\cdot-+$	$H = 8,\quad \omega t = \pi/2$
$o\underline{\quad}o$	$H = 0,$	$\square-\cdot-\square$	$H = 2,$	$\times-\cdot-\times$	$H = 8,\quad \omega t = 3\pi/4$

Fig. 2. Velocity profiles.

a)

b)

$F_1 = 0.1,\ F_2 = 0.2,\ P_r = 100$ $F_1 = 0.1\ F_2 = 1,\ P_r = 100$

____ $H = 0$,   +____+ $H = 0.2$, $\triangle$____$\triangle$ $H = 0.4$, $\omega t = \pi/4$

$\circ - \cdot - \circ$ $H = 0$, $\diamond - \cdot - \diamond$ $H = 0.2$, $\triangleright - \cdot - \triangleright$ $H = 0.4$ $\omega t = \pi/2$

$\triangleleft$ ___ $\triangleleft$ $H = 0$, $\square$___$\square$ $H = 0.2$,   ____ $H = 0.4$, $\omega t = 3\pi/4$
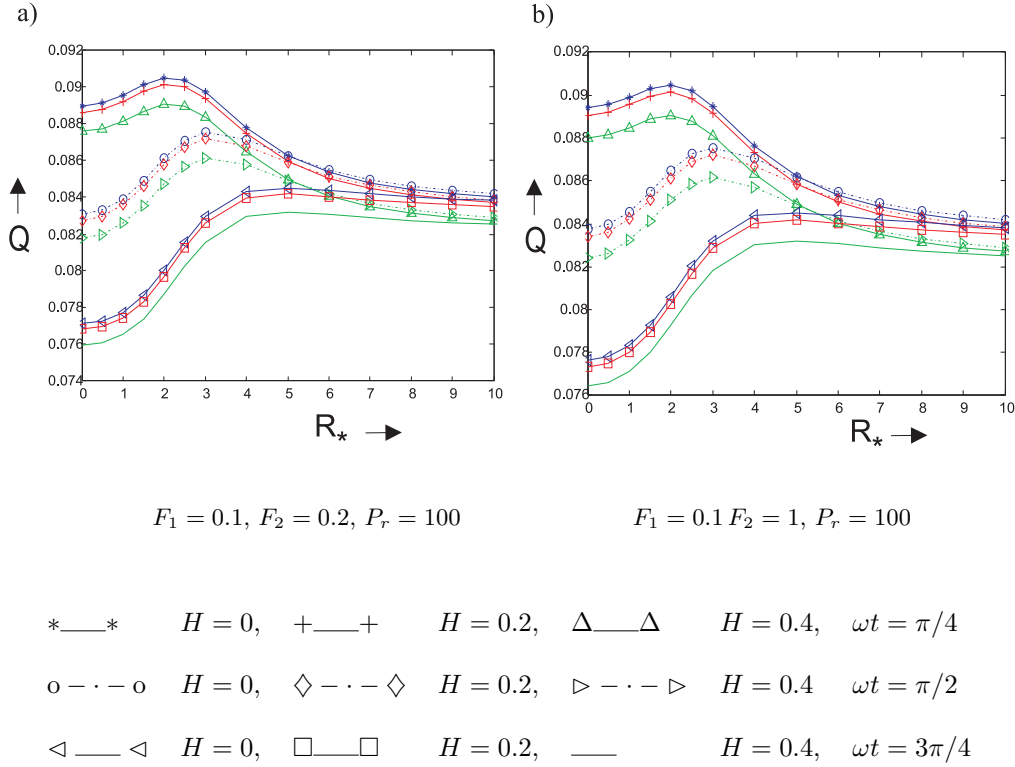
FIG. 3. Magnitude of the mass flux.

In the problem under investigation, θ_0 represents the steady temperature distribution in the fluid. The expression for θ_0 given by (2.18) remains the same for both a viscous and a viscoelastic fluid of Oldroyd type under similar conditions. Figure 4 depicts the steady temperature profiles corresponding to θ_0 for various values of $P_r E_c$. The steady temperature profiles plotted in Figs. 4a, 4b, 4c are almost parabolic and temperature decreases with increase of the Hartmann number. Further it can be noticed that the increase in Hartmann number decreases the rate of heat transfer. We note that there is no change in the character of the profiles as E_c varies. But as the Eckert number E_c increases, the steady temperature increases. Regarding the rate of heat transfer in the steady – state condition the reversal of heat flux from the fluid to the hotter plate takes place when $P_r E_c > 22$ which, in turn, makes the hotter plate more hot. In fact, the value of $P_r E_c$ provides a measure of the amount of heat generated due to friction which, in the present case, increases with the increase of the pressure gradient. If the temperature difference between the plates is fixed, heat flows

a)

$F_1 = 0.2,\ F_2 = 0.8,\ H = 0,\ E_c = 1,$

b)

$F_1 = 0.2,\ F_2 = 0.8,\ H = 2,\ E_c = 1,$

$F_1 = 0.2,\ F_2 = 0.8,\ H = 3,\ E_c = 1$
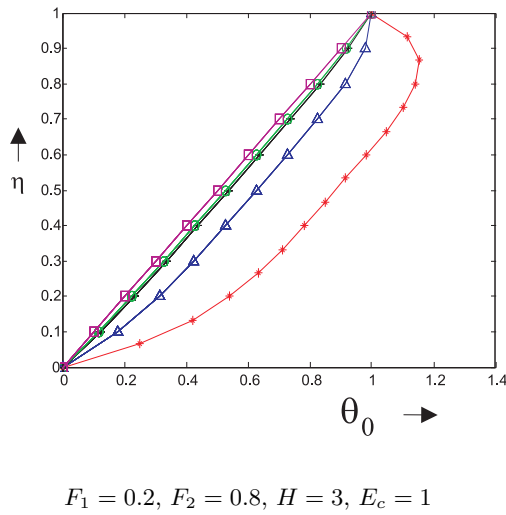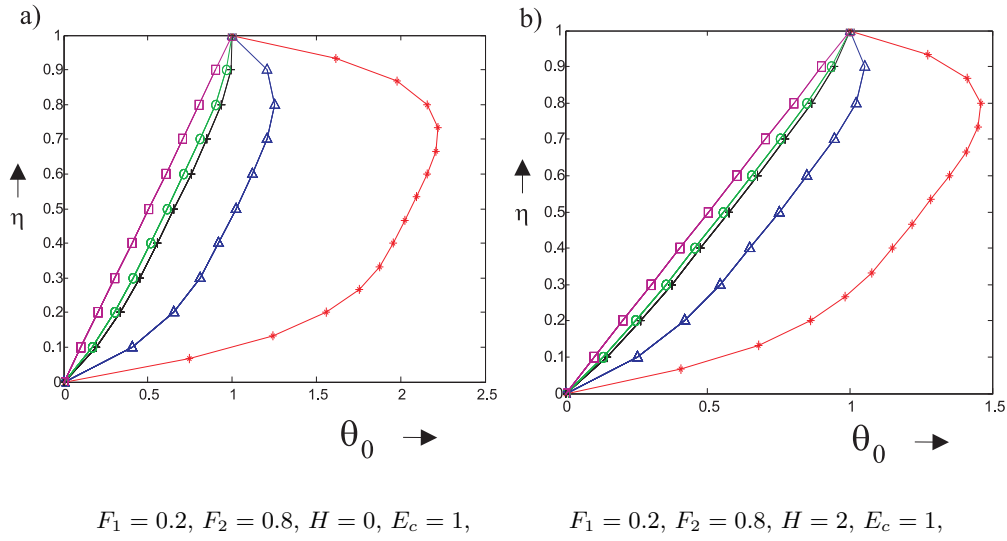
$*\underline{\quad}*\quad P_r = 300,\quad \Delta\underline{\quad}\Delta\quad P_r = 100,\quad +\underline{\quad}\quad P_r = 30,$

$\mathrm{o}\underline{\quad}\mathrm{o}\quad P_r = 22,\quad \square\underline{\quad}\square\quad P_r = 1.$

FIG. 4. Steady temperature profiles.

from the hotter plate to the fluid as long as the pressure gradient does not exceed a certain value, i.e for $P_r E_c$ to be not greater than 22. This phenomenon

is important for cooling at high pressure gradients. The effect of changing the Hartmann number (for fixed E_c) and changing Eckert number (for fixed H) are shown in Tables 1 and 2. Table 1 shows that the rate of heat transfer from the lower plate decreases with Hartmann number, whereas it increases in the upper plate. We observe from Table 2 that the rate of heat transfer from the lower plate increases with E_c while at the upper plate, the heat flows from the fluid to the plate even if $T_1 > T_0$.

Table 1.

$E_c = 1, P_r = 100, R_* = 1$

	$H = 0$	$H = 1$	$H = 2$	$H = 3$
$(\theta_0')_{\eta=0}$	17.6518	14.7787	9.5485	5.69695
$(\theta_0')_{\eta=1}$	-15.6518	-12.7787	-7.5405	-3.6969

Table 2.

$P_r = 10, H = 1.5, R_* = 1$

	$E_c = 1$	2	3	5
$(\theta_0')_{\eta=0}$	2.1123	3.2247	4.3371	6.5618
$(\theta_0')_{\eta=1}$	-0.11235	-1.22471	-2.33706	-4.56177

Fixing P_r and R_*, the instantaneous temperature profiles are plotted in Figs. 5a–5e, enabling us to observe the effect of changing H (with E_c fixed) and changing E_c (with H fixed). It also depicts the effect of changing values of the elastic parameters F_1 and F_2. It can be noted that $F_2 = 1$ always represent the case of a viscous fluid irrespective of the values of F_1. From Figs. 5a–5e, it can be seen that temperature decreases as H increases. The temperature profiles are almost parabolic for small values of H, but they oscillate more for large values of H and the maximum temperature is shifted to the boundary layers near the walls. The temperature increases rapidly with increase in E_c, which may be due to high viscous dissipation. Comparison of Figs. 5b and Fig. 5c shows that the presence of the elasticity of the fluid increases the temperature in a region near the plate and gradually diminishes the same at the central part of the channel. This study indicates that the temperature in a viscoelastic fluid increases rapidly with the increase of E_c and also interestingly we find that the increase of temperature near the plate occurs mainly due to the increase of the relaxation time of the fluid, while the increase in retardation time of the fluid produces a gradual decrease of temperature at the central part of the channel. It can be

observed that there is no significant change in the character of the profile as E_c varies.

The effect of changing elastic parameters and changing H (for fixed E_c) and changing R_* (for fixed E_c) and changing E_c (for fixed H), on the values of the amplitude and phase of the rate of heat transfer is shown in Tables 3, 4 and 5. In Table 3, it is observed for a viscoelastic fluid the increase in Hartmann number decreases the amplitude of heat transfer at both the plates. There is a phase lag at both the plates when the fluid is viscoelastic. It may be observed from Table 4 that at the lower plate there is a phase lag at higher frequency, but at the upper plate there is a phase lead. We also find that at both the plates the amplitude decreases uniformly with frequency for fixed E_c. It can be noticed from Table 5 for fixed R_* the amplitude increases uniformly with E_c at both the walls. The increase of the Eckert number E_c increases the amplitude of heat transfer at the plates for the viscoelastic fluid, while the phase at the plates remains unaffected by the increase of E_c.

Table 3.

$P_r = 200, R_* = 10, F_1 = 0.1, F_2 = 0.5, E_c = 3$

H	$|D_0|$	$|D_1|$	$\tan \alpha_0$	$\tan \alpha_1$
0	0.261855	0.0231703	-29.0306	12.9313
0.2	0.260977	0.0231044	-28.8304	12.8729
0.4	0.258385	0.0229097	-28.2463	12.7017

Table 4.

$P_r = 200, \ F_1 = 0.1, \ F_2 = 0.4, \ H = 0.3, \ E_c = 5.$

R_*	$|D_0|$	$|D_1|$	$\tan \alpha_0$	$\tan \alpha_1$
5	2.73881	0.265488	-61.0054	5.35171
10	0.649884	0.0575502	-25.151	14.5618
15	0.29009	0.0244279	-29.1139	33.4444

Table 5.

$P_r = 200, \ F_1 = 0.1, \ F_2 = 0.5, \ H = 0.2, \ R_* = 5.$

E_c	$|D_0|$	$|D_1|$	$\tan \alpha_0$	$\tan \alpha_1$
5	2.74875	0.266414	-84.1425	5.12845
10	5.49751	0.532828	-84.1425	5.12845
15	8.24626	0.799242	-84.1425	5.12845

a) ... b)
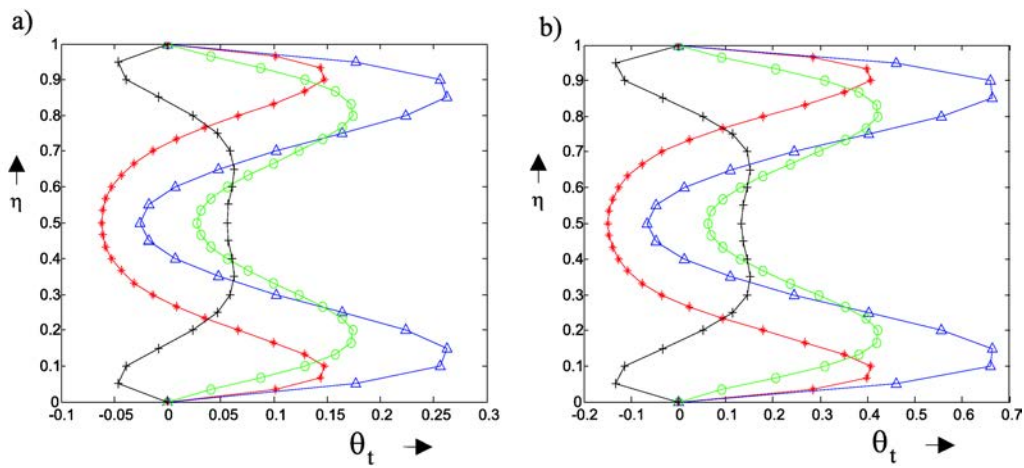
$F_1 = 0.02$, $F_2 = 0.05$, $H = 0$, $P_r = 100$, $R_* = 1$, $E_c = 1$,

$F_1 = 0.02$, $F_2 = 0.05$, $H = 2$, $P_r = 100$, $R_* = 1$, $E_c = 5$

$*\underline{\quad}*$ $\omega t = 0$, $\Delta\underline{\quad}\Delta$ $\omega t = \pi/4$,

$o\underline{\quad}o$ $\omega t = \pi/2$ $+\underline{\quad}+$ $\omega t = 3\pi/4$
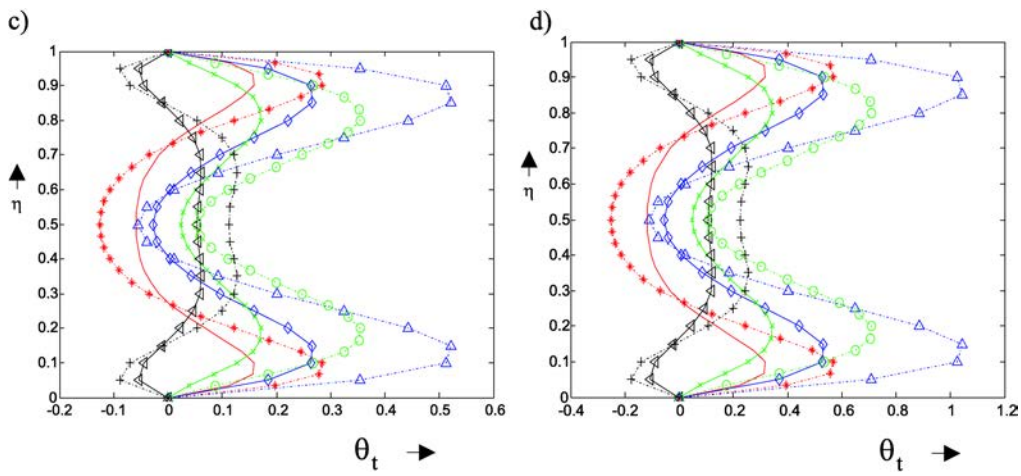
$F_1 = 0.02$, $F_2 = 1$, $P_r = 100$, $R_* = 1$, $E_c = 2$, $F_1 = 0.02$, $F_2 = 1$, $P_r = 100$, $R_* = 1$, $E_c = 4$,

[Fig. 5]
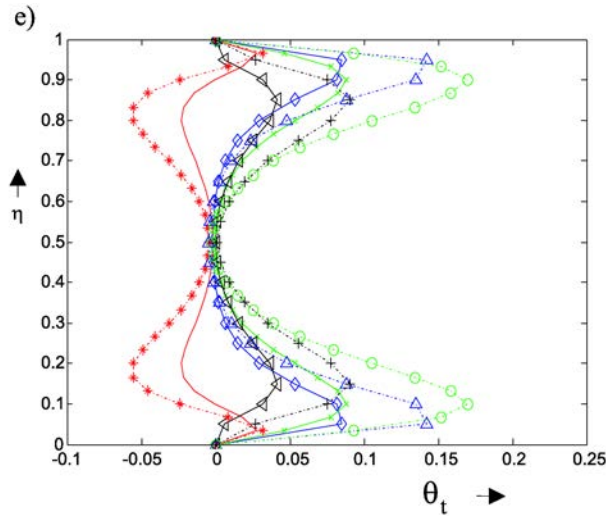
$F_1 = 0.02,\ F_2 = 1,\ P_r = 100,\ R_* = 2,\ E_c = 2$

——	$H = 2$	$\omega t = 0,$		$^{*}-\cdot-^{*},$	$H = 0,$	$\omega t = 0,$
$\diamond\!\!-\!\!\diamond$	$H = 2$	$\omega t = \pi/4,$		$\triangle-\cdot-\triangle$	$H = 0,$	$\omega t = \pi/4,$
$\times\!\!-\!\!\times$	$H = 2,$	$\omega t = \pi/2,$		$\mathrm{o}-\cdot-\mathrm{o}$	$H = 0,$	$\omega t = \pi/2,$
$\triangleleft\!\!-\!\!\triangleleft$	$H = 2,$	$\omega t = 3\pi/4,$		$+-\cdot-+$	$H = 0,$	$\omega t = 3\pi/4.$

Fig. 5. Unsteady temperature profiles.

References

1. A.S. Berman, *Laminar flow in channels with porous walls*, J. Appl. Phys., **24**, 1232–1235, 1953.

2. J.R. Sellars, *Laminar flow in channels with porous walls at high suction Reynolds numbers*, J. Appl. Phys., **26**, 489–490, 1955.

3. S.W. Yuan, Further investigation of laminar flow in channels with porous walls, J. Appl. Phys., **27**, 267–269, 1956.

4. M. Morduchow, *On laminar flow through a channel or tube with injection – application of method of averages*, Q.J. Appl. Math., **14**, 361–368, 1956.

5. A.S. BERMAN, *Laminar flow in an annulus with porous walls*, J. Appl. Phys., **29**, 71–75, 1958.

6. J.G. OLDROYD, *Non-Newtonian effects in steady motion of some idealized elastico-viscous liquids*, Proc. Roy. Soc. Lond., **A245**, 278–297, 1958.

7. Y.C. WANG, *Pulsatile flow in a porous channel*, J. Appl. Mech., **38**, 553–555, 1971.

8. S.A. VICTOR and V.L. SHAH, *Heat transfer to blood flowing in a tube*, Biorheology, **12**, 361–368, 1975.

9. G. RADHAKRISHNAMACHARYA and M.K. MAITI, *Heat transfer to pulsatile flow in a porous channel*, Int. J. Heat Mass Transfer, **20**, 171–173, 1977.

10. A.S. MUZUMDAR, *Advances in transport process*, Vol. 1, Wiley Eastern Ltd., 1980.

11. A.K. GHOSH and L. DEBNATH, *On heat transfer to pulsatile flow of a viscoelastic fluid*, Acta Mechanica, **93**, 169–177, 1992.

12. N. DATTA and D.C. DALAL, *Pulsatile flow and heat transfer of a dusty fluid through an infinitely long annular pipe*, Int. J. Multiphase flow, 21, 515–528, 1995.

13. ALI J. CHAMKA, *Solutions for fluid-particle flow and heat transfer in a porous channel*, Int. J. Engg. Science, **34**, 1432–1439, 1996.

14. ZHIXIONG GUO, SEO YOUNG KIM and HYUNG JIN SUNG, *Pulsating flow and heat transfer in a pipe partially filled with porous medium*, Int. J. Heat Mass Transfer, **40**, 4209–4218, 1997.

15. T. MOSCHANDREOU and M. ZAMIR, *Heat transfer in a tube with pulsating flow and constant heat flux*, Int. J. Heat Mass Transfer, **40**, 2461–2466, 1997.

16. DAE-YOUNG LEE, SANG JIN PART and SUNG TACK RO, *Heat transfer in thermally developing region of a laminar oscillating pipe flow*, Cryogenics, **38**, 584–594, 1998.

17. A. OGULU and T.M. ABBEY, *Simulation of heat transfer on an oscillatory blood flow in an indented porous artery*, International communication in Heat and Mass Transfer, In press 2005.